

Roll-to-Roll Advanced Materials Manufacturing DOE Laboratory Consortium - FY 2017 Final Report

ORNL/SPR-2018/774

January 2018

Funding provided by:

U.S. Department of Energy

Office of Energy Efficiency and Renewable Energy

Advance Manufacturing Office



ANL Resin Wafer Extruder System



ORNL Dual Slot Die Coater



NREL R2R GDE Studies



LBNL Modeling of Slurry Mixing



Disclaimer

This report was prepared as an account of work sponsored by an agency of the United States government. Neither the United States government nor any agency thereof, nor any of their employees, makes any warranty, express or implied, or assumes any legal liability or responsibility for the accuracy, completeness, or usefulness of any information, apparatus, product, or process disclosed or represents that its use would not infringe privately owned rights. Reference herein to any specific commercial product, process, or service by trade name, trademark, manufacturer, or otherwise does not necessarily constitute or imply its endorsement, recommendation, or favoring by the United States government or any agency thereof. The views and opinions of authors expressed herein do not necessarily state or reflect those of the United States government or any agency thereof.

DOCUMENT AVAILABILITY

Reports produced after January 1, 1996, are generally available free via US Department of Energy (DOE) SciTech Connect.

Website <http://www.osti.gov/scitech/>

Reports Produced before January 1, 1996, may be purchased by members of the public from the following source:

National Technical Information Service
5285 Port Royal Road
Springfield, VA 22161
Telephone 703-605-6000 (1-800-553-6847)
TDD 703-487-4639
Fax 703-605-6900
E-mail info@ntis.gov
Website <http://www.ntis.gov/help/ordermethods.aspx>

Reports are available to DOE employees, DOE contractors, Energy Technology Data Exchange representatives, and International Nuclear Information System representatives from the following source:

Office of Science and Technical Information
PO Box 62
Oak Ridge, TN 37831
Telephone 865-576-8401
Fax 865-576-5728
Email reports2osti.gov
Website <http://www.osti.gov/contact.html>

Foreword

Oak Ridge National Laboratory (ORNL), Argonne National Laboratory (ANL), Lawrence Berkeley National Laboratory (LBNL), and the National Renewable Energy Laboratory (NREL) in collaboration with Eastman Kodak Business Park (Kodak) and Citrine Informatics (Citrine) formed Roll-to-Roll Advanced Materials Manufacturing (R2R AMM) Department of Energy (DOE) Laboratory Consortium in April 2016 to broadly disseminate materials, process science, and advanced technologies to industry in R2R manufacturing. This multi-laboratory and industry partnership enables advanced R2R manufacturing research and development to demonstrate a materials genomic approach to optimization of process parameters for finding new transformational improvements in manufacturing technologies enabling clean energy applications. The Laboratories successfully demonstrated their combined capabilities for a fast, clean energy manufacturing development in Fiscal Year (FY) 2016 as a seed effort. The first project for demonstration was to develop a novel cathode material for Li-ion battery manufacturing. For FY 2017, efforts have continued for matching anode development and expanded in other areas of fuel cells, water membranes and other functional materials. This consortium creates a critical team of national experts covering all needed aspects from materials synthesis modeling and simulation through materials development, slurry formulation, scale-up, pilot deposition, process development, non-destructive process evaluation, big data analytics and validation, to full scale production of rolled goods. This new approach will enable an order of magnitude shorter process development cycles bringing them from 20 years down to a few years with the pathway for initial commercialization within months of pilot scale demonstrations.

DOE cost targets for advanced energy storage and conversion applications will not be met without significant and timely advancements in R2R manufacturing. Required R2R advances include adaptation of existing processing methods and development of novel methods that have the potential to significantly impact U.S. manufacturing sector recovery, environmental security, energy security, and sustainable transportation adoption. Economies of scale through increased manufacturing volumes based on traditional assembly and processing methods will not suffice. For example, current baseline technology cell costs in the Li-ion battery industry are about $2.5\times$ the \$100/kWh ultimate target of DOE Vehicle Technologies Office (VTO) (Howell 2017). To increase the capacity from 250 Wh/kg to 1000 Wh/kg for anode materials, novel R2R processing technologies will be required. Furthermore, polymer electrolyte fuel cell stacks currently cost almost $10\times$ in low volumes compared to the ultimate cost of the DOE Fuel Cells Technology Office (FCTO) target of \$20/kW by the year 2020 (Garland 2017). Water consumption for renewable energy technologies can be as high as a medium value 4,500 gallons/MWh and more than 44,000 gallons/MWh for non-renewable energy applications (Macknick et al. 2011). New technologies are needed to increase the capacity of these systems to meet future needs. Other examples of the Energy Efficiency and Renewable Energy (EERE) Office funded technologies that have a similar cost-target issue are chemical-process industry membranes, window films, photovoltaic films, and electronic films. The EERE Advanced Manufacturing Office (AMO) is poised to assist in reaching the low dollars per unit costs of these various critical energy related applications through addressing R2R manufacturing problems common to each application.

Preface

The following report provides a description of the program structure and technical accomplishments made during FY 2017 to overcome challenges for expanding use of R2R technologies and processing for clean energy applications. Technologies are under development that enable enhanced manufacturing of battery electrodes, fuel cells and water separation membranes that take advantage of advancements in new functional materials. Data mining, visualization, modeling and simulation for the materials, technologies and processes being developed allow for improvements in R2R manufacturing applications. This report documents the research conducted by four DOE national laboratories as a consortium in collaboration with industry partnerships. The research is directly applicable to AMM strategies that apply the National Science and Technology Council's Materials Genome Initiative (NSTC 2011) approach to enhance the performance of battery, fuel cell and water membrane materials. This effort supports building the foundation of technologies, processes and a U.S. manufacturing base that will enable an order of magnitude in shorter process development cycles with the pathway for initial commercialization within months instead of years.

Acknowledgements

First and foremost, the following scientists, investigators and technical support who are working diligently to realize their innovative ideas and technological developments in R2R processing and their desire to deploy them broadly for energy storage applications are acknowledged for their contributions:

ANL: Youngho Shin, Ozge Feridun, Andrew Jansen, Gerald Jeka, Alison Dunlop, Steve Trask, Bryant Polzin, Dennis Dees, Seth Snyder, Yupo Lin

ORNL: *Structured Lithium-Ion Battery Anode and Cathode Tasks:* Marissa Wood, T. J. Christensen, Jianlin Li, Yangping Sheng, Zhijia Du; *Thickness Feedback Loop and Process Controls Task:* Alex Melin, Kofi Korsah, Yarom Polsky, Marissa Wood, T. J. Christensen; *Fuel Cell Gas Diffusion Electrode Coating Task:* T. J. Christensen, Jianlin Li, Marissa Wood

NREL: Peter Rupnowski, Brian Green, Scott Mauger, KC Neyerlin, Ami Neyerlin, Sunil Khandavalli, Jason Pfeilsticker, Shriram Santhanagopalan, Maikel van Hest, Rob Tenent, Jason Woods

LBNL: Fuduo Ma, Dula Parkinson, Harold Barnard, David Trebotich, Steve Ferreira, Gerd Ceder, Vince Battaglia, Olga Kononova

DOE EERE AMO: David Hardy (Technical Project and Program Management)

We would like to acknowledge Matt Fronk and Daniel Ocorr at Kodak Eastman Business Park, Rochester, NY, for their participation in the R2R AMM DOE Laboratory Consortium program and their insights for improving technologies and processes for R2R manufacturing. Their inputs were of great value to the consortium team for building a technical portfolio and defining R2R problems.

Also, Greg Mullholland, Chief Operating Officer and Sean Paradiso at Citrine Informatics must be recognized for their collaboration and technical support with the analysis of the battery electrode research data and the development of a machine learning model for improving cathode design.

Finally, we would also like to acknowledge the contributions of Fred Crowson, Energetics, for his project management assistance and assistance in preparing and publishing this report.

The research at

- Oak Ridge National Laboratory, managed by UT Battelle, LLC for the U.S. Department of Energy, under contract DE-AC05-00OR22725
- Argonne National Laboratory, managed by University of Chicago Argonne, LLC for the U.S. Department of Energy, under contract DE-AC02-06CH11357
- Lawrence Berkeley National Laboratory, managed by University of California for the U.S. Department of Energy, under contract DE-AC02-05CH11231
- National Renewable Energy Laboratory, managed by Alliance for Sustainable Energy, LLC for the U.S. Department of Energy, under contract DE-AC36-08GO28308

was sponsored by the Office of Energy Efficiency and Renewable Energy, Advanced Manufacturing Office (Mark Johnson and David Hardy).

Acronyms and Abbreviations

(Definitions for terminology used in this report are in the Glossary section at the end of this report)

η_{hydr}	hydrodynamic viscosity
η_L	viscosity of PVDF and NMP solution
η_{struct}	colloidal interaction viscosity
ϕ_a	volume fraction of carbon black aggregates
ϕ_m	maximum packing fraction
ϕ_p	isolated carbon black volume fraction
°C	degrees Centigrade
µm or µ	micrometers or microns
µm/h	micrometers per hour
\$/kW	dollars per kilowatt
\$/m ²	dollars per square meter
1C, 2C etc.	a charge current of 1, 2, etc. time the rated capacity
A	amp
AAAS	American Association for the Advancement of Science
ACS	American Chemical Society
Ah	amp-hour
AIMCAL	Association of International Metallizers, Coaters and Laminators
AMM	Advanced Materials Manufacturing
AMO	Advanced Manufacturing Office
ANL	Argonne National Laboratory
API	application programming interface
BR	batch reactor
C	chemical symbol for carbon
CA	California
CAMP	Argonne National Laboratory's Cell Analysis, Modeling and Prototyping facility
CB	carbon black
CCM	catalyst-coated membrane
cm ²	centimeter squared
Co	chemical symbol for cobalt
CO	Colorado
CRADA	Cooperative Research and Development Agreement
CSTR	continuous stirred tank reactor
CVS	comma separated values
D10, D50, D90	the value of the particle diameter at 10%, 50% and 90% in the cumulative distribution for a group of particles
DC	District of Columbia
DOI	Digital Object Identifier
DOE	U.S. Department of Energy
DP	dual pass; to process a coating on one side of a substrate on a single pass through a process and then coat the substrate on the back side of the substrate in a second pass

EC:DEC	ethylene carbonate (EC)–diethyl carbonate (DEC) electrolyte
EC:EMC	ethylene carbonate (EC)–ethyl methyl carbonate (EMC) electrolyte
ECS	Electrochemical Society
EERE	Energy Efficiency and Renewable Energy
e.g.	abbreviation meaning “for example”; a Latin phrase, “ <i>exempli gratia</i> ” meaning “for the sake of example”
etc.	abbreviation for the Latin phrase “ <i>et cetera</i> ” which means “and so forth”
F1	In statistical analysis of binary classification, the F1 score (also F-score or F-measure) is a measure of a test's accuracy and considers both the precision and the recall of the test to compute the score.
FCTO	Fuel Cell Technologies Office
FY	fiscal year
g	gram or grams
GDE	gas diffusion electrode
GDL	gas diffusion layer
h or hr	hour
h_c	separation where the minimum interparticle potential locates
Hg	chemical symbol mercury
HPC	high-performance computing
HPPC	hybrid pulse-power capability (or characterization)
HSC	high surface-area carbon
HTML	hypertext markup language
I/C	ionomer to carbon ratio
IL	Illinois
IOP	Institute of Physics
IR	infrared
kg	kilogram
Kodak	Eastman Kodak Business Park
kT	product of the Boltzmann constant, k , and the temperature, T
kWh	kilowatt hour(s)
kWh/m ³	kilowatt hours per cubic meter
L or l	liter(s)
LBNL	Lawrence Berkeley National Laboratory
L/h	liters per hour
Li	chemical symbol for lithium
LiPF ₆	lithium hexafluorophosphate
M	molar
mAh	milliamp-hour
mAh/cm ²	milliamp-hour per square centimeter
mAh/g	milliamp-hour per gram
MEA	membrane electrode assembly
MERF	Materials Engineering Research Facility
mg/cm ²	milligram per square centimeter
min(s)	minute(s)
mL/h	milliliters per hour
mm	millimeters
Mn	chemical symbol for manganese
NCM or NMC	nickel-manganese-cobalt
Ni	chemical symbol for nickel

nm	nanometer
NMP	N-Methyl-2-pyrrolidone
NREL	National Renewable Energy Laboratory
NSTC	National Science and Technology Council
NY	New York
OLED	organic light-emitting diode
ORNL	Oak Ridge National Laboratory
PDF of pdf	portable document file
PEMFC	polymer electrolyte membrane fuel cell
pH	the negative logarithm of the effective hydrogen-ion concentration or hydrogen-ion activity in gram equivalents per liter of the solution
Pt	chemical symbol for platinum
PV	photovoltaic
PVDF	polyvinylidene fluoride
QC	quality control
R2R	roll-to-roll
RSC	Royal Society of Chemistry
s	second(s)
SEM	scanning electron microscope (or microscopy)
SP	single pass
STEM	scanning transmission electron microscopy
T&DM	text and data mining
TEM	transmission electron microscopy
TN	Tennessee
TODA	TODA America, Inc.
TOF	time-of-flight (a technique used in microscopy)
TVR	Taylor vortex reactor
USABC	United States Advanced Battery Consortium
USAXS	ultra-small angle x-ray scattering
V	volt
vol.	volume
vs.	versus
VTO	Vehicle Technologies Office
Wh/kg	watt-hour per kilogram
wt%	percent by weight
XCT	x-ray computed tomography
XML	extensible markup language
XRF	x-ray fluorescence (or fluorometer)

Table of Contents

Disclaimer.....	i
Foreword.....	ii
Preface.....	iii
Acknowledgements.....	iv
Acronyms and Abbreviations.....	v
Table of Contents.....	viii
List of Figures.....	x
List of Tables.....	xiii
Executive Summary.....	1
Accomplishments.....	1
Technology Assessment.....	4
Roll-to-Roll Advanced Materials Manufacturing DOE Laboratory Consortium Project.....	6
Consortium Contacts.....	6
Annual Operating Plan Title and Corporate Planning System (CPS) Agreement Numbers.....	7
Project Introduction.....	8
Approach.....	8
Core Program.....	8
FY 2018 Plans.....	10
Technology Transfer Paths.....	12
Results.....	12
Structured Anode Study.....	12
Argonne National Laboratory.....	12
Oak Ridge National Laboratory.....	17
National Renewable Energy Laboratory.....	31
Citrine.....	34
Fuel Cell Study.....	35
National Renewable Energy Laboratory.....	35
Argonne National Laboratory.....	38
Oak Ridge National Laboratory.....	41

Modeling and Simulation.....	42
Lawrence Berkeley National Laboratory.....	42
R2R Functional Materials.....	50
R2R Water Nexus.....	54
Collaboration/Coordination/Outreach/CRADA.....	60
Workforce Development/Educational Outreach.....	61
Challenges/Contingencies.....	62
Risks and Risk Handling/Project.....	63
Project Ratings.....	63
Conclusions.....	65
Glossary.....	66
Key Publications.....	69
References.....	69
Bibliography.....	70

List of Figures

Figure 1. Cycle life plot of baseline electrodes with following active materials: SLC1520P: NMC532 6 μm , SLC1506T: NMC532 6 μm and 50/50 mix SLC1520P/SLC1506T: NMC532 6 μm . These cells were cycled between 3 to 4.2V and are representative cells (capacity based upon grams of cathode material)	13
Figure 2. Cycle life plot of cathode double pass NMC532 12 μm in the bottom layer and NMC532 6 μm in the top layer paired against various anode electrodes. The key to the anodes used is on the graph. These cells were cycled between 3 to 4.2V and are representative cells (capacity based upon grams of cathode material)	14
Figure 3. Cycle life plot of the 100% NMC532 6 μm cathode paired against various anode electrodes. The key to the anodes used is on the graph. These cells were cycled between 3 to 4.2V and are representative cells (capacity based upon grams of cathode material)	14
Figure 4. Cycle life plot of cathode single pass NMC532 6 μm in bottom layer and NMC532 12 μm in the top layer paired against various anode electrodes. The key to the anodes used is on the graph. These cells were cycled between 3 to 4.2V and are representative cells (capacity based upon grams of cathode material)	15
Figure 5. Cycle life plot of cathode double pass NMC532 6 μm in the bottom layer and NMC532 12 μm in the top layer paired against various anode electrodes. The key to the anodes used is on the graph. These cells were cycled between 3 to 4.2V and are representative cells (capacity based upon the full coin cell)	15
Figure 6. Dual slot die setup used to make cathode (FY 2016 effort) and anode (FY 2017 effort) coatings (#5 and #6). Each cylinder contains a slurry that is extruded through either the top or bottom slit in the slot die (shown in the enlarged picture), allowing two layers to be coated simultaneously	17
Figure 7. High-rate pouch cell cycle life comparison (1000 cycles) at charge of 1C and discharge of 2C. HPPC was performed every 50 cycles. Each error bar is an average of the standard deviation for those 50 cycles. Data is an average of 3 cells for each coating	18
Figure 8. Long-term pouch cell cycle life (~1000 cycles) comparison at charge of C/3 and discharge of C/3. HPPC was performed every 50 cycles. Data is an average of three cells for each coating type except for cathode coatings #4 and #6, which were a 2-cell average, and each error bar is an average of the standard deviation for those 50 cycles	18
Figure 9. Comparison of pouch cells made with coating #1 (all small particles) using different electrolytes. (a) Rate performance comparison between pouch cells made with different and (b) comparison of capacity at C/10, C/2, and 2C discharge rates for ANL coin cells	19
Figure 10. Rheological properties of anode (a & b) and cathode (c & d) slurries used for slot-die coatings in terms of shear stress versus shear rate ((a) and (c)) and viscosity versus shear rate ((b) and (d))	23
Figure 11. Discharge rate performance comparison for single-layer pouch cells made with (a) cathode #1 (all small particles) and (b) cathode #3 (dual-pass with large particles on the bottom and small particles on top) and seven different anode coatings; and (c) comparison of all cells made with cathodes #1 and #3	26
Figure 12. Charge rate performance comparison for single-layer pouch cells made with (a) cathode #1 (all small particles) and (b) cathode #3 (dual pass with large particles on the bottom and small particles on top) and seven different anode coatings. (c) Comparison of all cells made with both cathode #1 and cathode #2	28

Figure 13. Cathode and anode pore size distributions measured by mercury porosimetry: (a) uncalendered cathode coatings, (b) calendered cathode coatings, (c) uncalendered anode coatings, and (d) calendered anode coatings	30
Figure 14. Fraction of rated capacity (C/10 discharge rate) for three different structured cathode/anode combinations as compared to cathode #1 - anode #1 (C1/A1) baseline	31
Figure 15. Cathode solid loading as a function of (a) the penetration depth model for Ni and (b) measurement uncertainty calculations	32
Figure 16. XRF analysis of cathode areal loadings	33
Figure 17. (a) Porosity model thermal responses for the 10 coated cathodes and (b) thermal responses in the mid-IR (~3 - 5 μm) range for the 10 coated cathodes showing the sensitivity of the responses in the wavelength band to slight differences in emissivity in some of the samples.....	34
Figure 18. Catalyst ink structure dependency on carbon type and Pt: (a) effect of the addition of Nafion ionomer and (b) impact of Pt catalyst on ink structure	36
Figure 19. Kelvin Probe data for electrode inks of different ionomer-to-carbon ratios and different solvent ratios at different drying temperatures.....	37
Figure 20. Experimental apparatus at the Advanced Photon Source for determining catalyst agglomerate size and content of catalyst-ionomer-solvent inks during sonication	39
Figure 21. Ultra-small angle x-ray scattering profiles for ink sample 1a (Table 1) before sonication, after horn sonication, and during bath sonication	40
Figure 22. X-ray scattering intensity (proportional to the number of scatterer), at two sizes: (a) 3 μm and (b) 300 nm as a function of sonication time	40
Figure 23. Measurement of thickness variability of SGL Group SIGRACET GDL 29BC carbon baseline GDL substrate for making GDE coatings	41
Figure 24. Visualization apparatus: (a) improvised equipment for in-situ visualization of the slurry doctor blading process, (b) enlarged view of the doctor blade head, and (c) Snapshots of the doctor blading dynamic process for slurries of 13% and 26% particle volume fractions	43
Figure 25. Rheology modeling of carbon black slurry: (a) interparticle potential between two carbon black particles dispersed in PVDF and NMP solution, (b) microrheological modeling of carbon black slurries with different volume fractions, and (c) schematics of the polymer brushes' morphologies on surface carbon blacks at a variety of ratios between polymer binder and carbon blacks	44
Figure 26. Rheological properties of the anode slurries: (a) viscosities of the slurries at varying shear rates, (b) linear viscoelastic regime test of the slurries, and (c) storage modulus of the slurries	47
Figure 27. Schematic representation of the project pipeline to create database of “codified” synthesis recipes. Source: LBNL.....	48
Figure 28. Schematic representation of recurrent neural network algorithm for synthesis paragraph classification.....	49

Figure 29. SEM images of (a) $\text{Ni}_{1/3}\text{Mn}_{1/3}\text{Co}_{1/3}(\text{OH})_2$ synthesized in pH 10.6 solution (i.e. sample A), and (b) $\text{Ni}_{1/3}\text{Mn}_{1/3}\text{Co}_{1/3}(\text{OH})_2$ synthesized at pH 11.4 (i.e. sample B). Source: ANL	51
Figure 30. Particle size growth and the effective radius of disk: (a) dynamics of $\text{Ni}_{1/3}\text{Mn}_{1/3}\text{Co}_{1/3}(\text{OH})_2$ secondary particle growth measured by particle size analyzer and (b) dynamics of primary particle growth of sample measured by in-situ USAXS	52
Figure 31. Individual and total metal-ammonia complex: (a) concentration of metal-ammonia complex with respect to pH showing neither very low pH nor very high pH is beneficial for the formation of the metal-ammonia complex, (b) increase in primary particle diameter with time showing that initially it increases quickly and eventually saturates due to aggregation and loss of contact with the reacting solution, and (c) growth of secondary particle diameter with time at pH = 11.0 and $c_{\text{NH}_3} = 1.0\text{M}$ showing a good correlation with the square-root of time curve indicating that the aggregation process is diffusion limited	53
Figure 32. Variation in secondary particle size obtained at the end of coprecipitation process conducted at different magnitudes of pH: (a) comparison between experimentally obtained and computationally predicted diameter of the secondary particles obtained at different pH values and (b) phase map between ammonia content and solution pH. Source: ANL	54
Figure 33. Schematic of semi-automated assembly line to produce resin wafers	55
Figure 34. Blending equipment and materials: (a) OptimaBlend™ Sanitary Lab Blender, and (b) particles mixtures from the laboratory and the industrial blender. Source: Eirich Machines and LBNL	56
Figure 35. All-Fill Inc. Model BS particle dispenser with lift and inflatable bag clamp. Source: All-Fill Inc....	57
Figure 36. Curing equipment: (a) INTEK Corporation electric infrared conveyor oven and (b) the temperature profile measurement of the oven at 395°F (187°C). Source: Intek Corporation.....	58
Figure 37. Resin wafer fabrication: (a) sample before and after curing in the INTEK electric infrared conveyor oven and (b) results of ionic conductivity measurements. Source: ANL	59
Figure 38. The assembly line under construction to incorporate the blender, the dispenser and oven. Source: ANL	59

List of Tables

Table I. Summary of Electrode Couple Performance from the Cycle Life Data	16
Table II. Current specifications for existing slot-die coating head	20
Table III. Target specifications for new slot-die coating thickness feedback control loop	20
Table IV. Compositions of Catalyst-Ionomer-Solvent Inks for Agglomeration Studies	39
Table V. Total Number of Papers from Various Publishers Successfully Retrieved and Presented in the Current Version of the Database.....	48
Table VI. R2R AMM Laboratory Consortium Project Ratings	64
Table VII. Technology Readiness Level Definitions	68

Executive Summary

High-value R2R processing is used to support a wide range of products in applications which span many industrial business sectors. The overall R2R process technology can be considered as “mature” as the process methodology, in one or another variation, has been in use for decades. The technique traditionally involves deposition of material(s) onto moving webs or carriers or other continuous R2R, belt-fed, or conveyor-based processes that enable successive steps to build a final construction which serve to support these deposited materials.

Current process technologies, which typify “roll to roll”, include tape casting, silk-screen printing, reel-to-reel vacuum deposition/coating and R2R lithography. Products supported by R2R manufacturing include micro-electronics, electro-chromic window films, photovoltaics (PVs), fuel cells for energy storage and generation battery electrodes, and barrier materials. An example in industry, where introduction of R2R proved invaluable to enable cost-effective high-volume manufacturing, is in the fabrication of multi-layer capacitors. Initially, in the 1960’s a single capacitor with relatively few layers was valued in multiple dollars. However, due to innovation in materials and process equipment, high-quality yet very low-cost multi-layer capacitors are manufactured today on a very cost-competitive basis.,

It has long been recognized that, to move energy-related products from high-cost niche applications to use by the public, a means needs to be available to enable manufacture of these products in a cost-competitive manner, yet yielding products which are affordable by the general consumer. Fortunately, products such as fuel cells, thin- and mid-film PVs, batteries, electrochromic and piezoelectric films and other energy saving technologies readily lend themselves to manufacture using R2R approaches.

Within the DOE EERE AMO, it was recognized that establishment of a program supported at the DOE National Laboratories, along with the immense design of materials and equipment modelling capability enabled with use of high-performance computing at these same labs, could take advantage of available R2R infrastructure to manufacture these technologies. Therefore, a R2R Consortium was established and provided with initial “seed” funding to take an approach consistent with the National Science and Technology Council’s Materials Genome Initiative to materials and applications that were envisioned to be supportable by advanced manufacturing R2R processes (NSTC 2011). This collaborative approach was designed to foster identification and development of materials and processes related to R2R for clean-energy product development. Using computational and experimental capabilities by acknowledged subject matter experts within the supported National Laboratory system, the R2R Consortium would leverage the capabilities and expertise at each of four laboratories to further the development of this enabling high-volume cost-competitive platform technology.

As such, a R2R AMM DOE Laboratory Consortium comprised of ORNL, ANL, NREL and LBNL, coordinating with Kodak’s Eastman Business Park (Kodak) and other selected industry partners, was formed in April 2016 to address enhancing battery electrode performance and R2R manufacturing challenges. The objective of the FY 2016 project was to develop a materials genome synthesis process amenable to R2R manufacturing and to provide modeling, simulation, processing, and manufacturing techniques that demonstrate the feasibility of process controls and scale-up potential for improved battery electrodes. The research efforts were to predict and measure changes and results in electrode morphology and performance based on process condition changes; to evaluate mixed, active, particle size deposition and drying for novel electrode materials; to model various process condition changes and the resulting morphology and electrode performance; and to develop and validate non-destructive evaluation techniques for in-line measurement of battery electrode material properties.

The four National Laboratories used a collaborative approach to look at compositions of materials with different particle sizes to make electrode samples using a R2R manufacturing process. The shape, size, and morphology of the materials, the chemistry of the formulation, the nature of slurries, their coating rate, the rate

of drying all play a role in determining the final coating architecture, quality, and performance. A commercial cathode material was selected to make a series of cathodes and anodes by single pass, dual pass and slot die methods. Results from formation and rate studies of half-cell testing showed that porosity had little effect on the cell performance. Based on these results, 40% porosity cathodes were selected for further testing with matched anodes in FY 2017.

An additional core project was added in FY 2017 to conduct studies of fuel cell materials that can be produced using R2R processes. The goal of this project is to explore, understand and optimize material and process parameters to support increased throughput, increased quality, and reduced cost for high volume production of gas-diffusion electrodes (GDEs) for polymer electrolyte membrane fuel cells (PEMFCs). Project work in FY 2017 included detailed ink formulation, mixing, and rheology studies; small-scale and R2R coating of GDEs; characterization of gradient GDE structures using standard and newly developed techniques; and membrane electrode assembly (MEA) fabrication and in situ testing of the performance impacts of different material and process parameters. Two other projects for AMM Functional Materials and R2R Water Nexus were funded by AMO and added to the consortium portfolio. The AMM Functional Materials effort aims to enable advanced materials process R&D, scaleup and synthesis of next generation functional materials; develop several materials, processes, software tools and techniques that support and are potentially compatible with continuous manufacturing process technologies over a range of functional energy-related materials; prototype, characterize and develop a material properties database suitable to support related materials design; and provide uniform, baseline materials to industry for validation and to researchers for further development. The objectives for the R2R Water Nexus project are to remove the material manufacturing hurdle for water membrane materials, evaluate the manufacturing tools to improve material properties for energy and cost savings, and demonstrate the application of advanced manufacturing technology to improve water treatment efficiency and processing cost.

The R2R AMM DOE Laboratory Consortium successfully completed all tasks to develop an enhanced battery material using a R2R manufacturing process and to provide modeling, simulation, processing, and manufacturing techniques that demonstrate the feasibility and potential for scale-up. Technology transfer for this and other technology areas applicable to R2R manufacturing was initiated through a Cooperative Research and Development Agreement (CRADA) solicitation to industry. This DOE-Industry partnership will result in low manufacturing costs, low energy processes, high volume production, high throughput due to improved materials, compatibility with many material platforms, and products with varying sizes and dimensions. The primary metrics of success are throughput, energy use and yield.

Accomplishments

The consortium as a team participated in bi-monthly review meetings with DOE AMO/FCTO Program Managers to ensure information is made available on a continuous and regular basis. Team members also presented at the TechConnect World Innovation Conference, the 2017 DOE Hydrogen and Fuel Cells Program and Vehicle Technologies Office Annual Merit Review and Peer Evaluation Meeting, and the AMO Peer Review. As a team, the consortium executed a CRADA solicitation and received six proposals that are in various stages of approval and contract award. The solicitation stays open and proposals are being considered for evaluation and presented to DOE for final selection.

Structured Anode Study

The ANL core project for the Structured Anode Study produced low loading baseline anode and cathode electrodes, along with non-structured high loading anode electrodes. The low loading baseline electrodes were made into coin cells and tested in FY 2017 for comparisons to the high loading structured electrodes. In addition to the baseline cells, a full matrix of plain, mixed and structured anodes and cathodes were made into coin cells and tested. At the conclusion of FY 2017, approximately two-thirds of the testing matrix was completed along with the data analysis. All scheduled milestones for FY 2017 were met.

ORNL completed seven anode coatings and re-coated seven cathodes. Testing was finished on the high-rate (1C/-2C) cycling up to 1000 cycles with 1.5 Ah pouch cells and ~1000 United States Advanced Battery Consortium (USABC) cycles (at C/3 charge and C/3 discharge) with 0.5 Ah pouch cells for six cathode coatings. Tests were also completed for discharging and charging rate performance of two cell groups with new anodes and FY 2016 cathode structures at 4 mAh/cm² loadings and all small particles for one cathode and with large particles on the bottom and small particles on the top for a second cathode. Mercury (Hg) porosimetry measurements of new anodes (calendered and uncalendered) and re-coated FY 2016 cathodes (calendered and uncalendered) were made for additional data on the electrode materials

NREL completed x-ray fluorescence (XRF) analysis of cathode areal loading and developed an x-ray penetration depth model used to understand the change in sensitivity with loading to estimate measurement uncertainty as a function of loading. An intrinsic uncertainty at about 0.7% (averaged over 33 trials) was determined and manganese (Mn) was found to have the best penetration/least loading uncertainty. NREL completed testing and analysis of ORNL cathodes with a porosity diagnostic. Fabrication of 10 different cathodes took place on the ORNL slot die coating line. Samples with nine loadings at three slurry solids and three coating speeds were used to verify the porosity model with all 10 cathodes. FY 2017 efforts by NREL resulted in a joint NREL-ORNL publication on the cathode porosity diagnostic in Journal of Power Sources, and a submitted joint patent application.

Fuel Cell Study

The NREL core project for the Fuel Cell Study began by solidifying the roles and interactions with ANL, ORNL and LBNL with respect to ultra-small angle x-ray spectroscopy (USAXS), x-ray computed tomography (XCT) characterization, dual-slot coating, calendaring, electron microscopy, and phase field modeling. Small-scale (bar and rod) coating of electrode samples were completed to explore the impact of ink composition and drying parameters on the creation of an ionomer-rich electrode surface layer. A novel surface analysis technique based on Kelvin Probe was developed and validated to quickly screen coated samples for surface ionomer content. NREL completed MEA fabrication and in situ performance testing of ionomer-rich-surface layer small-scale coated samples, which showed that the best samples to date perform well compared to baselines, and that the Kelvin Probe method correlates to measured performance. Initial R2R gravure coating of single-layer fuel cell electrodes were completed to achieve ionomer-rich surfaces, based on a range of conditions identified in the small-scale testing.

ANL developed a method and experimental apparatus for determining micro-structure of inks during sonication. Ink characterization shows that most of the break-up of large agglomerates (>~1 μm) occurs in the first five minutes of horn sonication. Agglomerates were not re-formed when sonication was stopped. Water-rich solvent is more effective at breaking up agglomerates than a n-propanol-rich solvent. Catalysts with platinum (Pt) on high surface-area carbon (HSC) support showed better break-up of agglomerates than catalysts with Pt on medium surface area carbon, and addition of the ionomer facilitates the break-up of agglomerates.

ORNL completed thickness homogeneity measurements of NREL supplied gas diffusion layer (GDL) roll, from SGL Group – The Carbon Company, to obtain understanding of GDL thickness variations on electrode coating step. Initial small-scale coating trials of carbon-black inks were performed with a tape caster. Microscopy support was obtained from the ORNL Materials Characterization Center to verify NREL-coated bilayer (electrocatalyst/ionomer) microstructures. A workplan with ANL's Sensors and Embedded Systems Group was modified to allow outfitting the pilot slot-die coating line with a coating thickness feedback loop to adjust the rate of the dispersion pump.

Functional Materials

ANL conducted investigations on the synthesis of transition metal hydroxide precursors for the many materials, including lithium ion battery cathode materials, which focused on the secondary particle size

distribution of the hydroxides collected after a 3-hour reaction time. Further analyses were conducted on the dynamics of the primary particle growth for two different concentrations of the total transition metal ions and metal hydroxide in a reactor. A simplified multiscale computational model was developed that can capture the nucleation growth and aggregation of primary particles that leads to the formation of secondary particles.

R2R Water Project

The ANL R2R Water Nexus project initiated efforts to develop a R2R process to fabricate resin wafers and benchmark their performance in comparison to existing fabrication methods. Plans were developed to evaluate materials for a new reverse flow resin wafer electrodeionization system that will provide a higher capacity and be more energy efficient than current materials for water treatment. The design for a semi-automated assembly line of porous resin wafers was developed that will increase the fabrication rate by 10x. The design incorporated industrial equipment including a mixer, a dispenser and an infrared oven in the assembly line, which will significantly reduce the curing time (by 60x) of wafer fabrication.

Modeling, Simulation and Data Mining

The LBNL core project continued to focus on the modeling and simulation of electrode materials and initiated an effort to data mine material properties from the open literature for predictive synthesis of new materials. Research continued to determine the role of colloidal interactions in slurries of materials for Li-ion battery fabrication. Studies were completed for on situ visualization of the coating process of an anode slurry using optical microscopy. The rheology of carbon black in polyvinylidene fluoride (PVDF) and N-Methyl-2-pyrrolidone (NMP) was investigated to narrow down the theory to single system for developing a model.

LBNL data mining efforts produced a database contain ~1,100,000 papers, including portable document (PDF) and hypertext markup language (HTML) files, which was ~1.5-fold increase compared to the previous database version. Of the HTML files, 43.2% have identified synthesis sections. A total of ~2,800,000 digital object identifier (DOI) citations were identified for downloading. Downloading issues were solved and a new scraping tool, which accounts for specific publisher's web-format, was developed. The accuracy of classification for ~1,700 paragraphs was 96%. LBNL developed an internal Mechanical Turk website for manual annotation of the dataset used to train a learning model.

CRADA

In support of the CRADA solicitation, ORNL completed the solicitation draft and Terms and Conditions and circulated them to the consortium Team Leads, AMO and FCTO Program Managers, and AMO and FCTO Program Directors. ORNL participated in the selection of three CRADA proposals and negotiations of the statements of work. ORNL also participated in the evaluation of three other CRADA proposals.

Technology Assessment

Structured Anode Study

Research conducted at ANL provided baseline and customized materials for new electrodes through material synthesis and fabrication process development. Chemical and physical analysis and performance evaluations of these materials assisted in improving rolled electrode modifications. Electrochemical analysis of coated electrodes was instrumental for anode matching to previously developed cathodes.

The studies at ORNL produced Li-ion anode materials with structured cathodes to improve high-rate capacity (power density) for 4 mAh/cm² electrodes with bilayer structures. Coating process controls and metrology will implement real-time measurement of electrode coating thickness and characterize thickness variation as a function of line speed. Measurements on the webline will validate the model of the coating process for specific

project material applications. The updated model will include automated adjustment features and incorporate model in closed-loop feedback control of process.

NREL continues to develop an in-line porosity diagnostic. The gap in technology being addressed is that, while the porosity of coated battery electrodes is critical to proper performance, there is no current method to monitor the in-line porosity of the heterogeneous electrode thin film during fabrication. This capability is needed to ensure high quality electrodes are being made during high-throughput R2R manufacturing. The goal of the NREL project is to develop and validate a real-time technique based on active thermography that is sensitive to as-coated variations in porosity in battery cathodes and/or anodes and is amenable to a R2R manufacturing environment. Ultimately, the metric is to show that the technique is viable, i.e. sensitive to relevant levels of porosity variation and amenable to line speeds that are relevant for battery R2R processes.

Fuel Cell Study

GDE-style MEAs are becoming increasingly of interest to the fuel cell industry because of ease of coating onto gas-diffusion media rather than directly coating onto the ion-conducting membrane and because current decal-transfer coating of electrodes requires an extra process step, i.e. coating then transfer lamination. The gap in technology being addressed at NREL is that GDE-style electrodes currently require an additional ionomer layer to achieve target performance. The goal of this project led by NREL is to develop single-pass method – either by dual slot simultaneous coating or a phase-segregated single layer coating – to create an ionomer-rich surface layer on a coated GDE that has comparable performance to standard laboratory GDEs with a separate ionomer overcoat layer. The metric is to assist the DOE to achieve cost targets for automotive fuel cell systems at manufacturing volumes of 500,000 systems/year of \$40/kW_{net} in 2020, and ultimately \$30/kW_{net}.

The R2R manufacturing of PEMFC GDEs and a membrane electrode assembly (MEA) processing-performance parameter study will improve high-current-density performance ($>1.5 \text{ A/cm}^2$) of PEMFC MEAs and make unitized MEAs (two GDEs bonded to a polymer electrolyte membrane).

Modeling, Simulation and Data Mining

LBNL continues efforts to apply colloid and interface science to generate fundamental material and process understanding needed to solve battery electrode manufacturing issues and implementing innovative solutions. These studies set the framework for future materials design and fabrication. Materials discovery will be enabled using data-mining approaches of existing and future inputted Meta-Data developed at LBNL, thus accelerating discovery and initial synthesis using high performance computing (HPC).

Functional Materials

ANL has observed one of the first examples of “watching” particle growth during synthesis for both primary and secondary particles. A model was developed that captures nucleation, growth and aggregation, and shows qualitative trends seen in experiments.

R2R Water Project

ANL designed a lab-bench scale resin wafer using a prototype R2R method and conducted studies of resin wafer characterizations, porosity and pore distribution, flow distribution in the wafer, and ionic conductivity. Components were ordered, and the system will be assembled and commissioned in FY 2018.

Roll-to-Roll Advanced Materials Manufacturing DOE Laboratory Consortium Project

Consortium Contacts

Claus Daniel, Project and Consortium Team Lead

Oak Ridge National Laboratory (ORNL)
National Transportation Research Center
2360 Cherahala Blvd.
Knoxville, TN 37932
Phone: 865-946-1544
Email: danielc@ornl.gov

David L. Wood III, ORNL Project Team Lead

Oak Ridge National Laboratory (ORNL)
National Transportation Research Center
2360 Cherahala Blvd.
Knoxville, TN 37932
Phone: 865-574-1157
Email: wooddl@ornl.gov

Gregory K. Krumdick, ANL Project Team Lead

Argonne National Laboratory (ANL)
9700 S. Cass Avenue
Building 362
Argonne, IL 60439-4844
Phone: 630-252-3952
Email: gkrumdick@anl.gov

Michael Ulsh, NREL Project Team Lead

National Renewable Energy Laboratory (NREL)
15013 Denver West Parkway
Golden, CO 80401
Phone: 303-275-3842
Email: Michael.Ulsh@nrel.gov

Ravi Prasher, LBNL Project Team Lead

Lawrence Berkeley National Laboratory (LBNL)
1 Cyclotron Road
MS 70R 0108B
Berkeley, CA-94720
Phone: 510-495-2679
Email: vsrinivasan@lbl.gov

David C. Hardy, DOE Roll-to-Roll Program Manager

Department of Energy (DOE)
Energy Efficiency and Renewable Energy (EERE)
Advanced Manufacturing Office (AMO)
1000 Independence Ave., S.W., Suite 5F-063
Washington, DC 20585-0121

Phone: 202-586-8092

E-mail: david.hardy@ee.doe.gov

Technical Contacts:

ORNL: Jianlin Li, Marissa Wood

ANL: Andrew Jansen, Bryant Polzin, Yupo Lin, Venkat Srinivasan

NREL: Scott Mauger, Peter Rupnowski

LBNL: Vince Battaglia, Fuduo Ma, Gerd Ceder, Olga Kononova

Partners: Kodak Eastman Business Park, Citrine Informatics

Annual Operating Plan Title and Corporate Planning System (CPS) Agreement Numbers

Roll-to-Roll Manufacturing Science and Applications: From Ideal Materials to Real-World Devices/

ORNL CPS# 97995

ANL CPS #s 29915, 32553 and 32681

NREL CPS #97995

LBNL CPS #31112

Project Introduction

Modern variants of proven, classical R2R coating technologies, as well as new coating methods, are needed for enabling widespread commercialization of renewable energy storage and conversion technologies. Established coating methods, such as multi-layer slot-die, gravure, reverse comma, tape casting, etc. with homogeneity and uniformity superior to spraying methods need to be further adapted for improving performance of various technologies. Examples of sustainable energy technologies and applications are electrochemical energy storage and conversion such as batteries, electrolytic hydrogen production for fuel cells and water separation, smart flexible sensors for building energy efficiency improvement, flexible displays such as organic light emitting diodes and electronics, and photovoltaic panels. The shape, size, and morphology of the materials, the chemistry of the formulation, the nature of slurries, their coating rate, the rate of drying etc. all play a role in determining the final coating architecture, quality, and performance. In addition, non-destructive evaluation (NDE) of the produced coatings for improving in-line quality control (QC) and identification of defects, prior to down-stream value added steps being performed, is of paramount importance.

The challenges to develop new technologies in these areas brought together expertise from four national laboratories to solve the complex nature of the R2R process and methods to improving existing production capabilities. The project has expanded in the second year to focus on fuel cell materials, water separation and purification, and new functional materials. An effort to get industry more involved was initiated through a CRADA solicitation that has produced interest from the commercial sector.

Approach

Core Program

Structured Anode Study

In FY 2017, ANL focused on blending structured cathodes (from FY2016 efforts) with new structured anodes to enable cycling of high loading ($\sim 4.4 \text{ mAh/cm}^2$) electrodes. The materials that were used to produce these electrodes (mostly made by Battery Manufacturing R&D Facility at ORNL) were a lithium metal oxide powder from TODA America, Inc. (TODA) (NMC532) with particle sizes of 6 and 12 microns and a graphite powder from Superior Graphite (SLC1506T and SLC1520P) with a particle size of 6 and 20 microns. These powders were used as individual powders, blended mixes and layered structures in the electrodes. The hope is that the electrode structuring would yield a higher level of electrochemical performance in high loading electrodes.

ORNL is responsible for the materials processing and coating of samples, which includes preparing baseline slurries and anode coatings (small, large and mixed particles), preparing slurries and graded anodes coating and reprocess matching cathodes, building of devices (with emphasis on pouch cells), and providing electrodes to NREL, LBNL, and ANL for further analyses. The approach for characterization and performance of materials uses scanning electron microscopy (SEM) and Hg porosimetry to identify material structures and properties. Battery materials tested for rate capability and capacity fade. In FY 2017, graded cathodes in combination with new anodes were evaluated. Working with the other laboratories that comprise the consortium, ORNL will determine cathode balance loadings, supply microscopy and materials characterization data to LBNL, and supply electrodes to NREL for in-line porosity modeling.

Fuel Cell Study

NREL, as lead lab for the Fuel Cell Study, will address an emerging MEA construction method – namely GDEs – by identifying processes that can reduce the number of process steps (specifically that of coating an ionomer overlayer on the surface of the electrode) in the overall electrode R2R fabrication process. The approach is to understand the fundamental (nano- and micro-scale) interactions in the heterogeneous electrode ink that lead to macro-scale properties determined by rheology, which ultimately impact coating and drying parameters as well as device performance. Advanced characterization tools at ANL and ORNL (USAXS and XCT at the APS, and electron microscopy at ORNL) are being leveraged to understand the dispersion of particles and polymer in the ink and to image the morphology through the thickness of the electrode layer as a function of material, ink, and process parameters. Eventually, modeling capabilities at LBNL will be leveraged to help optimize ink formulation and process parameters via phase field modeling of the material segregation during drying as well as mechanistic modeling of ink rheology. NREL will utilize standard in situ testing to quantify impact of ink and process parameters on performance and, ultimately, leverage FCTO investments in QC development for fuel cell electrodes and identify techniques relevant to the GDE construction.

Modeling, Simulation and Data Mining

LBNL has developed a physics model based on colloidal interactions and this model will be improved for predicting the rheological properties of the anode slurry. Major interactions between particles, such as Van der Waals, electrostatic, and polymer steric interactions were included for calculating the viscosities. The properties of the anode slurry, including particle size and zeta potential, particle and polymer mass ratio, and particle volume fractions will be further investigated. The current model well predicts the viscosities of anode slurries and will be modified for other materials.

The preliminary version of the database of synthesis “recipes” was created from the 848,706 research papers. Each paper was parsed using Natural Language Processing and Machine Learning approaches to extract paragraphs about synthesis routes. The classifier based on Neural Net was subsequently applied to every paragraph to obtain materials, operations and conditions. These efforts will continue by pursuing additional entries to make the database more comprehensive.

Functional Materials

ANL developed a unique capability in visualizing the processing of battery electrodes using in situ x-ray tomography and combined that with first principle calculations as part of the R2R lab consortium. The project has provided insights into the role of viscosity of the slurry and the effect of using different types of binding agents on the final electrode microstructure. The project has also led to the first attempts at correlating the fabrication process to the device performance. Efforts will shift to a greater focus in the materials area due to the universality of the role of materials across technologies, removing focus on a specific technology. This role fills a gap between the synthesis effort and fabrication efforts being pursued by the R2R consortium.

The Materials Engineering Research Facility (MERF) at ANL will examine the growth-dynamics of cathode particle precursors during the coprecipitation process. Computational models will be developed to predict the nucleation, growth and aggregation of the primary particles, which leads to the formation of secondary particles extensively used as the cathode material within lithium ion batteries. Dependence of different processing conditions, such as, pH of the solution and ammonia concentration, on the dynamics of particle growth will be investigated. A link will be established between processing conditions and the morphology of the transition metal hydroxide secondary particle precursors.

Water Nexus

ANL will continue to investigate materials for water separation and purification using the lab bench-scale resin wafer R2R prototype system. For each material fabricated with a R2R method, the resin wafers will be characterized for porosity and pore distribution, flow and ionic conductivity. Water desalination performance and energy extraction from concentrated salt brine will be evaluated for each wafer configuration fabricated.

FY 2018 Plans

Structured Anode Study

The main goal of the FY 2018 work for ANL will be to complete the full test matrix of electrode combinations. There are 12 out of 49 structured-electrode combinations that still need to be tested. ANL will be fabricating cell sets for the remaining combinations and testing them. Rate study, initial hybrid pulse-power capability (HPPC), and cycle life averaging data will be analyzed, and the results reported for the completed cells. Trends outside of capacity fade will be evaluated to see if any structures show promise for further optimization.

ORNL has made steady progress on the FY 2017 structured anode study despite issues with equipment, but a great deal of performance testing will be required moving into FY 2018. Advanced materials characterization of Li-ion electrodes will include surface energy, capillary flow porometry (CFP), transmission electron microscopy/scanning transmission electron microscopy (TEM/STEM). Progress will continue a cross-cutting task that will ultimately help the thickness homogeneity of all coating types.

NREL will study the applicability of the in-line porosity diagnostic to structured anodes and ensure that the porosity model appropriately represents the anodes.

Fuel Cell Study

NREL will continue to lead the cross-lab team and further explore (a) characterization of ink mixing and formulation, (b) gravure and slot die coating conditions, (c) drying parameters, (d) impact of different solvents, (e) electrode-membrane calendaring, (f) coated electrode morphology, (g) phase field and rheology modeling of inks, (h) MEA fabrication and testing, and (i) in-line diagnostics. The goal will be R2R fabrication, by one or more methods, of a single/simultaneous layer electrode with comparable performance to standard lab-fabricated GDEs with an ionomer overcoat layer. Multiple joint publications are expected with the other laboratory partners.

ANL will continue to provide support for the fuel cell study by doing a comparison of ink micro-structure for three mixing procedures (horn and bath sonication, ball-milling) and correlating ink micro-structure results with NREL fuel cell performance results. Analysis of the most recent set of USAXS data will be completed and new nano-tomography data on the NREL cathode catalyst layer samples will be acquired early FY 2018. The purpose of those experiments is to determine the effects of electrode composition and fabrication on electrode structure and to correlate these data with NREL's performance data. In addition, Argonne and NREL are collaborating in correlating the USAXS data with performance data and the results of this correlation are being incorporated into a manuscript which will be submitted to an appropriate journal early in 2018. Aqueous electrochemical measurements of catalyst surface area and oxygen reduction reaction activity as a function of sonication time will be made to determine extent of catalyst damage. Nano-tomography of NREL gas diffusion electrodes and modeling of electrode transport properties using the characterization results will be performed.

Low-cost methods of MEA manufacturing (slot-die, gravure, etc.), i.e. coating electrocatalyst layers onto gas diffusion media to make GDEs will be further evaluated. R2R hot-pressing (calendering) of GDEs to polymer electrolyte membranes will be assessed for making “unitized” MEAs. ORNL will continue advanced materials characterization of the properties for GDEs.

Modeling, Simulation and Data Mining

LBNL plans include building a comprehensive model to understand the rheological properties of electrode slurry in the mixing process. The slurry rheology model will be modified to incorporate the drying process. The relationship between the rheological/viscoelastic properties of slurry and the electrochemical and mechanical performance of battery will be modelled. A determination will be made if the new model is applicable to predict the performance of lithium ion batteries when changing the process conditions. Predictive materials synthesis capability will be developed so that new compounds, targeted morphologies and defect levels, can all be created with a predictive synthesis approach.

Functional Materials

The main aim of this research is to understand the formation of NMC cathode active particles used in lithium ion batteries. After the formation of hydroxide precursors, the next major step is the calcination process where lithium gets inserted into the hydroxides and the transition metals get oxidized. In the next year, we plan to develop a computational model that can successfully capture the physicochemical phenomena that occurs during calcination and elucidate how the operating conditions impact the secondary particle morphology.

R2R Water Project

ANL will convert the bench-scale batch capability to a pilot-scale for semi continuous R2R processing of resin wafers. The resin wafers will be evaluated, and properties and performance characterized.

CRADAS

ORNL will continue efforts to generate more fuel cell industry interest in our CRADA solicitation (beyond Proton OnSite, Lambda Technologies, American Fuel Cell, etc.).

NREL will initiate work on new Solar Windows Technologies and Navitas CRADAs, facilitate the evaluation of current proposals from Lambda Technologies and Proton OnSite, and continue to facilitate submission and review of new CRADA proposals.

Potential New Projects

ANL is investigating a method to establish a flame spray pyrolysis deposition capability onto a R2R substrate.

ORNL is considering a new flexible sensors task for smart buildings applications where relative humidity, carbon dioxide, temperature, motion sensors, etc. are integrated with a thin film battery.

NREL will explore the development and use of real-time imaging tools with broad applicability across the consortium and will develop new core laboratory project proposals supporting R2R technology needs related to building and solar energy technologies.

Technology Transfer Paths

For the core program tasks, technology will be transferred through collaboration with industry and companies receiving CRADA contracts. The CRADA solicitation remains open and, as new companies submit proposals, the consortium team will work closely with any companies receiving awards to ensure technologies are accepted for commercialization. Various aspects of the consortium effort will be presented at conferences, symposia, peer reviews and direct contact with industry and the commercial sector. Specific research will be reported in technical journals and through patent applications.

The modeling and simulation efforts will extend the material genome and integrated computational materials engineering approaches to encompass not only materials discovery, but also to accelerate materials synthesis and fabrication using HPC-related tools. This effort leverages the R2R equipment and technology at ORNL, the engineering expertise and facilities of the MERF at ANL, and the metrology advances and capabilities at NREL in conjunction with the materials design computational efforts of ANL and LBNL. An objective is to demonstrate the ability and to further the current state-of-the-art to accelerate the manufacture of advanced materials using a materials genome computational approach focusing on energy storage and generation (battery and fuel cell) as well as water process materials, associated membranes, equipment, technologies and applications, all as the base applications to impact burgeoning clean energy technologies.

Results

Structured Anode Study

Argonne National Laboratory

The Argonne tasks in the Structured Anode Study were to identify small and large graphite materials, deliver 10 kg samples of these materials to ORNL and smaller samples to LBNL, characterization of graphite materials, fabrication of baseline electrodes, fabrication of plain and blended electrodes, and conduct a viscosity study on graphite slurry blends and provide the data to LBNL. All tasks were completed on schedule to meet the necessary Annual Operating Plan milestones.

For all experimental investigations, the anode and cathode electrode compositions were locked; with only the active material type or electrode structure varied. The cathode consisted of 90 wt% active material (NMC532), 5 wt% Timcal C45 carbon black and 5 wt% Solvay 5130 PVDF binder. The anode consisted of 91.83 wt% active material (graphite), 2 wt% Timcal C45 carbon black, 6 wt% Kureha 9300 PVDF binder and 0.17 wt% oxalic acid.

Initial electrodes were fabricated with each active material being the sole component to understand the performance of the baseline materials, SLC1520P graphite, SLC1506T graphite and the TODA NMC532 6-micron (μ) particles. These electrodes had a target capacity of ~ 2.5 mAh/cm², which is commensurate with electrodes currently being produced in industry. The Cell Analysis, Modeling and Prototyping (CAMP) Facility at ANL produced the baseline electrodes. There were three anode structures produced: (1) all SLC1520P, (2) all SLC1506T and (3) a 50/50 wt% SLC1520P and SLC1506T blended. There was only one cathode structure that was produced and that was a 100% TODA NMC532 6 μ m electrode. Each of the anode structures were capacity matched with the cathode electrode to make full CR2032 coin cells for electrochemical testing.

The non-baseline anode and cathode electrodes, which were produced by the Battery Manufacturing R&D Facility at ORNL, had the following structured combinations at a higher loading (~ 4.4 mAh/cm²): large particles only, small particles only, blend of large and small particles, a layer of small particles on bottom with

a layer of large particles on top, and a layer of large particles on bottom with a layer of small particles on top. The layered structures were done one of two ways: (1) one layer coated and dried followed by coating a second layer onto the first or (2) both layers coated simultaneously.

The CAMP Facility used their established characterization and cycle life protocols to test the baseline cells along with all high loading couples, and a voltage window of 3V to 4.2V (full cell) was used. The characterization of the coin cells consists of a formation and rate study and HPPC tests. The formation process consists of three cycles at a rate of C/10. The formation and rate study tests consist of two cycles at C/20, three cycles at C/10, three cycles at C/5, three cycles at C/3 charge and C/2 discharge, three cycles at C/3 charge and 1C discharge, and three cycles at C/3 charge and 2C discharge. The HPPC test consists of one cycle at 1C charge and 1C discharge, then nine discharge and charge pulses (at every 10% of capacity) at 3C discharge and 2.25C charge. These three tests make up the cell characterization process. After characterization is complete, the cells were moved onto cycle life testing. The cycle life protocol is as follows: 1) one cycle at C/20 charge and discharge, 2) 47 cycles at C/2 charge and discharge, and 3) the HPPC test. This process is repeated continuously five times creating a 250-cycle loop. Cells are continued in this process until the capacity retention falls below 80% of its initial cycle life capacity.

In this report, we are going to focus on the cycle life data for all cells tested in FY 2017. The first data set examined is for the baseline anode and cathode cells. Figure 1 shows the cycle life graph for the ~2.5 mAh/cm² baseline cells. This is the data set that will establish the desired performance (capacity retention) for comparison to all other cells.

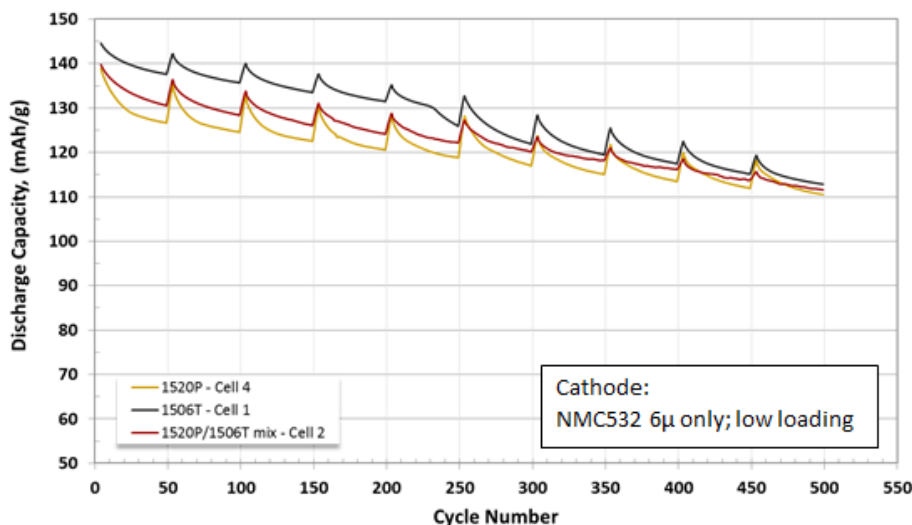


Figure 1. Cycle life plot of baseline electrodes with following active materials: SLC1520P:NMC532 6 μ , SLC1506T:NMC532 6 μ and 50/50 mix SLC1520P/SLC1506T:NMC532 6 μ . These cells were cycled between 3 to 4.2V and are representative cells (capacity based upon grams of cathode material).

From Figure 1, we can establish the cycle number when the capacity of the cells hit the 80% capacity retention. The SLC1520P:NMC532 6 μ m cells reached the 491st cycle, the SLC1506T:NMC532 reached the 441st cycle, and the 50/50 mix SLC1520P/SLC1506T:NMC532 6 μ m cells reached the 496th cycle before they went below 80% capacity retention. The high loading electrode couples will be compared to these cycle numbers.

The first set of non-baseline cells tested used the cathode double pass NMC532 12 μ m in the bottom layer and NMC532 6 μ m in the top layer and was paired with all the various anode structures. Figure 2 shows the cycle life plot for this set of cells.

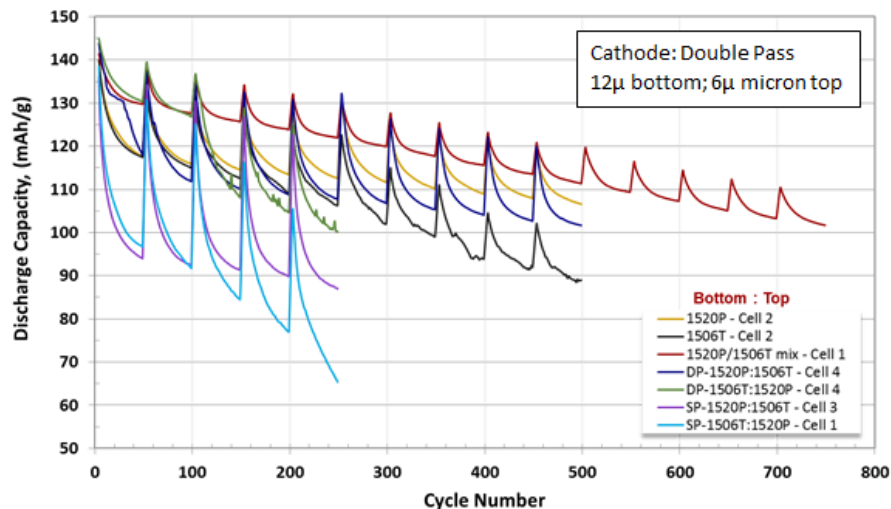


Figure 2. Cycle life plot of cathode double pass NMC532 12μ in the bottom layer and NMC532 6μ in the top layer paired against various anode electrodes. The key to the anodes used is on the graph. These cells were cycled between 3 to 4.2V and are representative cells (capacity based upon grams of cathode material).

The second set of non-baseline cells tested used the 100% NMC532 6 μm only cathode paired with all the various anode structures. Figure 3 is the cycle life plot for this set of cells.

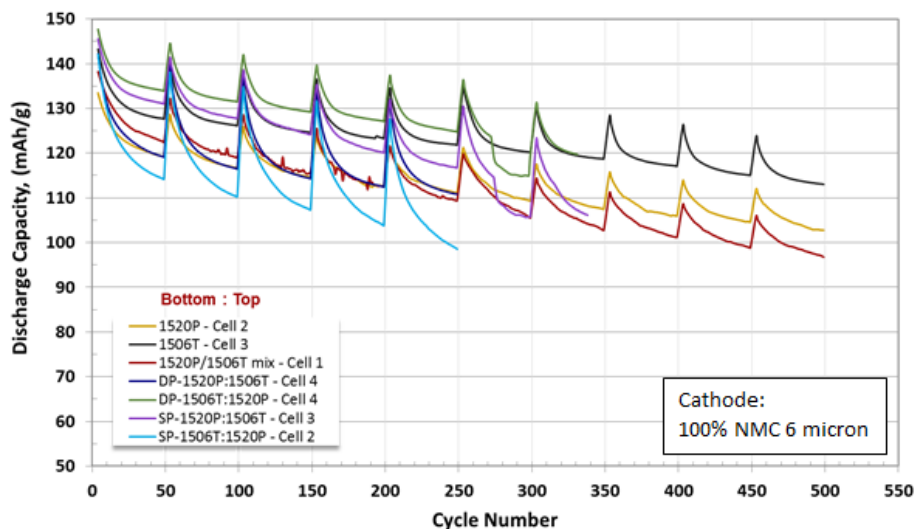


Figure 3. Cycle life plot of the 100% NMC532 6 μm cathode paired against various anode electrodes. The key to the anodes used is on the graph. These cells were cycled between 3 to 4.2V and are representative cells (capacity based upon grams of cathode material).

The third set of non-baseline cells tested used the cathode single pass NMC532 6 μm in the bottom layer and NMC532 12 μm in the top layer paired with all the various anode structures. Figure 4 shows the cycle life plot for this set of cells.

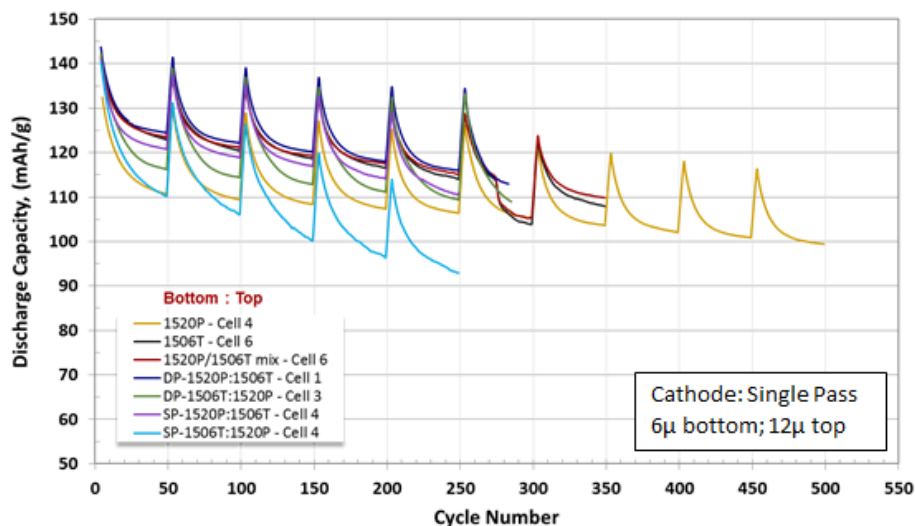


Figure 4. Cycle life plot of cathode single pass NMC532 6 μ m in bottom layer and NMC532 12 μ m in the top layer paired against various anode electrodes. The key to the anodes used is on the graph. These cells were cycled between 3 to 4.2V and are representative cells (capacity based upon grams of cathode material).

The fourth set of non-baseline cells tested used the cathode double pass NMC532 6 μ m in the bottom layer and NMC532 12 μ m in the top layer paired with all the non-layered anode structures. Figure 5 shows the cycle life plot for this set of cells.

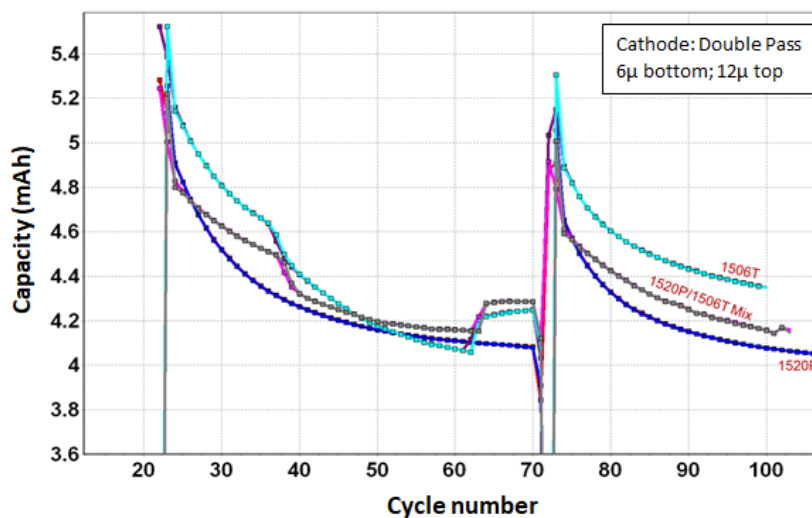


Figure 5. Cycle life plot of cathode double pass NMC532 6 μ m in the bottom layer and NMC532 12 μ m in the top layer paired against various anode electrodes. The key to the anodes used is on the graph. These cells were cycled between 3 to 4.2V and are representative cells (capacity based upon the full coin cell).

Using the data in Figures 1 to 5, a table of the electrode couple's performance can be made to compare the high loading couples to the baseline cells. Table I provides a summary of the performance data for the various compositions of materials and methods of assembly.

Table I. Summary of Electrode Couple Performance from the Cycle Life Data

NMC532 Electrode	Superior Graphite Electrode	Total Number of Cycles Tested on Cells	Representative Discharge Capacity Retention (%)	Cycle at 80% Discharge Capacity Retention (Cycles into Cycle Life)
Baseline: 6 μ m low loading	1520P	522	79.6	491
	1506T	522	78.0	441
	1520P/1506T mix (50/50)	522	79.8	496
DP -12 μ m (B):6 μ m (T)	1520P	522	77.2	385
	1506T	522	63.6	185
	1520P/1506T mix (50/50)	772	71.9	472
	DP – 1520P(B): 1506T(T)	522	70.7	124
	DP – 1506T(B):1520P(T)	272	69.0	124
	SP -1520P(B):1506T(T)	272	63.9	13
	SP – 1506T(B):1520P(T)	272	47.2	15
6 μ m	1520P	522	77.0	386
	1506T	522	78.9	474
	1520P/1506T mix (50/50)	522	70.0	235
	DP – 1520P(B): 1506T(T)	272	77.9	185
	DP – 1506T(B):1520P(T)	356	80.8	Not Yet
	SP -1520P(B):1506T(T)	358	72.9	309
	SP – 1506T(B):1520P(T)	272	69.3	81
SP – 6 μ m (B):12 μ m (T)	1520P	522	75.1	288
	1506T	369	76.3	299
	1520P/1506T mix (50/50)	369	78.0	320
	DP – 1520P(B): 1506T(T)	303	78.6	272
	DP – 1506T(B):1520P(T)	305	76.6	138
	SP -1520P(B):1506T(T)	272	78.7	231
	SP – 1506T(B):1520P(T)	272	66.2	75
DP – 6 μ m (B):12 μ m (T)	1520P	522	74.7	295
	1506T	120	84.6	Not Yet
	1520P/1506T mix (50/50)	120	86.6	Not Yet

Our baseline low loading couples crossed the 80% capacity retention (~112 mAh/g) line between cycles 441 to 496 (also highlighted in yellow in Table II). For the high loading couples to be considered successful, they

should reach the 80% capacity retention and cell capacity (~112 mAh/g) in the same cycle number range as the low loading baseline cells. The top four high loading couples selected from the cells cycling were (1) double pass NMC532 12 μm in the bottom layer/NMC532 6 μm in the top layer: SLC1520P only (2) double pass NMC532 12 μm in the bottom layer/NMC532 6 μm in the top layer: SLC1520P/SLC1506T mixed; (3) NMC532 6 μm only: SLC1520P only; and (4) NMC532 6 μm only: SLC1506T only (highlighted in yellow in Table II). The other cells tested did not fall within the acceptable cycle number range for the 80% capacity retention line. Cycling tests were continued on several of the cells, shown by the red text in Table II, and data is not available for this report.

There are still several high loading structured electrode couples that are cycling and others that need to be tested to determine the maximum performance that can be achieved with these materials and structures. This work will be continued into FY 2018 to finish the complete analysis of this study.

Oak Ridge National Laboratory

Dual Slot Die Setup

Figure 6 shows the components for the dual slot die setup used to make cathode (FY 2016 effort) and anode (FY 2017 effort) coatings designated as #5 and #6 for these studies. Each cylinder contains a separate slurry that is pumped to the slot die and extruded through either the top or bottom slit (shown in the enlarged picture at the bottom). This configuration allows two layers to be coated simultaneously. Conversely, cathode and anode coatings designated as #1- #4 and #7 were made with a single slot die setup, which uses only one cylinder of slurry and a slot die with a single slit.



Figure 6. Dual slot die setup used to make cathode (FY 2016 effort) and anode (FY 2017 effort) coatings (#5 and #6). Each cylinder contains a slurry that is extruded through either the top or bottom slit in the slot die (shown in the enlarged picture), allowing two layers to be coated simultaneously. Source: ORNL

High-Rate Pouch Cell Cycle Life Testing (Cathode Study Initiated in FY 2016)

The high-rate cycle life pouch cell study comparing the six different cathode coatings, while using a baseline anode like the FY 2017 anode coating #1, was completed during the first quarter of FY 2017. The capacity retention for each coating after 1000 cycles at 1C/-2C charge/discharge rates is shown in Figure 7. Although the performance of several of the coatings was similar, cathode coating #3 (2-pass, 12 μm large particles on

bottom/6 μ small particles on top) demonstrated the highest capacity retention after 1000 cycles, while cathode coatings #4 through #6 exhibited the lowest capacity retention.

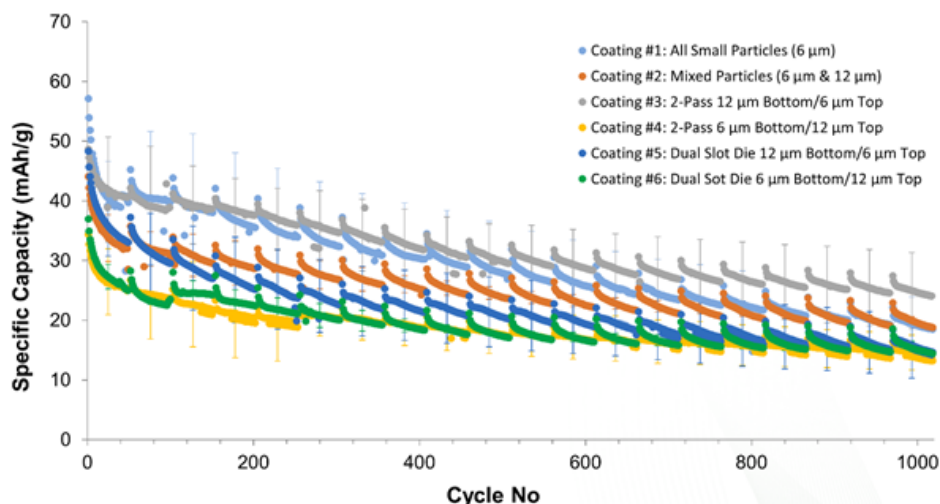


Figure 7. High-rate pouch cell cycle life comparison (1000 cycles) at charge of 1C and discharge of 2C. HPPC was performed every 50 cycles. Each error bar is an average of the standard deviation for those 50 cycles. Data is an average of 3 cells for each coating.

USABC Pouch Cell Cycle Life Testing (Cathode Study Initiated in FY 2016)

The long-term USABC-protocol capacity retention for pouch cells made with each coating was completed in the third quarter of FY 2017 and results are shown in Figure 8. Cathode coatings #1, #2, and #5 exhibit the highest capacity retention (highest for coating #2 at 85%) and smallest cell-to-cell variation through ~1000 cycles at 0.33C/-0.33C charge/discharge rates, while coatings #4 and #6 show the highest capacity fade (lowest capacity retention for Coating #6 at 51%).

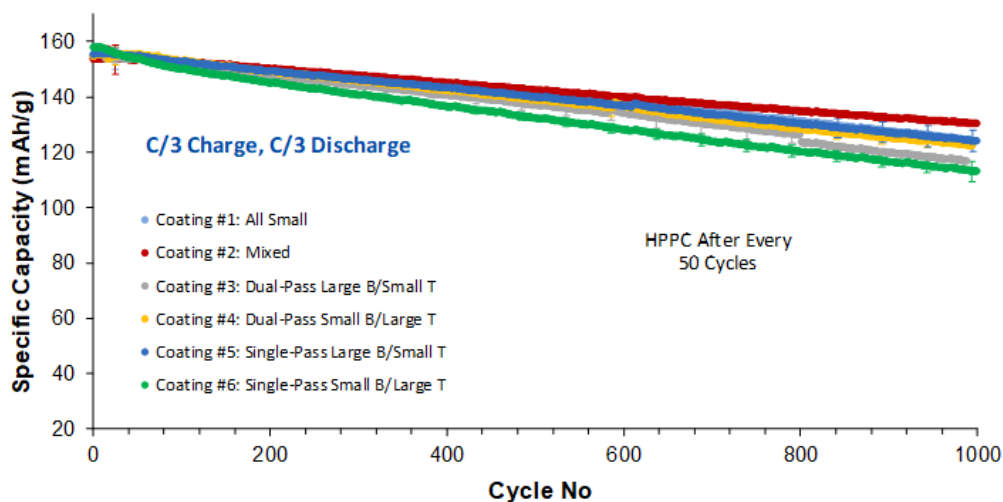


Figure 8. Long-term pouch cell cycle life (~1000 cycles) comparison at charge of C/3 and discharge of C/3. HPPC was performed every 50 cycles. Data is an average of three cells for each coating type except for cathode coatings #4 and #6, which were a 2-cell average, and each error bar is an average of the standard deviation for those 50 cycles.

Pouch Cell Electrolyte Comparison

We have previously shown that the ORNL pouch cells made with the six different cathode coatings exhibited a significantly greater capacity decrease at 2C than the ANL coin cells. Since one possible contributing factor is the different electrolytes used in the two cases, we built coin cells using the same electrolyte used in the ANL cells (1.2 M LiPF₆ in 3:7 wt% EC/EMC) to further investigate its influence. We showed that the capacity of these ORNL coin cells was lower at 2C compared to the ANL coin cells, but they demonstrated improved rate performance relative to the ORNL pouch cells, suggesting that the electrolyte has an important effect. We did not have enough material to make another set of pouch cells with the ANL electrolyte for a more direct comparison. However, we were able to build one pouch cell with coating #1 (all small particles) using the ANL electrolyte to more definitively determine the effect of the different electrolytes in pouch cells.

Figure 9a shows a comparison of the rate performance for pouch cells made with coating #1 using 1.2 M LiPF₆ in 3:7 v/v EC/DEC (average of three cells) and the one pouch cell made with coating #1 using 1.2 M LiPF₆ in 3:7 wt% EC/EMC (ANL electrolyte) (average of three cells with error bars indicating the standard deviation between five cycles at each C rate). The cell made with the ANL electrolyte shows ~1.4× higher capacity retention at 2C. Likewise, the capacity for this cell at 2C matches the capacity of the ORNL coin cells (Figure 9b), suggesting that the previously observed differences between the ORNL coin cells and ORNL pouch cells at 2C can likely be attributed to the different electrolytes used.

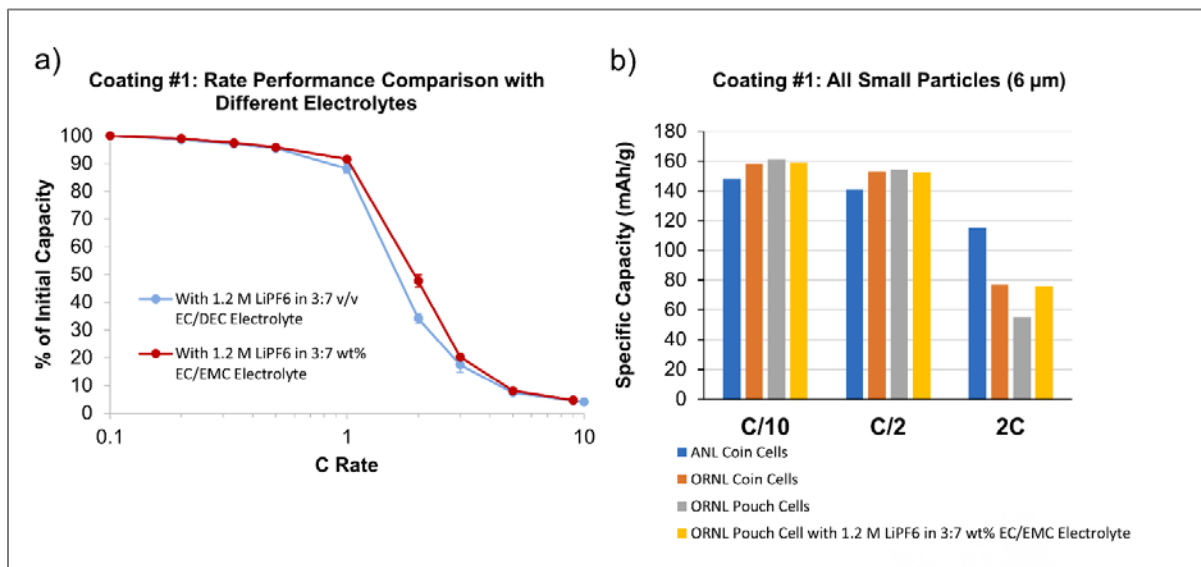


Figure 9. Comparison of pouch cells made with coating #1 (all small particles) using different electrolytes: (a) rate performance comparison between pouch cells made with different and (b) comparison of capacity at C/10, C/2, and 2C discharge rates for ANL coin cells

Improved Pilot Slot-Die Coater Thickness Measurement

This task consisted of watching the coating runs and reviewing the Frontier Dynacoat engineering drawings, performing an extensive literature search on slot-die state-of-the-art and flow and pressure control methods, defining current processing specifications of a slot-die coating method, defining target performance specifications for a modified slot-die coating method, and re-designing a concept for slot-die head with controls and sensors. The new thickness process feedback loop; system identification of process parameters, sensitivity studies, and feedback issues; implementation of a new system with metrology as a function of line speed; linking results with the LBNL modeling effort on coating deposition physics; and determining the alignment of current and target processing specifications were deliverables for 2017. Table II gives the specifications for the existing slot-die coating head and Table III provides the target specifications for the new

slot-die coating thickness feedback control loop. For the new system, values for the parameters are significantly increased.

Table II. Current specifications for existing slot-die coating head

Parameter	Cathode	Anode
Solid loadings in slurry (wt%)	~ 45% (NMP); ~ 60% (aqueous)	~ 45% (NMP); ~ 50% (aqueous)
Slurry viscosity (Pa s)	0.5 - 2	0.5 - 2
Coating speed (ft/min)	2 - 5	2 - 5
Coating deposition shear rate (s^{-1})	30 - 100	30 - 100
Capillary number (Ca)	1 - 5	1 - 5
Coating width (in)	4 - 10	4 - 10
Vacuum level (mm H ₂ O)	2 - 6	2 - 6
Areal loading (mg/cm ²)	6.5 - 38	3.1 - 18
Primary drying temperature (°F)	120 - 190 (NMP); 120 - 270 (aqueous)	120 - 190 (NMP); 120 - 270 (aqueous)
Coating Homogeneity across web (μm)	1 - 5	1 - 5

Table III. Target specifications for new slot-die coating thickness feedback control loop

Parameter	Cathode	Anode
Solid loadings in slurry (wt%)	~ 45% (NMP); ~ 60% - 75% (aqueous)	~ 45% (NMP); ~ 50% - 65% (aqueous)
Slurry viscosity (Pa s)	0.5 - 10	0.5 - 10
Coating speed (ft/min)	5 - 20	5 - 20
Coating deposition shear rate (s^{-1})	20 - 1000	20 - 1000
Capillary number (Ca)	1 - 5	1 - 5
Coating width (in)	4 - 10	4 - 10
Vacuum level (mm H ₂ O)	2 - 6	2 - 6
Areal loading (mg/cm ²)	3 - 45	1.4 - 22
Primary drying temperature (°F)	120 - 190 (NMP); 120 - 270 (aqueous)	120 - 190 (NMP); 120 - 270 (aqueous)
Coating Homogeneity across web (μm)	1 - 3	1 - 3

New Anode Coatings for Structured Anode Study

Seven anodes with structures matching those of the FY 2016 cathodes were slot-die coated according to the compositions listed below. The six cathode coatings from FY 2016 were also repeated to generate enough material for the FY 2017 combined structured anode/cathode pouch cell study. In addition, a seventh cathode was coated using all large (12 μm) particles to serve as a second control (to complement coating #1 made with all small 6 μm particles).

Anode coatings #1, #2, and #7 are all single-layer coatings. Coatings #3 and #4 are two-layer coatings made by a dual pass technique, where the bottom layer is coated and dried before the second layer is coated on top of it. Coating #3 contains large particles on the bottom and small particles on the top, whereas Coating #4 has the opposite configuration. Coatings #5 and #6 are also two-layer coatings and have the same compositions as coatings #3 and #4, but they were made using the dual slot-die, which allows both the bottom and top layers to be coated simultaneously in a single pass.

Anode coating #1: 100% small particles

- 91.83 wt% Superior SLC 1506T graphite
- 2 wt% Timcal C-45 carbon black
- 6 wt% Kureha 9300 PVDF binder
- 0.17 wt% oxalic acid

Anode coating #2: mixed particle sizes (50/50 wt% small/large particles)

- 45.915 wt% Superior SLC 1506T graphite
- 45.915 wt% Superior SLC 1520P graphite
- 2 wt% Timcal C-45 carbon black
- 6 wt% Kureha 9300 PVDF binder
- 0.17 wt% oxalic acid

Anode coating #3: dual pass with bottom layer of large particles and top layer of small particles

- Bottom layer slurry
 - 91.83 wt% Superior SLC 1520P graphite
 - 2 wt% Timcal C-45 carbon black
 - 6 wt% Kureha 9300 PVDF binder
 - 0.17 wt% oxalic acid
- Top layer slurry
 - 91.83 wt% Superior SLC 1506T graphite
 - 2 wt% Timcal C-45 carbon black
 - 6 wt% Kureha 9300 PVDF binder
 - 0.17 wt% oxalic acid

Anode coating #4: dual pass with bottom layer of small particle sizes and top layer of large particles

- Bottom layer slurry
 - 91.83 wt% Superior SLC 1506T graphite
 - 2 wt% Timcal C-45 carbon black
 - 6 wt% Kureha 9300 PVDF binder
 - 0.17 wt% oxalic acid
- Top layer slurry
 - 91.83 wt% Superior SLC 1520P graphite

- 2 wt% Timcal C-45 carbon black
- 6 wt% Kureha 9300 PVDF binder
- 0.17 wt% oxalic acid

Anode coating #5: single pass (dual slot-die) with bottom layer of large particles and top layer of small particles

- Bottom layer slurry
 - 91.83 wt% Superior SLC 1520P graphite
 - 2 wt% Timcal C-45 carbon black
 - 6 wt% Kureha 9300 PVDF binder
 - 0.17 wt% oxalic acid
- Top layer slurry
 - 91.83 wt% Superior SLC 1506T graphite
 - 2 wt% Timcal C-45 carbon black
 - 6 wt% Kureha 9300 PVDF binder
 - 0.17 wt% oxalic acid

Anode coating #6: single pass (dual slot die) with bottom layer of small particles and top layer of large particles

- Bottom layer slurry
 - 91.83 wt% Superior SLC 1506T graphite
 - 2 wt% Timcal C-45 carbon black
 - 6 wt% Kureha 9300 PVDF binder
 - 0.17 wt% oxalic acid
- Top layer slurry
 - 91.83 wt% Superior SLC 1520P graphite
 - 2 wt% Timcal C-45 carbon black
 - 6 wt% Kureha 9300 PVDF binder
 - 0.17 wt% oxalic acid

Anode coating #7: 100% large particles

- 91.83 wt% Superior SLC 1520P graphite
- 2 wt% Timcal C-45 carbon black
- 6 wt% Kureha 9300 PVDF binder
- 0.17 wt% oxalic acid

Rheological Properties of Anode and Cathode Slurries

Since slurry rheology can affect the resulting electrode microstructure, the rheological properties of the anode and cathode slurries used for the slot-die coatings were measured to assess any significant differences. The results are shown in Figure 10. For the anodes, the Superior SLC 1506T (6 μ m small particles) slurry was 45.3 wt% solids, and the Superior SLC 1520P (12 μ m large particles) and Superior SLC 1506T/1520P (mixed small/large particles) slurries were both 45.5 wt% solids. All cathode slurries were 42 wt% solids. The viscosity of the large particle (Superior SLC 1520P) anode slurry is slightly lower than that of the other two anode slurries at low shear rates, but all three slurries show very similar shear-thinning behavior with increasing shear rate. Similarly, the viscosity of the large particle NMC 532 cathode slurry is slightly higher than the other two cathode slurries at low shear rates, but all three slurries show very similar shear-thinning behavior with increasing shear rate.

The different trends that were observed between the anode and cathode viscosities with increasing shear rate (i.e. smaller anode particles had highest viscosity, and larger cathode particles have highest viscosity) is likely due to the significantly different surface chemistries and particle morphologies of the anode graphite and cathode NMC 532. The mixed cathode particle slurry showed the lowest viscosity, which could be due to better packing of particles in the slurry; however, this hypothesis needs further investigation.

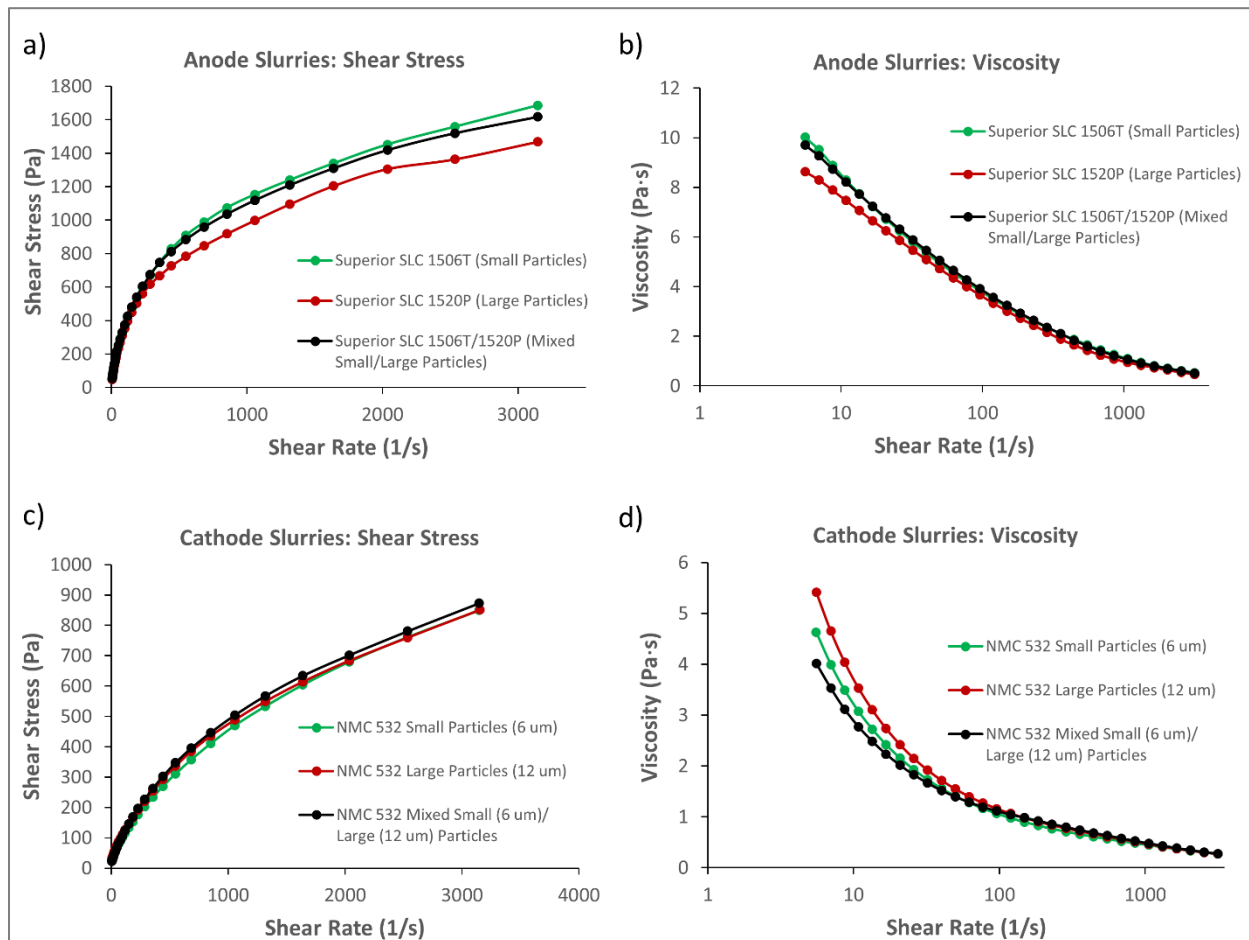


Figure 10. Rheological properties of anode (a & b) and cathode (c & d) slurries used for slot-die coatings in terms of shear stress versus shear rate ((a) and (c)) and viscosity versus shear rate ((b) and (d))

Single-Layer Pouch Cells with Structured Anodes and Cathodes

Single-layer pouch cells (~170 mAh) were assembled using seven different structured anode and cathode coatings. Due to the large number of anode/cathode combinations to be tested and limited potentiostat availability, cells were made and tested in batches. For the first batch, cathode #1 (all small 6 μ m particles) and cathode #3 (dual-pass with large 12 μ m particles bottom and small 6 μ m particles top) were each paired with all seven anodes. Cells for every combination were made in triplicate and subjected to both charge and discharge rate performance testing (discharge first, followed by charge). Details of both protocols are given below.

Formation (2.5V to 4.2V): 4 cycles at charge C/20, discharge C/20

Discharge rate performance protocol (2.5V to 4.2V):

- 5 Cycles at charge C/5, discharge C/10
- 5 Cycles at charge C/5, discharge C/5
- 5 Cycles at charge C/5, discharge C/3
- 5 Cycles at charge C/5, discharge C/2
- 5 Cycles at charge C/5, discharge 1C
- 5 Cycles at charge C/5, discharge 2C
- 5 Cycles at charge C/5, discharge 3C
- 5 Cycles at charge C/5, discharge 5C
- 5 Cycles at charge C/5, discharge 10C
- 5 Cycles at charge C/5, discharge C/5

Charge rate performance protocol (2.5V to 4.2V):

- 5 Cycles at charge C/10, discharge C/5
- 5 Cycles at charge C/5, discharge C/5
- 5 Cycles at charge C/3, discharge C/5
- 5 Cycles at charge C/2, discharge C/5
- 5 Cycles at charge 1C, discharge C/5
- 5 Cycles at charge 2C, discharge C/5
- 5 Cycles at charge 3C, discharge C/5
- 5 Cycles at charge 5C, discharge C/5
- 5 Cycles at charge 10C, discharge C/5
- 5 Cycles at charge C/5, discharge C/5

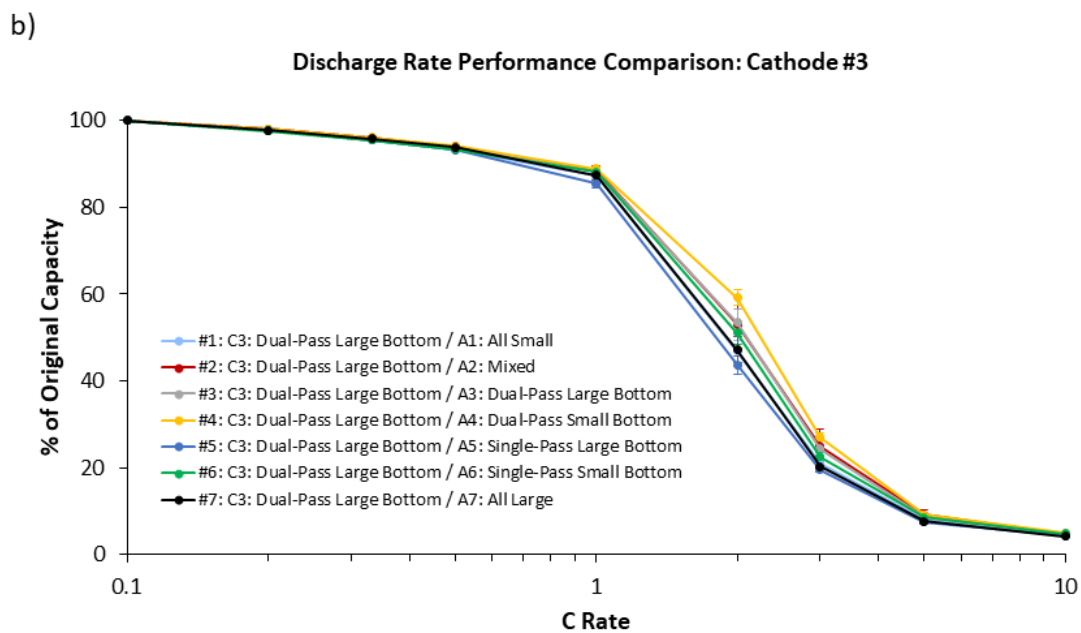
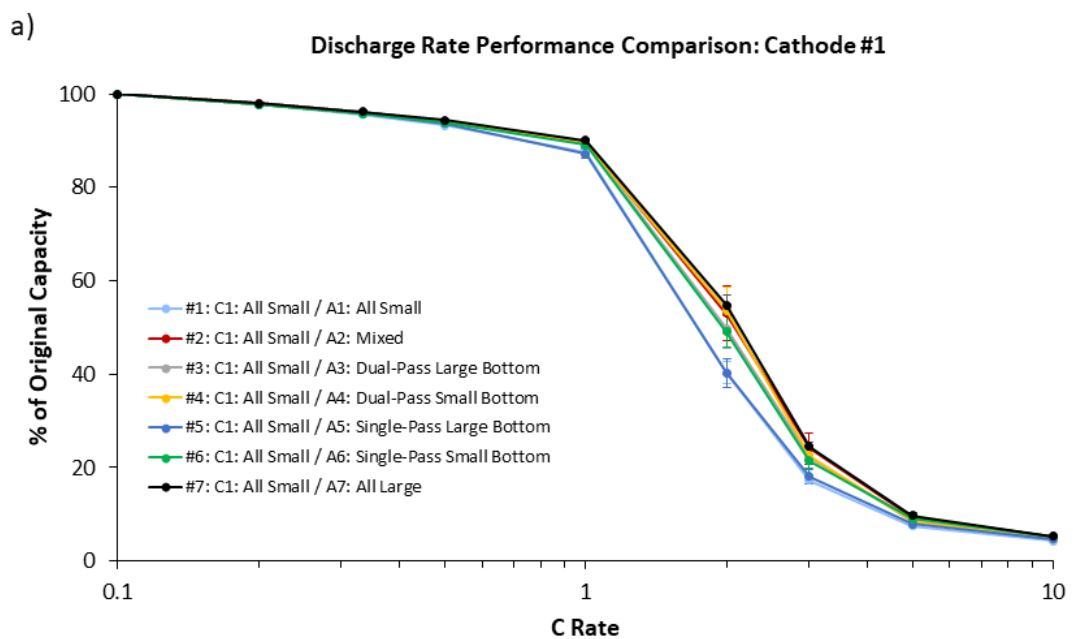
Discharge Rate Performance

The discharge rate performance results for cathode #1 and cathode #3 are shown in Figure 11a and Figure 11b. Some differences can be observed in the 2C and 3C discharge capacities of cells made with cathode #1 and different anodes. Cells made with anode #2 (mixed particles), anode #4 (dual-pass with small particles on bottom and large particles top), and anode #7 (all large particles) demonstrated the best performance, reaching ~50-55% of the original capacity at 2C. In contrast, cells made with anode #1 (all small particles) and anode #5 (single-pass with large particles on bottom and small particles on top) demonstrated the worst performance, achieving only ~40% of the original capacity at 2C. The results for cells assembled with cathode #3 are similar, with those made using anode #4 maintaining ~59% of the original capacity at 2C and those made using anode #5 reaching only ~44% of the original capacity.

Results for all the anode/cathode combinations are plotted in Figure 11c for comparison. The best performing combination in this first batch of cells is cathode #3 with anode #4 (~59% of original capacity at 2C), while the worst combinations are cathode #1 with anode #5 and cathode #1 with anode #1 (~40% of original capacity at 2C). These results suggest that certain electrode architecture combinations do improve the rate performance at high C rates.

Comparing both two-layer anode configurations, cells made with anodes containing small particles on the bottom and large particles on the top (anodes #4 and #6) generally have a higher capacity at 2C than those made with anodes in the opposite configuration (anodes #3 and #5). In addition, the performance of cells containing two-layer anodes coated using the dual-pass approach is, in general, marginally better than that of cells containing anodes coated using the single-pass method (although they are very similar). Interestingly, the structured cathode rate performance results from FY 2016 (all made with anode #7), showed the opposite trend from these structured anode cells; those made using cathodes with small particles on the bottom and large particles on the top had lower capacities at 2C than those made using cathodes with the reverse configuration. Each data point is an average of three pouch cells, with the initial capacity taken as the capacity at a discharge

rate of C/10. The error bars represent the standard deviation at each C rate. All cells were filled with 1.2 M LiPF_6 in 3:7 wt% EC/EMC electrolyte.



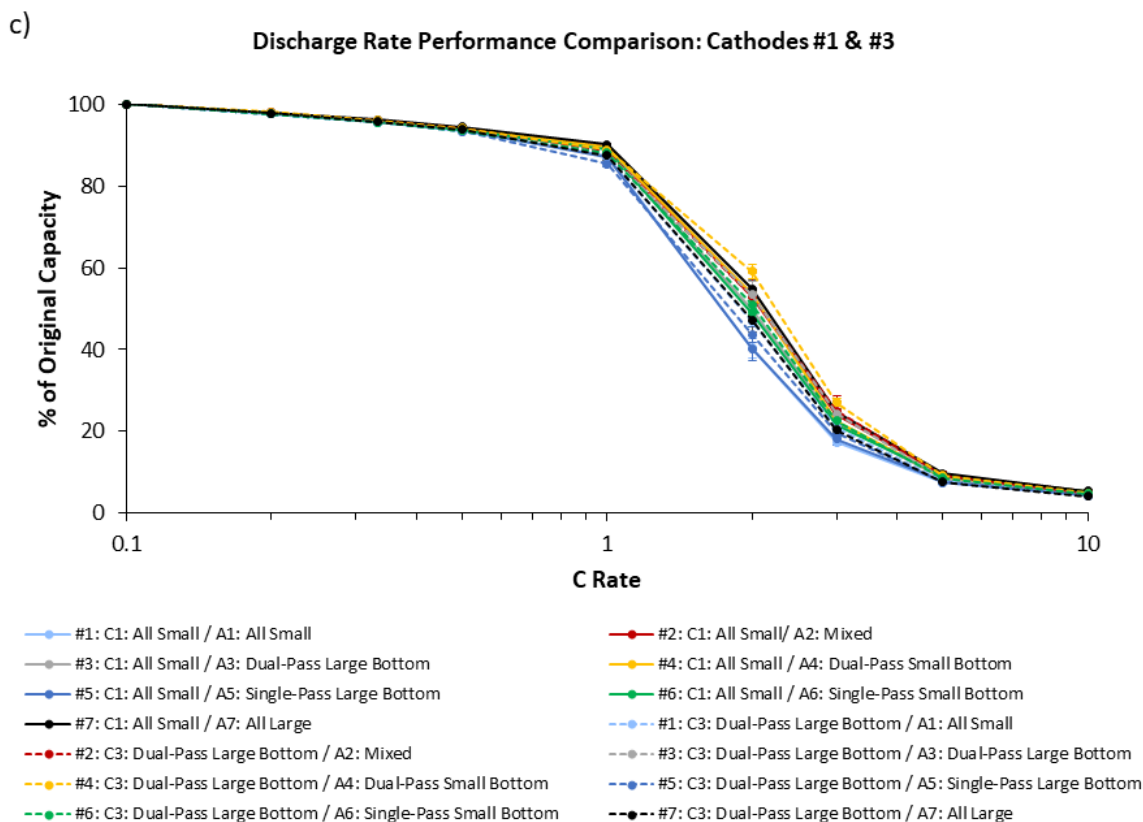


Figure 11. Discharge rate performance comparison for single-layer pouch cells made with (a) cathode #1 (all small particles) and (b) cathode #3 (dual-pass with large particles on the bottom and small particles on top) and seven different anode coatings; and (c) comparison of all cells made with cathodes #1 and #3

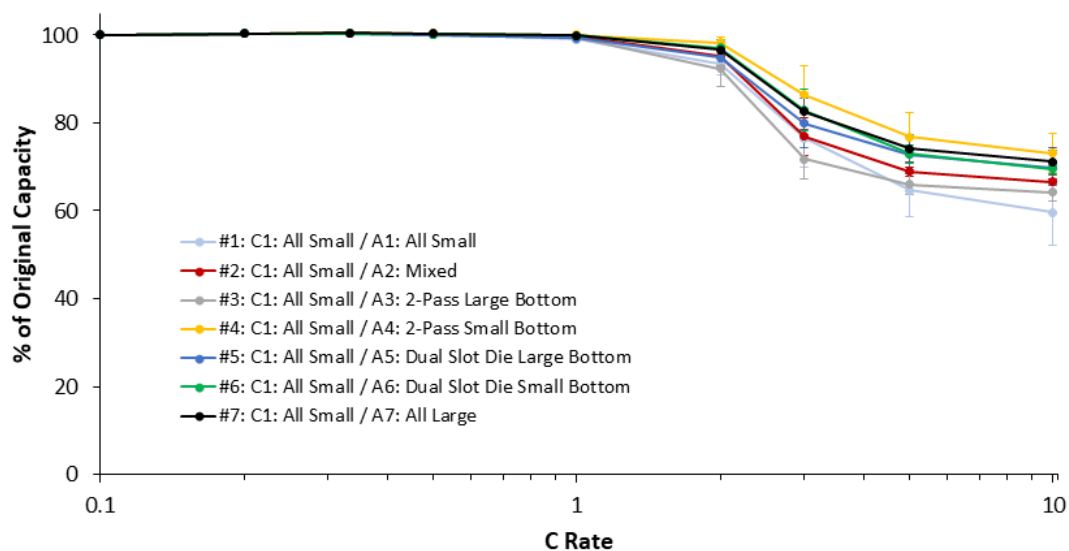
Charge Rate Performance

The charge rate performance results for cathode #1 and cathode #3 are shown in Figure 12a and Figure 12b. While the capacity of all cells decreases at charge rates $\geq 3C$, the capacity loss is not nearly as significant as that observed for high discharge rates. Like the discharge results, anode #4 (dual-pass with small particles on the bottom and large particles on top) was the best performing anode for cells made with both cathodes. Likewise, anode #1 (all small particles) was one of the worst performing anodes. However, for cells made with cathode #3, anode #3 (dual-pass with large particles on the bottom and small particles on top) was one of the *worst* performing anodes at high charge rates; whereas, it was one of the *best* performing anodes at high discharge rates.

The results from all cells made with both cathodes are plotted together for comparison in Figure 12c. Cells made with cathode #3 all performed better (~ 73 - 87% of the original capacity at $5C$) than cells made with cathode #1 (~ 65 - 77% of original capacity at $5C$), indicating that the cathode also influences charge rate performance. There is no discernible difference between the charge performance of anodes made with the dual-pass and single-pass methods, but the anodes with small particles on the bottom and large particles on top (anodes #4 and #6) again generally performed better than those with the opposite configuration (anodes #3 and #5). Each data point is an average of three pouch cells, with the initial capacity taken as the capacity at a charge rate of $C/10$. The error bars represent the standard deviation at each C rate. All cells were filled with 1.2 M LiPF_6 in $3:7\text{ wt\% EC/EMC}$ electrolyte.

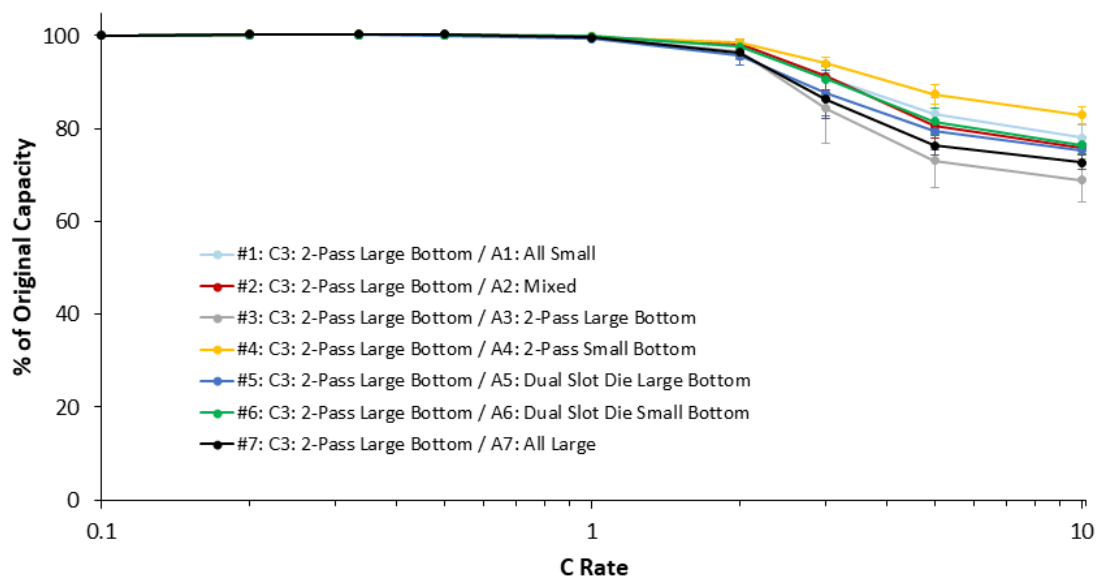
a)

Charge Rate Performance Comparison: Cathode #1



b)

Charge Rate Performance Comparison: Cathode #3



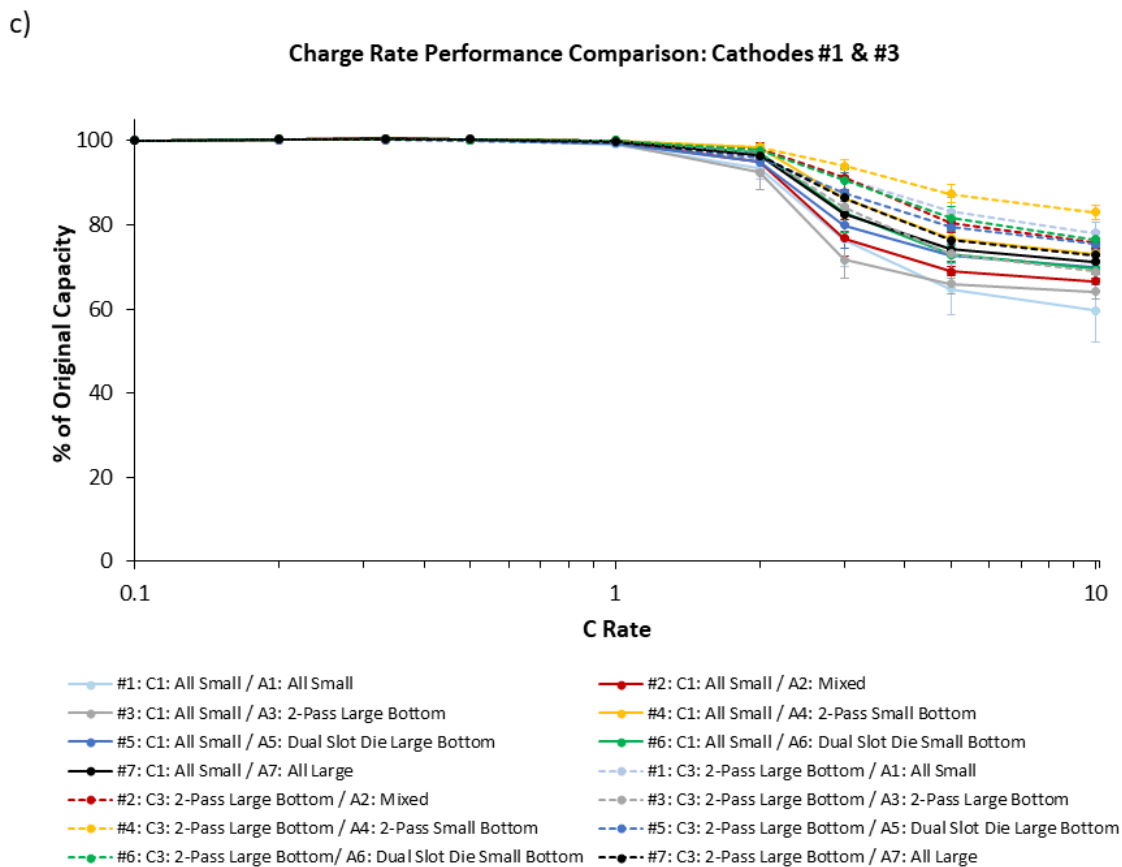


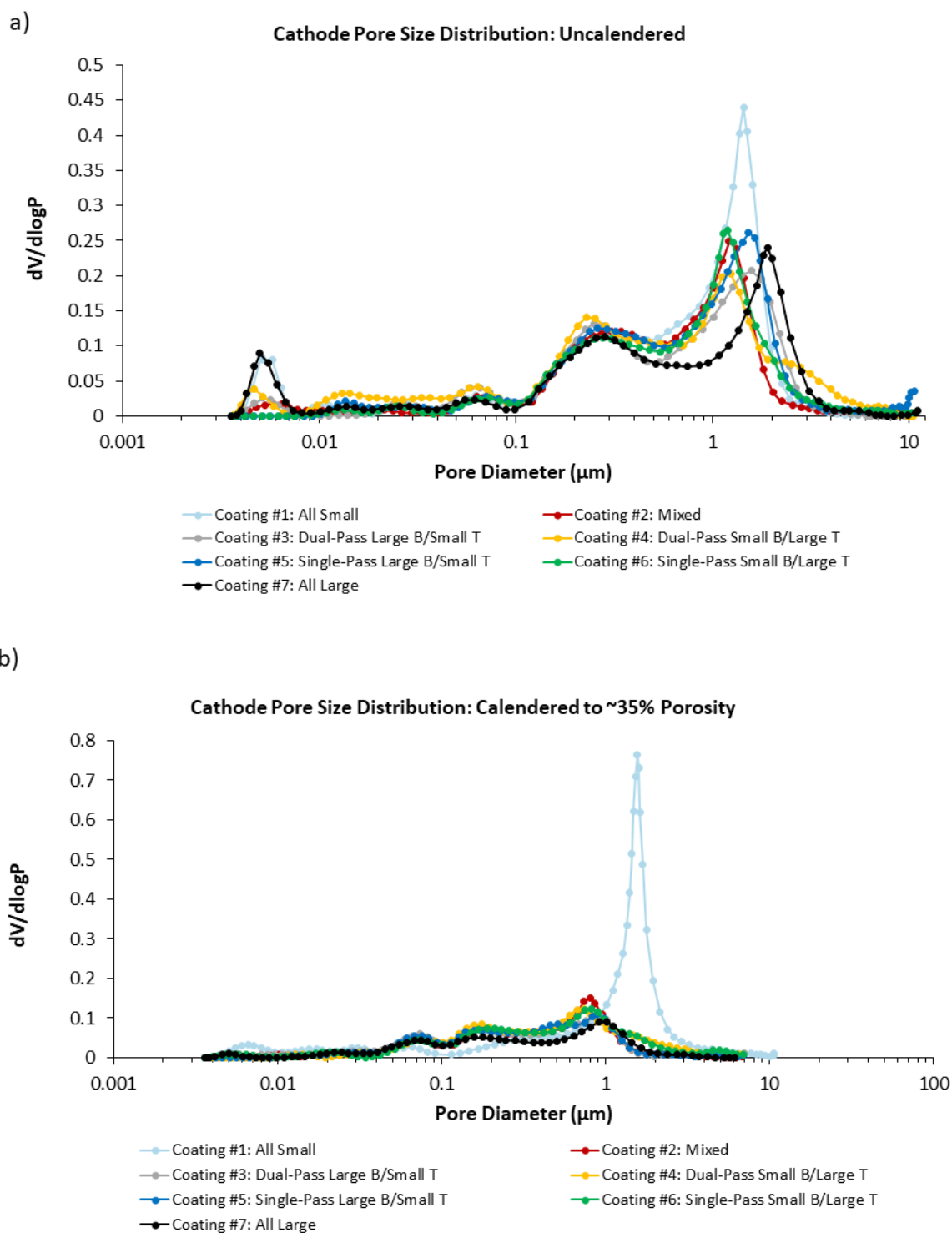
Figure 12. Charge rate performance comparison for single-layer pouch cells made with (a) cathode #1 (all small particles) and (b) cathode #3 (dual pass with large particles on the bottom and small particles on top) and seven different anode coatings. (c) Comparison of all cells made with both cathode #1 and cathode #2.

Mercury Porosimetry Tests

Figure 13 shows the pore size distributions for all seven cathodes and anodes obtained from mercury porosimetry testing before and after calendaring. In general, the pore diameters seem to be a little larger for the anodes compared to the cathodes. All the uncalendered cathode distributions follow similar trends, each showing two main peaks between 0.1 and 10 μm , except for coating #4 (dual-pass with small particles on the bottom and large particles on top), which shows three peaks in this region (Figure 13a). Cathode #7 (all large particles) seems to have slightly larger pores than the others (as expected due to the larger particle size). After calendaring, these peaks all shift to slightly smaller pore diameters and decrease in height (except for cathode #1), confirming the lower overall porosity (Figure 13b). It is unclear why a large peak around 1.5 μm pore diameter remains for cathode #1 after calendaring.

The uncalendered anode results show more variation, with all the single-layer coatings (anodes #1, #2, and #7) displaying only one major peak between 1 and 10 μm , and all the two-layer coatings (anodes #3 through #6) displaying two peaks in this region (Figure 13c). Like cathode #7, anode #7 (all large particles) has larger pores in this range compared to the other coatings. Both dual-pass coatings (anodes #3 and #4) also show considerable peaks at very small pore diameters ($<0.01 \mu\text{m}$), but these are most likely a consequence of the measurement process. Calendaring again causes a decrease in the peak heights and a shift in the locations toward slightly smaller pore diameters, confirming the lower porosity (Figure 13d). However, all the two-layer anode structures maintain their bimodal distribution in the 1-10 μm region except anode #3 (dual-pass with large particles on the bottom and small particles on top), which only shows a single peak after calendaring.

Overall, the results show that pairing structured cathodes with structured anodes results in some rate performance improvement at higher charge and discharge rates.



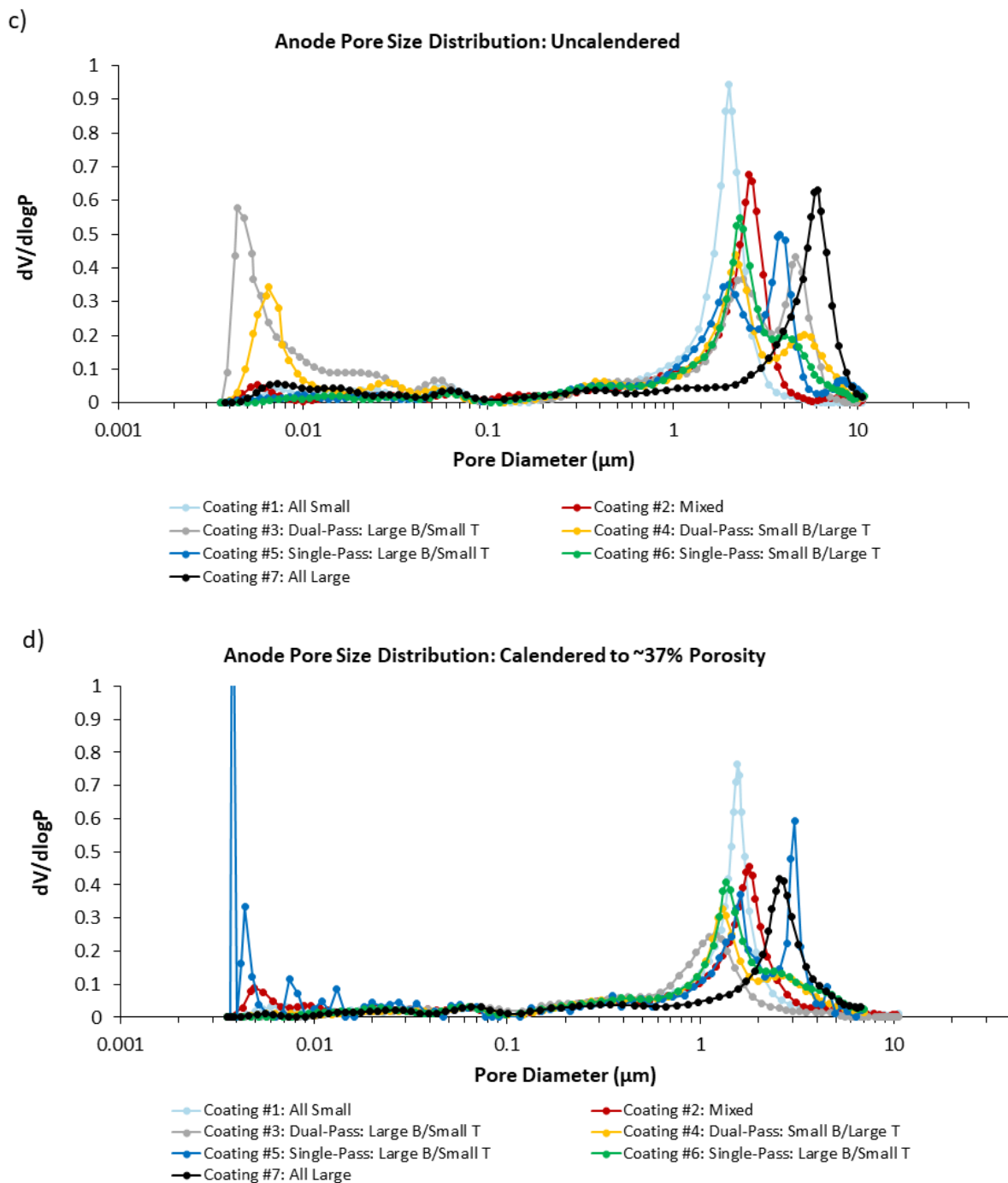


Figure 13. Cathode and anode pore size distributions measured by mercury porosimetry: (a) uncalendered cathode coatings, (b) calendered cathode coatings, (c) uncalendered anode coatings, and (d) calendered anode coatings

Discharge Rate Performance

General discharge performance trends are opposite for the structured cathodes and anodes as shown in Figure 14. Anode #1 (all small particles) and anode #5 (single-pass with large particles on the bottom and small particles on the top) show the *worst* performance, but cathode #1 (all small particles) and cathode structures

with large particles on the bottom (#5 and #3) show the *best* performance. Anode #4 (dual-pass with small particles on the bottom and large particles on the top) shows the *best* performance, but *cathode* structures with small particles on the bottom (#4 and #6) show the *worst* performance.

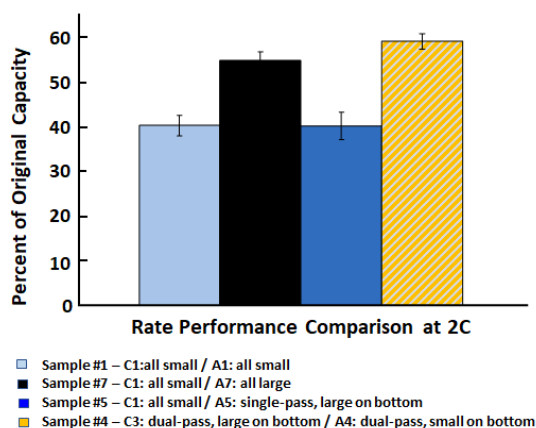


Figure 14. Fraction of rated capacity (C/10 discharge rate) for three different structured cathode/anode combinations as compared to cathode #1 - anode #1 (C1/A1) baseline

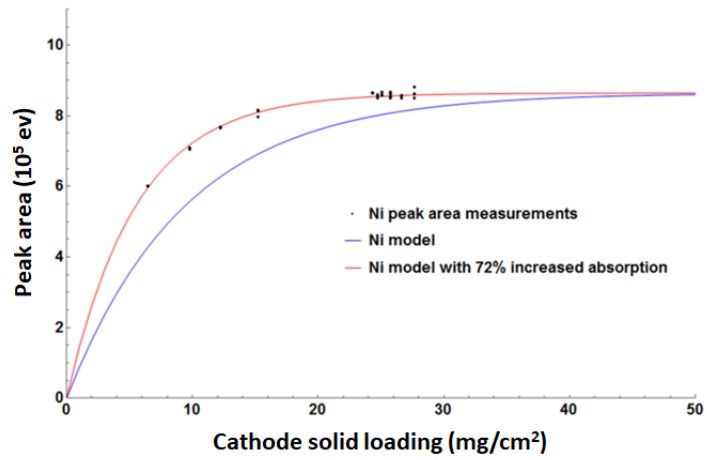
National Renewable Energy Laboratory

Tasks for XRF analysis of cathode loadings and the ORNL and NREL cathode in-line porosity measurements were completed. The technique for the electrode thermal conductivity measurements was tested and initial measurements made. The technique feasibility for the electrode emissivity measurements was tested; however, further testing is pending availability of equipment.

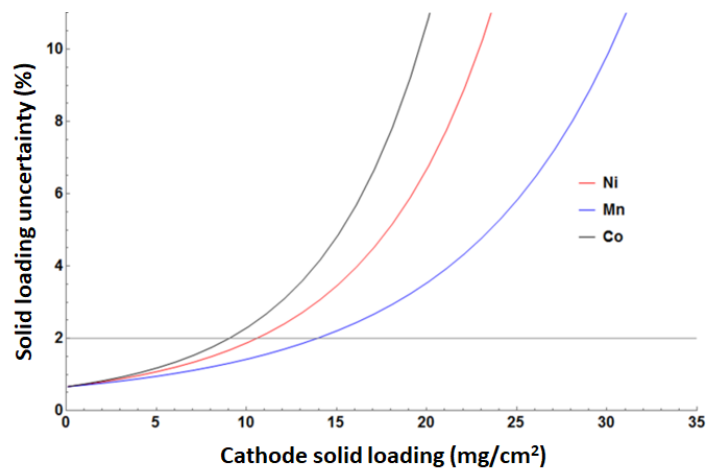
XRF Analysis of Cathode Areal Loading to Define Sensitivity of XRF System to Active Metals

NREL performed detailed analysis of XRF spectra of battery cathodes from this project to explore the accuracy of the data and the correlation between loading and signal. The data correlated well with known cathode active material loading for low loaded samples, i.e. below $\sim 20 \text{ mg/cm}^2$, but for the thicker, higher loaded samples, the measurement was insensitive (constant) to loading. This led to a modeling analysis of the penetration depth of the x-ray beam as a function of the materials and density of the cathode layer. The analysis confirmed that the current system is penetration-depth limited for these materials. However, across a range of low-loaded cathode samples, the data had an accuracy of within 3% of known loading, which was an improvement over the prior ORNL results.

In further analysis, we additionally used the penetration-depth model to develop a correlation between measurement uncertainty and loading for NMC cathodes, and to predict the XRF response (e.g. peak area) for an alternate XRF measurement system with the capability for greater penetration into the thick cathode electrodes. Figure 15a shows fitting of the penetration depth model to the experimental data (for Ni, in this example), and Figure 15b gives the measurement uncertainty calculations as a function of areal loading for the three active metals. Figure 16 shows the predicted high-loading XRF response for a measurement system with greater penetration depth. The XRF has also been used in several PEMFC studies to measure electrode platinum loadings, which will be good preparation for future core lab work on fuel cell electrodes.



(a)



(b)

Figure 15. Cathode solid loading as a function of (a) the penetration depth model for Ni and (b) measurement uncertainty calculations

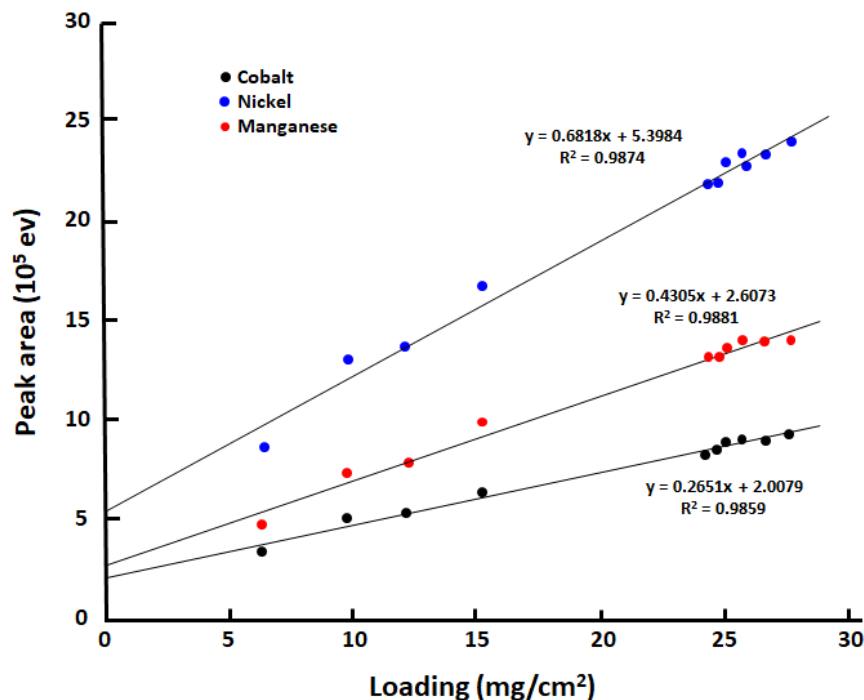
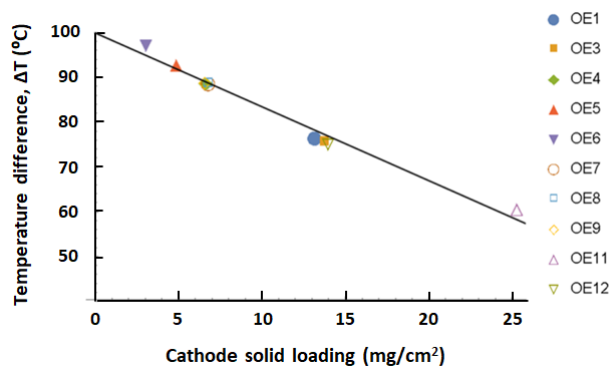


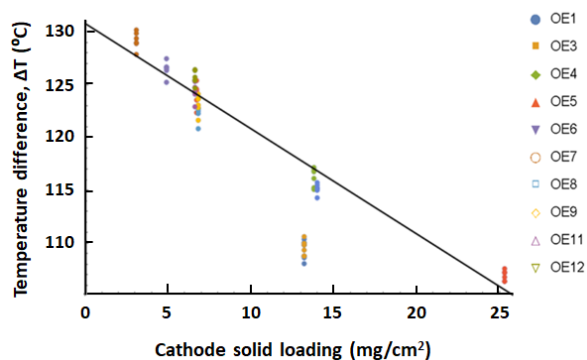
Figure 16. XRF analysis of cathode areal loadings

Battery Cathode Porosity Diagnostic Data Analysis for ORNL Coating Run and Follow-On Runs of Cathode Sheets on the NREL Web-Line

An analysis was performed on the in-line porosity data taken on the cathode samples coated at ORNL. Samples were coated at nine different active material loadings, using three slurry solids loadings and three coating speeds. These cathode samples were also run on the NREL web-line to get a more stable data set. The data analysis evaluated the technique response as a function of infrared (IR) wavelength band. For the measured responses in the mid-IR region ($\sim 3\text{-}5 \mu\text{m}$), several of the cathodes did not fit the predicted response due to differences in surface roughness/emissivity in that wavelength band, whereas all samples fit the predicted response in the far-IR region ($\sim 7\text{-}14 \mu\text{m}$). All the cathode samples were modeled and the expected correlation between thermal response and loading was observed. The modeling indicates that the technique may be very sensitive to active material loading in addition to porosity. Figure 17a shows the modeled thermal responses of the 10 coated cathodes, and Figure 17b gives the measured thermal responses of the samples in the mid-IR region showing the sensitivity of the responses in this wavelength band to slight differences in emissivity. From this work, a joint NREL-ORNL paper on the in-line porosity diagnostic methodology and initial validation was published (Rupnowski, et al. 2017) and a joint patent application was filed (Sopori 2016).



(a)



(b)

Figure 17. (a) Porosity model thermal responses for the 10 coated cathodes and (b) thermal responses in the mid-IR (~3 - 5 μm) range for the 10 coated cathodes showing the sensitivity of the responses in the wavelength band to slight differences in emissivity in some of the samples

Thermal Conductivity and Emissivity Measurements of Cathode Materials to Validate and Enhance Porosity Model Predictions

Initial measurements of thermal conductivity of battery cathode materials were performed using a laser-based testbed at NREL. The data analysis will continue into FY 2018. An analysis of feasibility for using an FTIR-based technique for battery cathode emissivity measurement was also performed. We understand the technique to be feasible for the measurement; however, the NREL device was inoperative due to required maintenance, and testing will resume when the device is operational.

Citrine

Citrine's predictive model on cathode material synthesis developed in FY 2016 was evaluated and their basic computational work frame was determined to be reasonable and works well but needs more data to increase accuracy of predictions. The initial contract effort with Citrine for data mining and analysis was concluded. Expenditures for the second quarter FY 2017 were for wrapping up work performed on end-of-contract services for the two historical projects (Task 1: Analyze the JCI data and establish a model and Task 2: Analyze the battery materials synthesis and develop a model) and work toward preparing a proposal for follow

on tasking. Many of these extensions are related to self-service features, including the ability for staff scientists to monitor model performance, add new data, and retrain models.

Discussions were held with Kodak to explore the possibility of leveraging the data generated by Kodak's pilot coater to see if there was a potential opportunity for a collaboration with Citrine. Kodak described a possible project, but they needed to determine if there was going to be an issue related to the intellectual property rights of the data and if it could be used for this purpose. This collaboration opportunity will be further pursued, and discussions will be coordinated between Kodak and Citrine in FY 2018.

After a discussion with Citrine, it was proposed to focus the modeling effort on a fuel cell based task that would have additional data available for a more accurate model. Citrine was asked to provide a detailed proposal for this work, including milestones and deliverables; however, after further discussions with Citrine and the fuel cell team, the available data from a fuel cell based project would not be sufficient for an accurate predictive model. Therefore, the fuel-cell-based model concept was postponed until a larger data set could be identified.

Fuel Cell Study

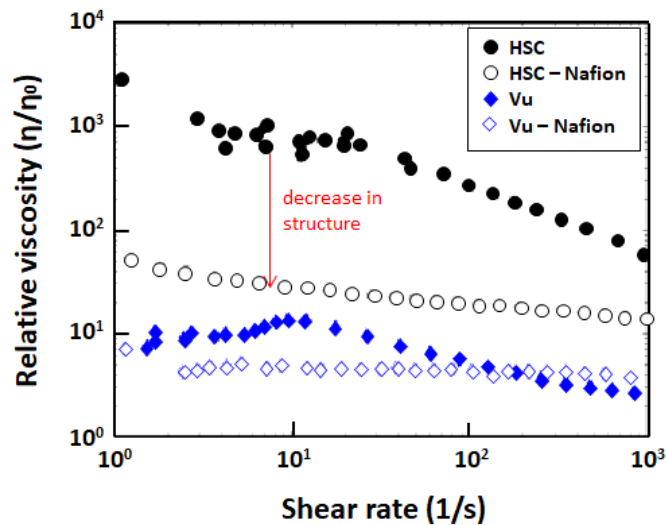
National Renewable Energy Laboratory

NREL is the lead consortium laboratory for the Fuel Cell Study effort. The objective of the study is to explore phase-separation and other single-coating-layer methodologies to achieve an ionomer-rich GDE surface. To meet this objective, NREL will study and characterize relevant electrode ink parameters, study the impact of coating parameters and types on GDE morphology, fabricate MEAs from coated GDEs, test the MEAs performance, interact with ORNL on ink studies, dual-slot coating and high-resolution electron microscopy, and interact with ANL for the USAXS and XCT advanced characterizations.

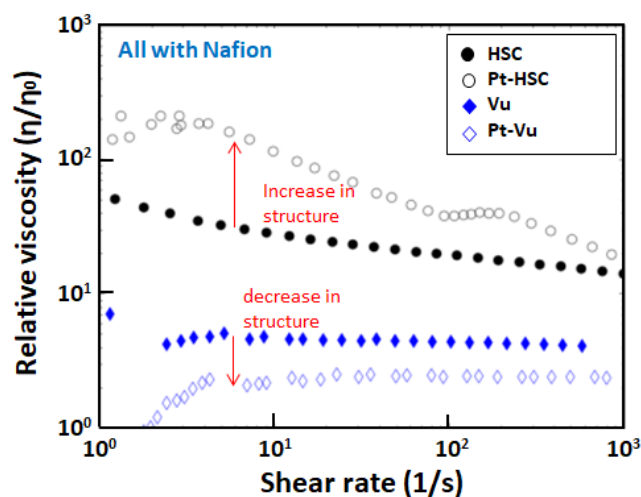
Phase-separation and other single-coating methodologies to achieve an ionomer-rich GDE surface

GDEs are recently garnering high interest in the industry as an alternate or possibly combined fabrication pathway for MEAs, with the more standard catalyst-coated membrane (CCM) approach. GDEs provide a different set of fabrication and performance variables that may provide improved performance and lifetime in some cases. However, fabrication of MEAs based on GDEs can require different material structures than CCMs, and, for scaling of GDE-based MEAs, this means potentially different process techniques and conditions. For example, an additional layer of ionomer is often required between the GDE electrode and membrane to achieve comparable performance to CCMs. The goal of this project is to explore, understand and optimize material and process parameters for scalable processes to support increased throughput, increased quality, and reduced cost for high volume production of MEAs.

This task began by performing detailed ink rheology studies to explore how particle-polymer interactions in the inks at the nano- and micro-scale affect the macro-scale viscoelastic behavior of the ink, which impacts coatability and ultimate structure and morphology of the electrode. This work was done within the context of understanding aspects of the ink that would help enable this target ionomer gradient, e.g. inter-particle forces and solvent evaporation rates. Figure 18a shows the effect of the addition of the ionomer to the bare support particles in solvent for two types of carbon support, and Figure 18b shows the impact that the platinum catalyst has on the ink structure, depending on the type of support. The difference in ink structure as a function of carbon support type was not expected and bears further study. Addition of Nafion results in similar decrease in structure regardless of carbon type. Addition of Pt results in opposite changes in viscosity depending on the carbon type. This indicates there may be a difference in the way the Nafion is adsorbing to the Pt/carbon surface, which may be dependent on the location of catalyst sites or the treatment of carbon surface during catalyst deposition.



(a)



(b)

Figure 18. Catalyst ink structure dependency on carbon type and Pt: (a) effect of the addition Nafion ionomer and (b) impact of Pt catalyst on ink structure

In addition to rheology, dynamic light scattering, and zeta potential measurements were used to characterize particle size and stability of dilute catalyst inks. Dynamic secondary ion mass spectroscopy was also investigated for through-the-thickness element mapping of the electrodes. This technique was of limited quantitative value because of the difficulty of calibrating depth in these heterogeneous materials.

As a baselining first step, the studied inks were used to fabricate ultrasonic sprayed GDEs, with and without ionomer overcoat layer. Testing of the performance of the sprayed GDEs with ionomer overcoat showed that they were comparable to that of our catalyst-coated membrane standards.

A series of exploratory bar and rod coating studies of electrode inks of different compositions (ionomer-to-carbon ratio and solvent mixture ratio) were then performed. These GDEs were prepared with the following parameters: the diffusion media was SGL 29BC, the catalyst loading in the dried electrode was 0.15 – 0.2 mg/cm², the catalyst was 50 wt% Pt/HSC and a concentration of 3 wt% Pt/HSC, the ionomer to carbon ratio was varied, the solvents were water and n-propanol, the drying was done with either a convection oven or a fume hood, and the sample area was 10 cm by 12 cm. Samples were dried under various conditions and with both air and IR sources. Because of these studies, we realized the need for a quick screening tool for surface composition, and initiated development of an analytical method to measure the electrode surface ionomer content based on the Kelvin Probe technique that measures the contact potential difference (work function) of the surface. When there is a significant difference between the work functions of two materials, Kelvin probe provides a measure of the surface composition. To our knowledge, this technique has not previously been used in this way for fuel cell materials. Figure 19a gives the Kelvin probe data for electrode inks of different ionomer-to-carbon ratios and different solvent ratios (H₂O/n-propanol) that were dried at different drying temperatures. The dashed line at the top shows the value for an electrode with a separate ionomer overcoat (i.e. the target). Figure 19b illustrates the in-situ performance of the rod-coated GDEs. We observed that the Kelvin Probe data correlates well with performance.

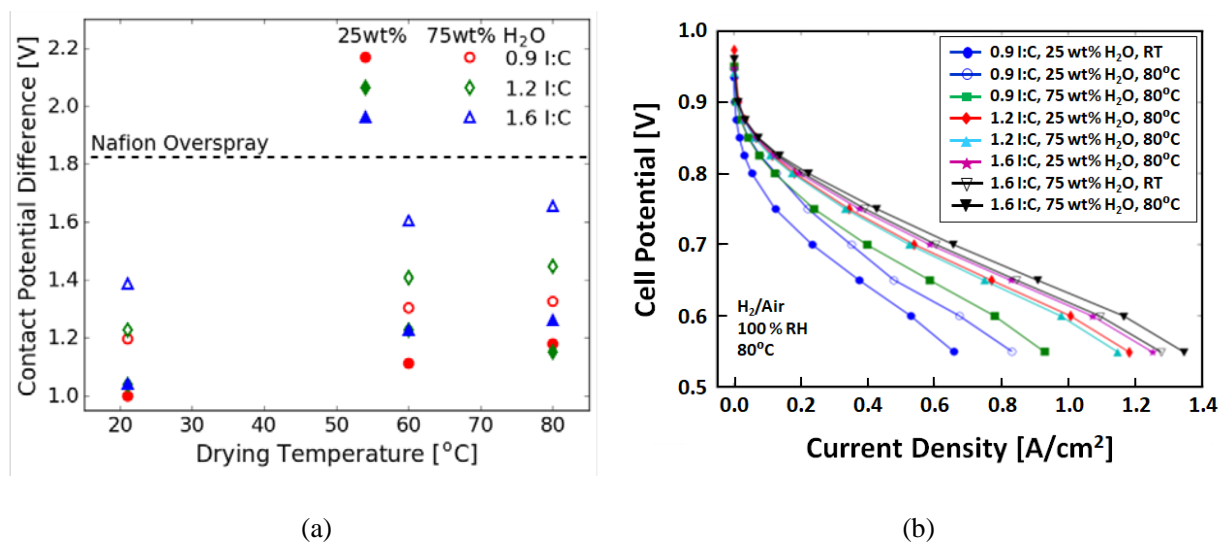


Figure 19. Kelvin Probe data for electrode inks of different ionomer-to-carbon ratios and different solvent ratios at (a) different drying temperatures and (b) in situ performance data in air for these GDEs

A continuous Nafion layer (overspray) has a much higher contact potential difference than a sprayed catalyst layer (Pt/HSC + Nafion, 0.9 ionomer to carbon ratio). By adjusting the solvent ratio, the ionomer to carbon ratio, and drying temperature, the Nafion surface concentration can be changed. We also noted that the best of these electrodes has performance that is very close to our laboratory standard.

Single-Layer Ionomer-Rich-Surface GDE Using R2R Coating

Based on results from the exploratory small-scale coating studies, i.e. trends in surface ionomer content relative to ink composition, we gravure-coated electrodes on the NREL R2R coating line at four different ink compositions. High current density performance between gravure R2R and spray coating was investigated. Gravure-coated MEAs have inferior activity to spray-coated MEAs; however, they have comparable performance at high current density. There was similar proton resistance for spray and R2R coatings. Further studies will be needed to characterize the diffusion limited current measurements and better understand the

mass transport. Electrode characterization and MEA fabrication and testing using these electrodes will continue into FY 2018.

In addition, we cast ion-transport membranes on our R2R coating line. While this is not currently part of the Fuel Cell Study, we mention this as a demonstration of capability for future efforts in the consortium potentially involving materials/projects where solution-casting of membranes and films is of interest, e.g. water membranes.

Interactions with Partner Consortium Labs

There were several planning calls and meetings early in the fiscal year with ANL regarding XCT and USAXS beam-line experiments, ultimately leading to an extensive and very detailed USAXS experimental plan for the Advanced Photon Source at ANL. In this study, NREL defined a range of ink compositions and provided materials, and ANL studied the effect of ultrasonic mixing time on the resulting particle aggregation and agglomeration state. In a first follow-on study, ANL explored variations of the ultrasonic mixing configuration as well as ball-milling. Results of the ANL experiments will be discussed in ANL's section of this report. We also provided electrode and MEA samples to ANL for XCT, which is pending.

We coordinated with ORNL on substrates and electrode materials and formulations for the electrode coating studies and provided some initial materials to ORNL. We also provided an initial set of sprayed and gravure-coated electrode samples to ORNL for electron microscopy examination.

We established an initial plan for phase field modeling of film (coating) formation in these electrodes with ionomer rich surface layers with LBNL.

Argonne National Laboratory

Argonne is supporting the Fuel Cell Study by providing characterization of catalyst-ionomer-solvent inks, studying ink synthesis parameters, such as sonication time and energy, characterization of the microstructure of electrodes, and evaluation of hot-pressed and calendared membrane-electrode assemblies' performance, as needed. The Argonne tasks for the Fuel Cell Study were to complete USAXS characterization of inks under different ultrasonic and shear mixing conditions; provide high-throughput exploration of ink synthesis parameter space, as necessary, based on initial formulation studies at NREL and ORNL; complete nano- and/or micro- x-ray tomography analysis of coated electrodes and share the data; and test hot-pressed and calendared MEAs for performance, as needed. All tasks were completed, and milestones met on schedule.

USAXS characterization was performed at Argonne's Advanced Photon Source to determine the agglomerate size of eight catalyst-ionomer-solvent inks as a function of catalyst type (Pt on low surface area carbon (Pt/Vulcan) and Pt on high surface area carbon (Pt/HSC)) ionomer to carbon ratio (I/C, 0.2, 0.5, and 0.9), and sonication type (horn sonication followed by bath sonication or bath sonication alone), and sonication time. The compositions of the inks recommended by NREL are shown in Table IV. The purpose of these studies was to determine the sonication type and time that facilitate the break-up of carbon agglomerates in the inks. The inks were sonicated in a round-bottom flask with a horn sonicator for 10 seconds, followed by sonication in a bath sonicator for 20 minutes, or were just sonicated with the bath sonicator for 20 minutes, while being chilled in an ice bath. They were then pumped out of the flask and through the x-ray beam continuously during sonication. This test apparatus is shown in Figure 20. Two inks were ball-milled instead of sonicated. Samples were extracted from the ball mill jars over the course of a day of milling and these static samples were also examined using USAXS.

Table IV. Compositions of Catalyst-Ionomer-Solvent Inks for Agglomeration Studies

Sample #	Catalyst	I/C	Pt/C (mg)	Water (mL)	1-propanol (mL)	Approx. Ionomer content D2020 (μ L)	Dispersion Method
1a	Pt/Vu	0.2	128.10	16.80	13.20	69.4	10 s horn 20 min bath
1b	Pt/Vu	0.2	128.10	16.80	13.20	69.4	20 min bath
2a	Pt/Vu	0.5	128.10	16.80	13.20	173.6	10 s horn 20 min bath
2b	Pt/Vu	0.5	128.10	16.80	13.20	173.6	20 min bath
3a	Pt/Vu	0.9	128.10	16.80	13.20	312.4	10 s horn 20 min bath
3b	Pt/Vu	0.9	128.10	16.80	13.20	312.4	20 min bath
4a	Pt/HSC	0.9	128.10	16.80	13.20	307.2	10 s horn 20 min bath
4b	Pt/HSC	0.9	128.10	16.80	13.20	307.2	20 min bath
5	Pt/Vu	0.5	1.28	22.8	17.7	1.7	Ball-milling
6	Pt/HSC	0.9	1.28	22.2	16.8	3.1	Ball-milling

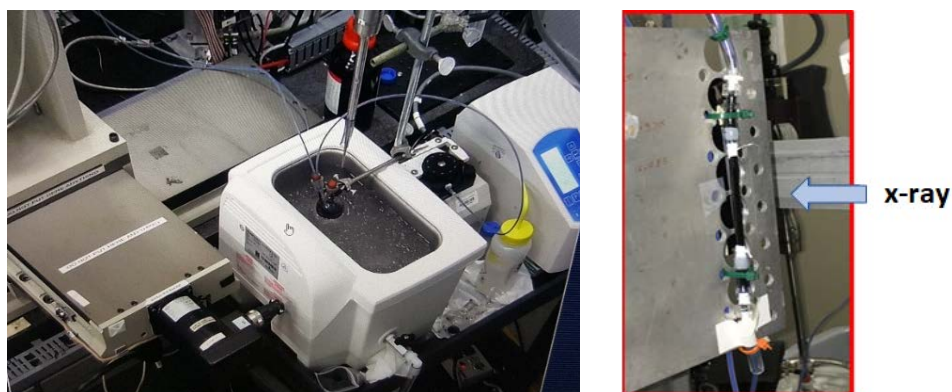


Figure 20. Experimental apparatus at the Advanced Photon Source for determining catalyst agglomerate size and content of catalyst-ionomer-solvent inks during sonication. Source: ANL

Representative scattering profiles from ink sample #1a before sonication, after 10 s of horn sonication, and during 20 minutes of bath sonication are shown in Figure 21. The scattering q regions (inversely proportional to particle/agglomerate size) that showed significant change with sonication time are in the $q = 0.0002$ and $q =$

0.002 regions, which correspond to particle/agglomerate sizes of 3 μm and 300 nm, respectively. The evolution of the scattering intensity at these two q values, which is proportional to the number of particles/agglomerates at that size, with sonication time is shown in Figure 22.

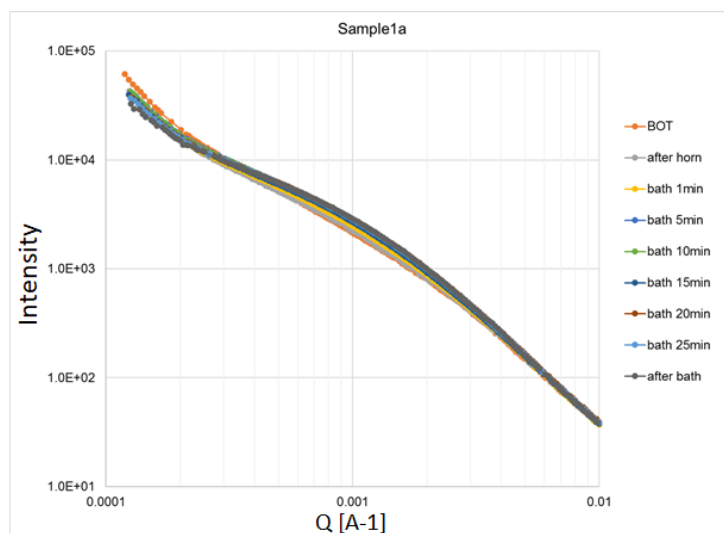
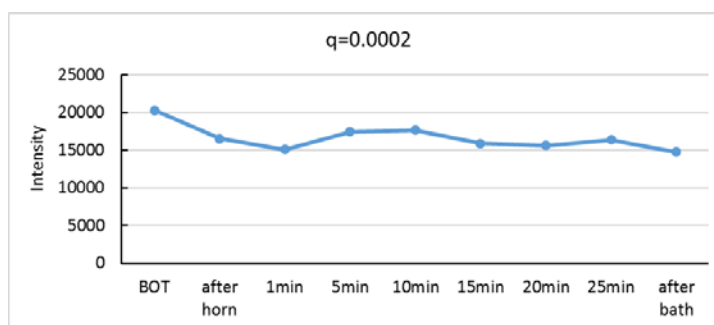
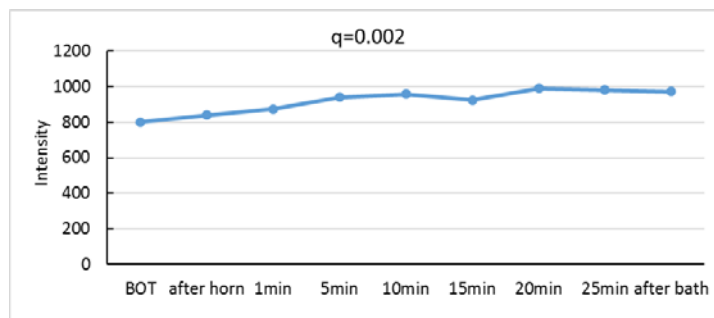


Figure 21. Ultra-small angle x-ray scattering profiles for ink sample 1a (Table 1) before sonication, after horn sonication, and during bath sonication



(a)



(b)

Figure 22. X-ray scattering intensity (proportional to the number of scatterers) at two sizes: (a) 3 μm and (b) 300 nm as a function of sonication time

These data, and the data for three other inks, show that even brief horn sonication is effective at breaking up the large agglomerates and that extensive bath sonication is needed to further break up agglomerates. The analysis of the USAXS during sonication experiments and of the ball-milled samples is on-going.

Attempts were made to analyze the x-ray nano-tomography of the cathode catalyst layers from NREL acquired early in the fiscal year. Unfortunately, the samples extracted from the NREL catalyst layers moved during the data acquisition, thus making it impossible to reconstruct the images.

Oak Ridge National Laboratory

The ORNL tasks for the Fuel Cell Study were to investigate low-cost methods of MEA manufacturing (slot-die) and coating electrocatalyst layers onto gas diffusion media to make GDEs, utilize R2R hot-pressing (calendering) of GDEs to polymer electrolyte membranes to make “unitized” MEAs, and implement processes for thickness control and metrology for MEA production quality control. The gas diffusion layer roll, carbon black catalyst support, and Pt-supported electrocatalyst powder were received from NREL. Microscopy support from ORNL Materials Characterization Center was obtained to verify coated microstructures. The dual slot-die coating on GDLs with and without Pt to form an ionomer-rich layer for bonding to the membrane was delayed.

Advanced materials characterization studies were conducted to determine surface energy using capillary flow porometry, and TEM/STEM. Initial GDL substrate thickness uniformity measurements with optical laser sensors showed that the GDL thickness ranged from 150–225 μm . Figure 21 illustrates the thickness variability for the SGL carbon baseline GDL substrate used for making the GDE coatings. Sensor readings were generally slightly lower than manual measurements.

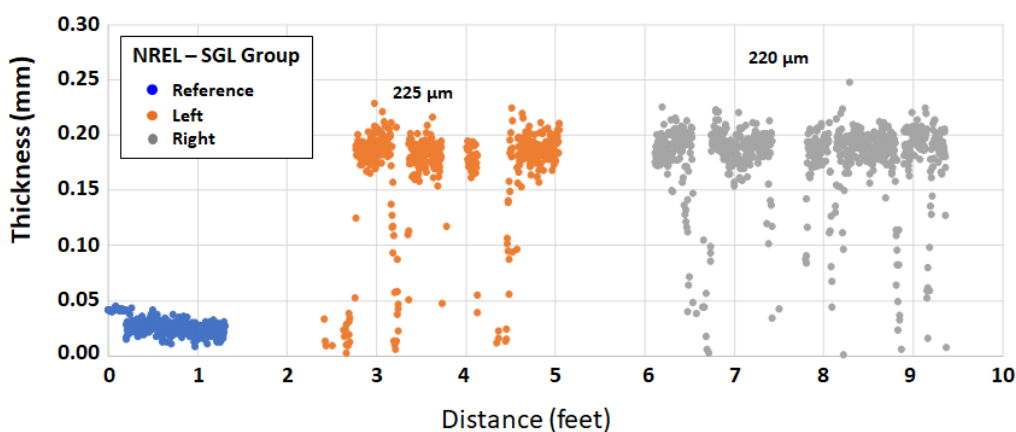


Figure 23. Measurement of thickness variability of SGL Group SIGRACET GDL 29BC carbon baseline GDL substrate for making GDE coatings

ORNL also had a cross-cutting task in FY 2017 to improve the pilot slot-die coater thickness measurement technique. Efforts completed include reviewing the Frontier Dynacoat engineering drawings, conducting an extensive literature search on slot-die state-of-the-art and flow and pressure control methods, defining the current processing specifications of the slot-die coating method, defining target performance specifications for a modified slot-die coating method, and performing a concept re-design for the slot-die head with controls and sensors.

Modeling, Simulation and Data Mining

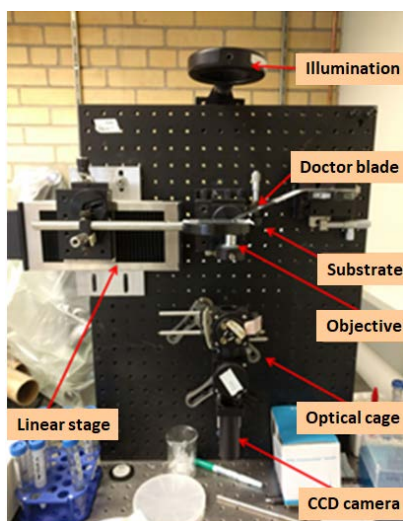
Lawrence Berkeley National Laboratory

The objectives for the LBNL modeling, simulation and data mining studies were as follows:

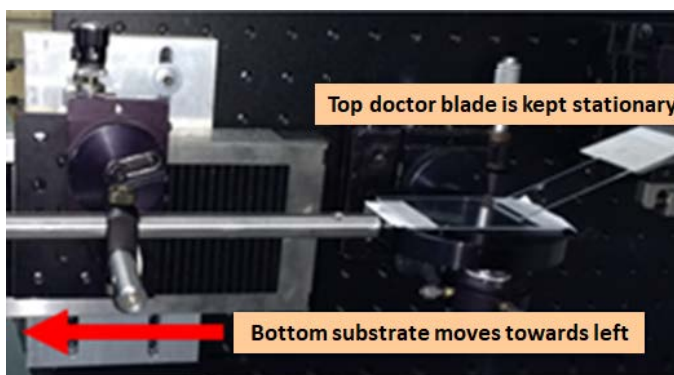
- Develop a physics-based model established on principles of colloidal science for battery electrode processing. The electrode slurry is indeed a colloidal system. A better understanding of the electrode fabrication processes from a standpoint of colloid science can shed light into the physics of battery electrode processing, which includes complex phenomena such as interactions between organic and inorganic material, rheology of slurry, drying, and evaporation of solvents. These interactions and processes affect crucial properties of the slurry, which in turn affect the properties of the electrode such as electrochemical and mechanical properties.
- Develop the theory of synthesis using data mining and deep learning approaches. Predicting the conditions under which a specific compound and crystal structure form is an unsolved and fundamental problem in materials synthesis, and one which, if understood and harnessed, could enable the rational design of synthesis pathways of novel battery materials. To address this problem, we proposed two subsequent steps. First, using text mining and natural language processing to create a database of so-called “codified recipes” of synthesis, extracted from research papers for hundreds of thousands of inorganic compounds. Second, using machine learning in combination with first-principles thermochemical data, data mine the database and suggest synthesis routes for novel battery compounds.

Visualization of the Coating Process by Optical Microscopy

In FY 2016, LBNL successfully used x-ray radiography and tomography to capture the evolution of active particles (NMC for cathode) in a slurry in the drying process. LBNL continued to delve into the fabrication processes in FY 2017 to better understand the evolution of particle assembly structures during slurry coating. Improvised equipment, shown in Figure 24a, was used to in-situ visualize the anode slurry coating process. The gap between top doctor blade and bottom substrate was set at 25 μm to form a thin coating film for better picture capture. Anode slurries of two volume fractions were used for doctor-blade coating, i.e., one was 13% vol. and the other was 26% vol.



(a)



(b)

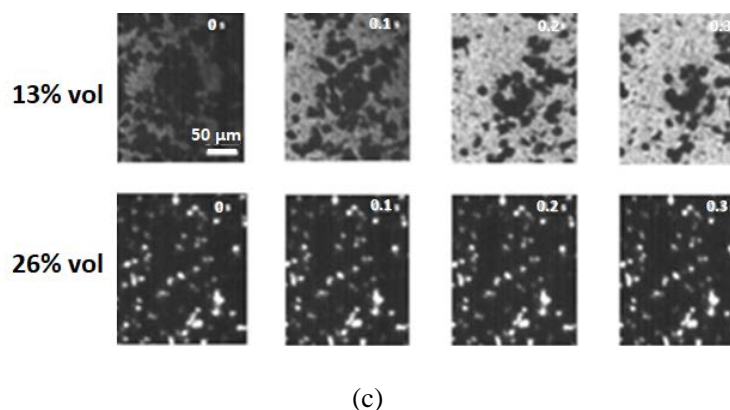


Figure 24. Visualization apparatus: (a) improvised equipment for in-situ visualization of the slurry doctor blading process, (b) enlarged view of the doctor blade head, and (c) snapshots of the doctor blading dynamic process for slurries of 13% and 26% particle volume fractions. Source: LBNL

As shown in Figure 24b, the top doctor blade was kept stationary, while the bottom substrate was withdrawn by a linear stage from right to left at a speed of 2 mm/s. An objective lens was mounted beneath the bottom substrate to visualize the dynamic process of slurry coating. The first row of Figure 24c illustrates that at 13% vol., shear stress from top doctor blade was strong enough to disassemble the graphite-carbon black large aggregates into small pieces. However, such disassembly was not observed at high slurry volume concentration. This is probably because the separations between particles became smaller at higher particle volume fraction, resulting in a stronger interparticle attraction that holds large aggregation against external shear. Therefore, the doctor blade coating process at high volume fraction slurry mainly functions as casting the slurry into a thin film without changing the particles' assembled structures.

Modeling of the Anode Slurry

The mixing process is an important step for determining the assemblies of material particles and polymer binder. Direct in-situ visualization of mixing process is challenging due to the high volume-fractions of slurries (~28%). Rheology, conversely, is a more feasible parameter to be measured and at the same time can provide information about the interparticle interactions as well as the slurry microstructures. LBNL conducted both experimental and theoretical research to understand the rheology of dense slurries. To better understand the rheology and simplify the slurry constituents, LNBL firstly studied the rheology of carbon black in polymer binder solution by developing a microrheological model. And then extended this theory to predict the viscosities of anode slurries with all the material particles.

Modeling of the carbon black slurry

Major colloidal interactions involved in the mixing process mainly included, but are not limited to Van der Waals attraction, electrostatic repulsion, and polymer steric repulsion. They are more important between particles with sizes ranging from hundreds of nanometers to several micrometers, i.e., the carbon black particles. Colloidal interactions controlled the assemblies of carbon blacks and further determined the viscosities of the carbon black slurry. Figure 25a presents the calculated energy between two carbon black particles (~200 nm in diameter) dispersed in PVDF and NMP solution. The interaction between carbon blacks is dominated by Van der Waals attraction at large separations and reaches a minimum (~8 kT) near the particle surface (~20 nm). This potential minimum is called the secondary potential minimum. When the surface-to-surface separation between two carbon blacks becomes even smaller than that compared to twice the polymer brush length, carbon blacks start feeling strong polymer steric repulsion to the order of several hundred kT. Carbon black particles cannot pass such a high energy barrier and fall in the secondary minimum. The depth of

the secondary potential minimum is a measure of the interparticle binding energy, while the position of this minimum corresponds to the most likely separation of the particles.

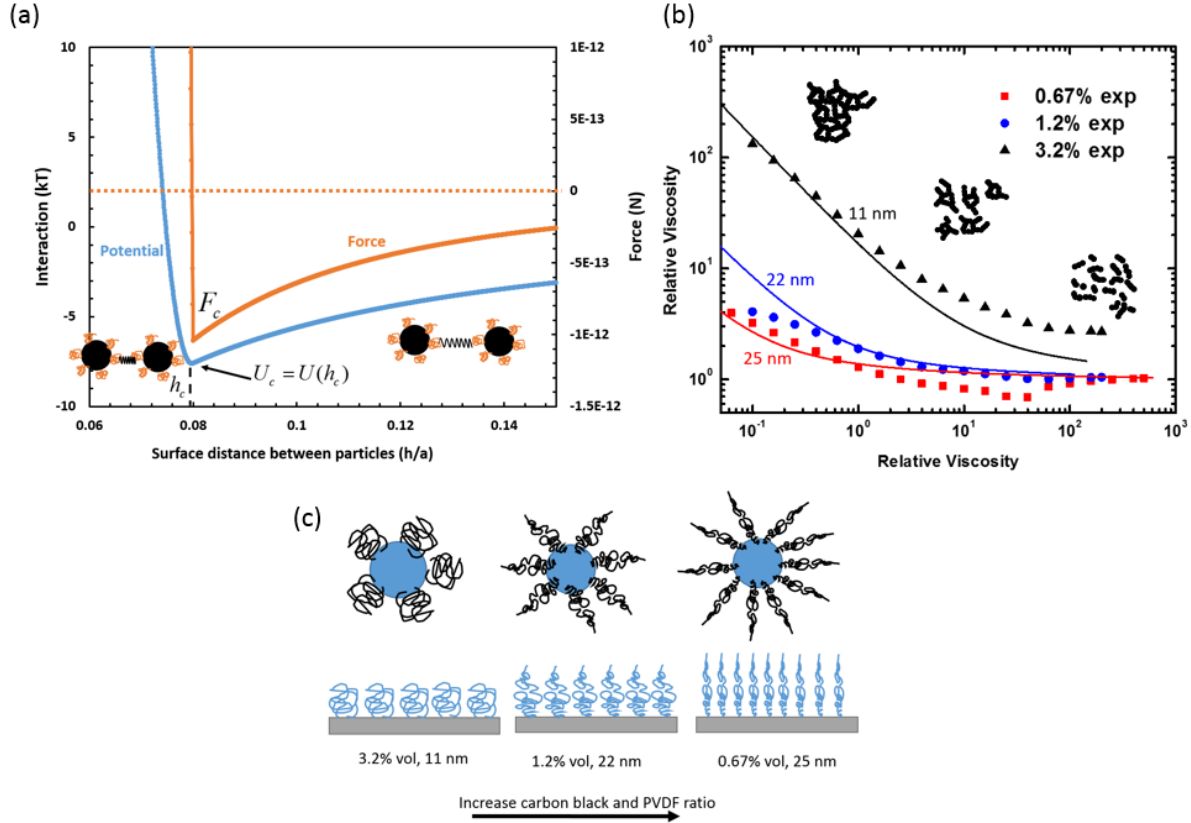


Figure 25. Rheology modeling of carbon black slurry: (a) interparticle potential between two carbon black particles dispersed in PVDF and NMP solution, (b) microrheological modeling of carbon black slurries with different volume fractions, and (c) schematics of the polymer brushes' morphologies on surface carbon blacks at a variety of ratios between polymer binder and carbon blacks. Source: LBNL

The viscosity of carbon black slurry is determined by the combination of interparticle colloidal and hydrodynamic interactions. LBNL used a dynamic rheometer to measure and microrheological model to calculate the viscosities of carbon black slurries of different volume fractions. As illustrated in Figure 25b, the carbon black slurries exhibited a shear thinning behavior. At low shear rates, colloidal interactions were dominant and carbon blacks assembled into weakly connected network. This network of carbon black was also captured by optical microscopy. As the shear rate increased, stronger shear stress (induced by external flow) broke the weak bonds between carbon blacks and disassembled large aggregates into small pieces. At even higher shear rates, hydrodynamic interactions between isolated carbon black aggregates were dominant and determined the slurry viscosity. LBNL built a microrheological model and successfully correlated the viscosities of carbon black slurries to colloidal interactions. Two major contributions to slurry viscosity, i.e., η_{hydr} the hydrodynamic viscosity and η_{struct} the colloidal interaction viscosity, were considered in this model. The total viscosity for the slurry is given by equation (1).

$$\eta_{total} = \eta_{hydr} + \eta_{struct} \quad (1)$$

The η_{hydr} viscosity was calculated using the classical Krieger-Dougherty's model, where η_L the viscosity of PVDF and NMP solution, ϕ_a the volume fraction of carbon black aggregates (a function of shear rate), and ϕ_m the maximum packing fraction. The estimation for the hydrodynamic viscosity is given by equation (2).

$$\eta_{hydr} \sim \eta_L \left(1 - \frac{\phi_a}{\phi_m}\right)^{-2.5\phi_m} \quad (2)$$

The η_{struct} viscosity was calculated by the microrheological model, where F_c the maximum attractive force, h_c the separation where the minimum interparticle potential locates, and ϕ_p the isolated carbon black volume fraction. Therefore, η_{hydr} is a function of these four parameters as shown in equation (3).

$$\eta_{hydr} \sim f(F_c, h_c, \phi_a, \phi_p) \quad (3)$$

In the rheology modeling, physical parameters such as carbon black diameter, zeta potential, and the Hamaker constant were kept the same. Polymer brush length was a fitting parameter used to match the calculated viscosities to the experimental data. With decreasing the volume fraction of carbon blacks from 3.2% to 0.67%, the length of polymer brush was increased from 11 nm to 25 nm to get the best fit. This is probably because when the mass ratio between carbon black and polymer binder decreases, the amount of polymer coating on each carbon black becomes larger. To avoid overlapping with neighboring polymer brushes, they trend to stretch longer out in the solvent, as shown in the schematics of Figure 25c. The values of polymer brush lengths chosen for data fitting were well within the range of theoretically calculated values. As illustrated in Figure 25b, the predicted viscosities from the microrheological modeling fitted well with those from measurements. This finding indicates that the ratio between the polymer binder and carbon black is a sensitive parameter for determining the interparticle interactions and the viscosity of the slurry.

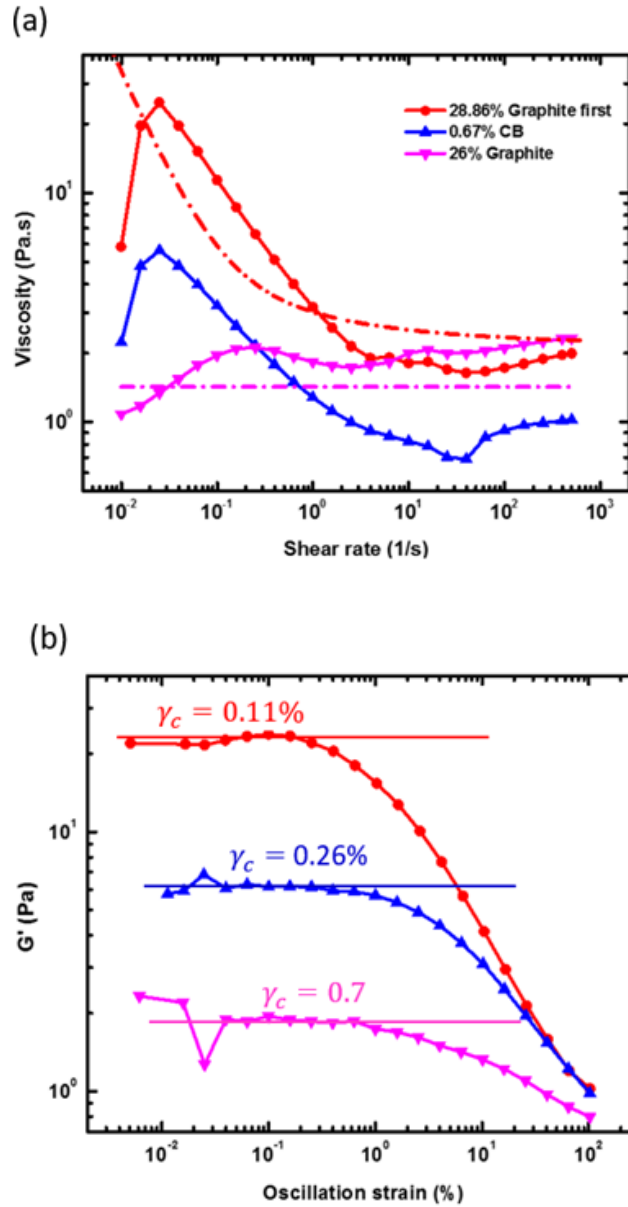
Modeling of the slurry with both graphite and carbon black

Prior to the modeling of whole slurry, we first studied the slurry with graphite and polymer binder. The viscosities of graphite slurries of 13% and 26% volume fractions are shown in Figure 26a. Though the volume fractions of graphite slurries were 20~40 times as that of carbon black slurry, they only increased the viscosity of polymer binder solution by two times. The graphite slurries exhibited no yield stresses either, indicating graphite did not form network structures. Visualization from optical microscopy showed the graphite particles repelled each other and stayed isolated. As the sizes of the graphite are about 10 μm , colloidal interactions between them are not significant. Instead, hydrodynamic interactions were dominant and controlled the assemblies and viscosity of graphite slurry. By using the Krieger-Dougherty model, viscosities of graphite slurries were well matched, as illustrated in Figure 26a. We then investigated the rheology of slurries with both graphite and carbon black particles. LBNL followed the recipe for the ORNL electrode materials to mix anode slurries. The formulation of the anode slurry was as follows:

Graphite: 92 wt % in dried electrode (26 vol% in slurry)
Carbon black: 2 wt% in dried electrode (0.67 vol% in slurry)
PVDF: 6 wt% in dried electrode (2.16 vol% in slurry)
Mass ratio between solids (graphite + carbon black + PVDF) and liquid NMP: 0.88

Due to its high molecular weight (~1,000,000), PVDF was firstly dissolved in NMP overnight. In the second step of “graphite first” mixing, graphite particles were added into the polymer solution with homogenization for 1.5 hours. Carbon blacks were added into the above slurry and the whole slurry was homogenized for another 1.5 hours. As illustrated in Figure 26a, the shape of viscosity plot of whole slurry was like the slurry

with 0.67% vol. carbon black, but with higher viscosity values. The whole slurry exhibited both shear thinning behavior and yield stress. This shows that carbon blacks still formed the network structures that fulfills the whole slurry, while the graphite particles were probably embedded in the network formed by the carbon blacks. The optical microscopy image again proved this hypothesis. We therefore set the carbon black slurry as the background medium and used its viscosity as the medium viscosity. The (hydrodynamic) contribution from addition of graphite particles to slurry viscosity was calculated from Krieger-Dougherty model, as shown in Equation (2) above. As indicated by the red and purple lines in Figure 26a, the calculated viscosities matched experimental data well. In addition, LBNL also studied the viscoelastic properties of the anode slurries and the results are presented in Figure 26b and Figure 26c. With increasing viscosities, linear viscoelastic regime becomes smaller and slurry stiffness was increased. Similarly, the storage modulus increased with increasing viscosities. Storage modulus is an important parameter charactering the elastic properties of slurry and can be related to the mechanical performance of battery.



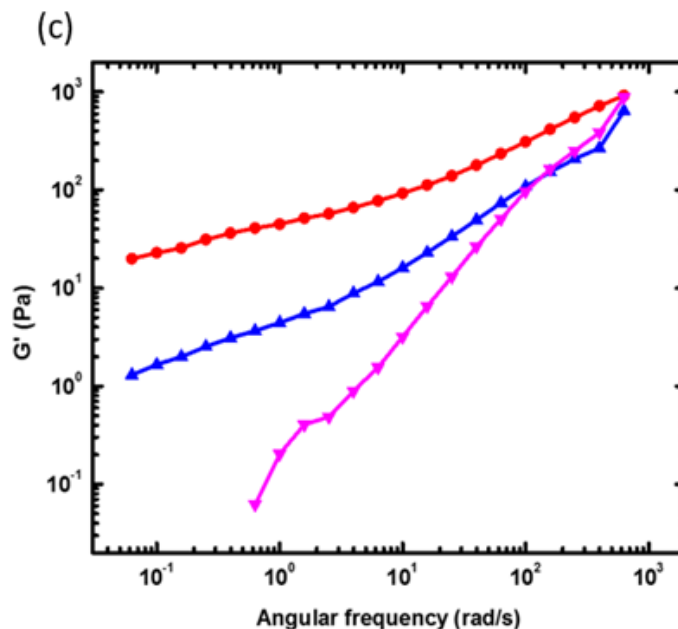


Figure 26. Rheological properties of the anode slurries: (a) viscosities of the slurries at varying shear rates, (b) linear viscoelastic regime test of the slurries, and (c) storage modulus of the slurries

Data Mining of Materials Synthesis “Recipes”

The second LBNL objective aims to develop theory of synthesis by utilizing text data mining and deep learning approaches. The important outcome of the work will be (a) a comprehensive database of “codified” synthesis recipes of known materials, which will be available to scientific community, and (b) the set of suggested synthesis routes and reactions for novel battery compounds.

To achieve the project goals, we proposed the steps specified in Figure 27.

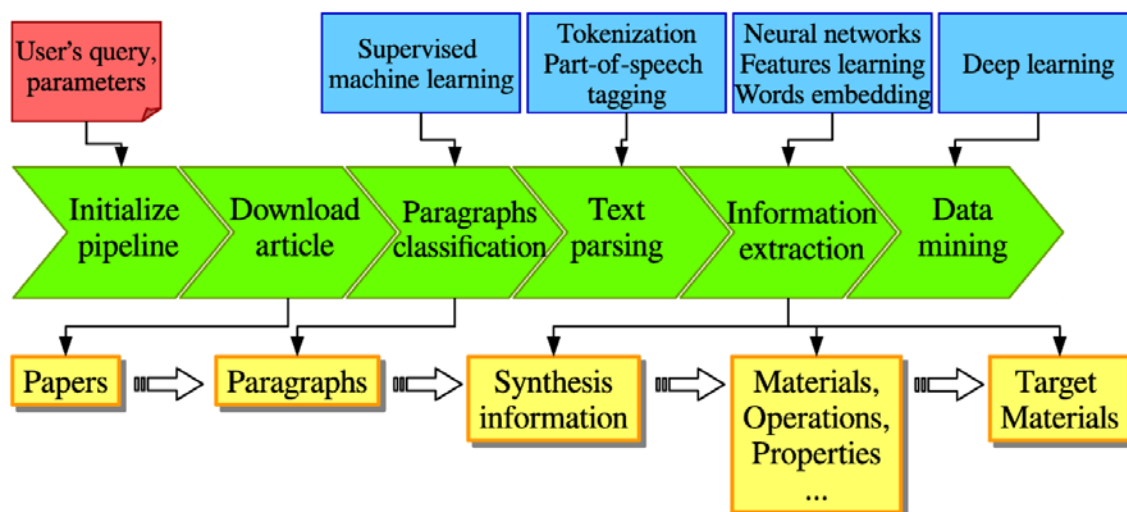


Figure 27. Schematic representation of the project pipeline to create database of “codified” synthesis recipes. Source: LBNL

The first step consists of searching and retrieval of research articles related to synthesis of battery materials. The second step is parsing of the retrieved papers and obtaining relevant paragraphs, describing synthesis

procedures. On the third step, we will create a database of “codified recipes”, extracted from the synthesis paragraphs, which will contain information about targets and precursors, operations and conditions. Next, the recipes will be mined to create synthesis patterns and suggest synthesis routes for the novel battery materials. Although the steps are given as a sequence, the process of the database development is very iterative and suggests constant updating of the previous steps to improve the quality of the database.

Obtaining text and data mining agreements with the most important publishing groups

Crawling and mining large amounts of text data from a publisher web-site requires additional Text and Data Mining (T&DM) agreements between the publisher and the university beyond the provided open-access to the journals content. At the end of FY 2017, LBNL obtained T&DM agreements with the major publishers, such as Elsevier, Springer, Wiley, Royal Society of Chemistry (RSC), American Association for the Advancement of Science (AAAS), and Electrochemical Society (ECS). For these publisher articles, scraping and downloading can be performed using CrossRef application programming interface (API). The AAAS and ECS asks for submitting a specific request each time before retrieval of a large amount the papers to avoid automatic disconnection. We were also able to negotiate the agreement with American Chemical Society (ACS) and Institute of Physics (IOP). Although they do not allow for direct crawling of papers on their web-sites, they can still provide the content (files for papers in PDF or HTML or XML format) for a specific list of journals and dates range. Unfortunately, neither University of California - Berkeley, not LBNL has a T&DM agreement with Nature publishing group; however, the recent merging of Springer with Nature provides an opportunity for a new agreement between Springer Nature and University of California – Berkeley and LBNL.

Articles retrieval and plain text extraction

We used CrossRef API to obtain a list of potential Digital Object Identifiers (DOIs) available for retrieval. The total list counts $\sim 2.8 \times 10^6$ potential papers; however, downloading for all of them was not successful. Table v contains information about total number of papers available for downloading per and the fraction of successfully retrieved papers per each publisher. Table V contains all publishing groups with T&DM agreements, the total number of papers available for downloading per agreement, and the fraction of successfully retrieved papers per each publisher. The asterisk marks the publishers for which only articles in PDF format were available.

Table V. Total Number of Papers from Various Publishers Successfully Retrieved and Presented in the Current Version of the Database

Publisher	Retrievable Documents	Percent in Database in FY 2017
Elsevier	1575747	43.8
Wiley-Blackwell	493412	29.4
Springer Nature	304463	29.1
Royal Society of Chemistry (RSC)	92045	25.5*
American Chemical Society (ACS)	77808	73.9*
The Electrochemical Society	23756	19.3*
American Association for the Advancement of Science (AAAS)	13299	0
IOP Publishing	6149	0

From Table V, it was not possible to extract all the available papers from the publisher. We found that one of the main reasons for this issue is the lack of a static HTML page. Instead, the web server uses Java Script which generates the page “on-the-fly”. As the result, crawling will return an empty output. To manage this issue, we decided to go for a publisher-specific scraping approach. We developed a web-scraping tool which considers the web-page format of a specific publisher and uses an intermediate Splash server to generate dynamic web-pages. The tool was tested for RSC publisher, and results show that with the web scraping tool we can extract ~210,000 more papers in HTML format, scraping it from issue to issue in each journal. A similar tool to scrape ECS and AAAS web-pages is being developed.

When a paper is retrieved, it must be parsed to extract the plain text only that is related to the paper body and omit all the non-relevant information. Initially, papers used were in PDF format as well as in HTML format to extract the plain text. However, due to wide variety of journal styles, parsing of PDFs is extremely complicated. For example, a one-column abstract format, a two-column format of the paper body, footnotes, graphical abstracts, and copyright lines are journal-dependent and bring multiple errors into the parsed text (~15% of extracted plain text contains encoding and parsing errors). Therefore, to proceed to the next step of the database development, we decided to limit the parsing of files for papers to HTML and XML files only where the format is more uniform.

The updated articles retrieval provided as with $\sim 1.1 \times 10^6$ papers, i.e. potential database entries compared to the previous version of the database with 641,998 entries. Among them, we identified 848,706 entries extracted from HTML files and used them for the following paragraphs classification and information extraction.

Paragraphs classification

During FY 2017, the algorithm of paragraphs classification was significantly improved to sort out the relevant paragraphs describing synthesis procedure. Briefly, in the previous version, we utilized a standard “bag-of-word” approach to create a features vector for each paragraph and used simple logistic regression to perform binary classification of the paragraphs. This gave us an F1 score accuracy of $\approx 91\%$. However, this accuracy was not good enough to unambiguously separate experimental sections with synthesis descriptions from the rest of the paragraphs. Yet, a lot of paragraphs were mistakenly assigned as paragraphs containing a synthesis recipe.

The current version of the database employs an algorithm based on the words embeddings and recurrent neural network to classify paragraphs. First, word embeddings are created using the Word2Vec model. The model uses a large corpus of data (specifically, paragraphs from the papers) to create a vocabulary based on the frequency of the words, then it runs an algorithm, which assigns each word with a specific numerical vector. As closer two words in the context are use, as smaller will be a Euclidean distance between their two vectors. Second, the paragraph is split into tokens, and each token is replaced by its lemma. Each token on the paragraph is assigned with the number which marks the position of this token in the words embeddings vocabulary. Hence, each sentence in the paragraph becomes replaced by a numeric integer vector. This vector is given as an input to the neural net algorithm. The scheme of the neural net algorithm is shown in Figure 28.

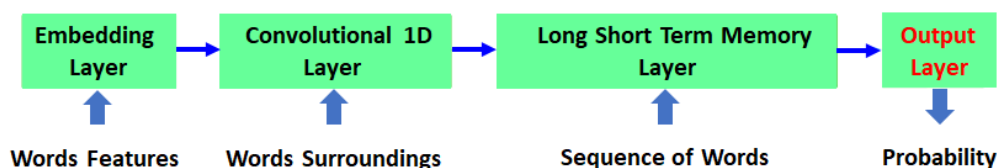


Figure 28. Schematic representation of recurrent neural network algorithm for synthesis paragraph classification

The first embedding layer uses pre-trained Word2Vec model to assign each word in the sentence with its feature vector – real-numbers vector from vocabulary. The second layer performs convolutional transformation on the output of the first layer to consider words surroundings. Third layer is recurrent layer which allows for

screening of the sequence of words before making a final decision. Finally, output layers utilize a sigmoid function to produce a probability that a paragraph contains synthesis information. To train this algorithm, we used ~2,000 manually annotated paragraphs. The overall result was an increase in accuracy of $F1 = 96\%$.

When we applied trained neural net to all the available plain text in the database, 78% of entries were found to actually have paragraphs, and only 42% have identified recipes paragraphs. The manual screening of 100 papers without any identified recipe paragraph showed that these are either theoretical or review papers or abstracts only. This result calls for additional expansion of our database in terms of the number of papers and publishers presented, and improvements of the algorithm. Moreover, to be even more precise about extraction of codified recipes, a sentence-based classification is planned. Preliminary analysis of the paragraphs showed that quite often the synthesis procedure is described in the first four to six sentences, while the rest of the paragraph describes characterization and analysis techniques.

Preliminary results on extraction of codified recipes from the relevant paragraphs show an accuracy of ~70% for materials extraction with 60% correct identification of targets among these materials, and ~80% for operations extraction. We are planning to improve the extraction by trying different approaches and algorithms of text mining. Moreover, on the next step of the database development we will translate the recipes to a simplified “coarse-grained” language, which will unify the recipes representation, and assign the identified targets and precursors with the corresponding identifications from the materials project to have access to the thermodynamic characteristics of materials. This will help us to proceed to the next step when we will learn patterns of synthesis and similarities between synthesis routes for different materials and can make prediction of the synthesis procedure for a desired compound.

R2R Functional Materials

Synthesis of the transition metal hydroxide precursors for many materials, including, lithium ion battery cathode materials, is usually conducted through the coprecipitation process. Two different types of chemical reactors have been adopted historically to grow metal hydroxide precursor particles, batch reactors (BR) and continuous stirred tank reactors (CSTR). Recently a third type of reactor is also being highly investigated for improved mixing of the reactants, which is known as the Taylor vortex reactor (TVR). As a first step in this project, we decided to model the BR. The working principle of BRs can be summarized as follows:

- An initial mixture of water and ammonia is maintained within a chemical reactor. A rotating stirrer continuously agitates the solution. Some inert gas is bubbled into the solution for the removal of excess oxygen.
- A transition metal solution is continuously pumped into the reactor that forms the hydroxide precursors.
- Constant pH is maintained by pumping sodium hydroxide into the solution.

Usually the BRs do not have any outflow of solution from the reactor; whereas, the CSTRs, as well as the TVRs, have continuous inflow and outflow of reactants. In all three types of reactors, nucleation, growth and aggregation of the primary particles occur simultaneously. Understanding the various mechanisms that are dominant at different conditions is the major purpose of this research effort.

Experimental procedure

The experiment is carried out in a 1L batch reactor with water bath jacket held at 60°C to synthesize $\text{Ni}_{1/3}\text{Mn}_{1/3}\text{Co}_{1/3}(\text{OH})_2$. The reaction proceeds with the addition of 5.0M aqueous ammonia at 15mL/h and 2.0M M-SO_4 ($\text{M} = \text{Ni}, \text{Co}, \text{and/or Mn}$ in desired ratios) at 20 mL/h. A pH meter with feedback to the pump is used to monitor the pH value, and 4.0M sodium hydroxide solution is automatically added to the reaction contents by the pump to maintain the desired pH. Samples were prepared with two solution pH levels of 10.6 and 11.4. An overhead rotator is used to stir the solution at a constant speed to ensure appropriate mixing of the reactants and products. Nitrogen gas flow is maintained through the reacting solution to get rid of oxygen, which has the

potential to unnecessarily oxidize the hydroxide products. The sample synthesized in the pH 10.6 solution is referred as sample A, while the one synthesized at the high pH level of 11.4 is referred as sample B. The total reaction time is 3 hrs. Figure 29 are SEM images of the resultant materials.

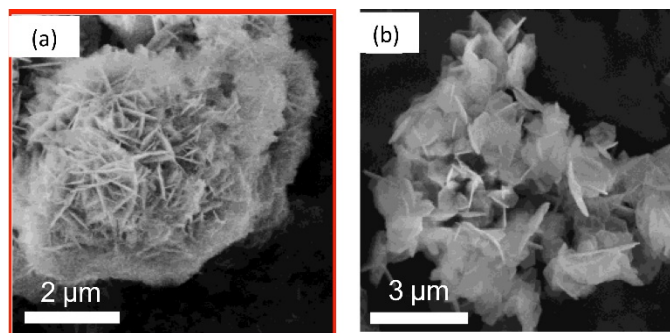


Figure 29. SEM images of (a) $\text{Ni}_{1/3}\text{Mn}_{1/3}\text{Co}_{1/3}(\text{OH})_2$ synthesized in pH 10.6 solution (i.e. sample A), and (b) $\text{Ni}_{1/3}\text{Mn}_{1/3}\text{Co}_{1/3}(\text{OH})_2$ synthesized at pH 11.4 (i.e. sample B). Source: ANL

We first focus on the secondary particle size distribution of the hydroxides collected after the 3-hour reaction time. Histograms of particle size of the samples collected from solutions with the two pH levels (i.e. 10.6 and 11.4) demonstrate a bimodal distribution. Since the median particle size, D50, is equal to the mean particle size plus or minus 1 μm in the particle size analysis, only median values will be reported here. The particle size distribution of sample A mostly falls in the range between 6 to 50 μm with a peak value at 16 μm . On the other hand, sample B shows a narrower size distribution from 2.6 to 28 μm , with a peak value at 8 μm . The smaller particles of sample B synthesized at the higher pH solution is in a good agreement with other reported research. This difference can be explained by the more negative surface potential of $\text{Ni}_{1/3}\text{Mn}_{1/3}\text{Co}_{1/3}(\text{OH})_2$ at higher pH, repulsing the particles nearby and thus preventing further agglomeration of the primary particles on the existing secondary particles.

Data Analysis

The above discussion only shows the particle size distribution after a reaction time of three hours. Further analysis has been conducted on the growth kinetics of the hydroxide secondary particles. The black curve (also denoted by square symbol) in Figure 30(a) shows the change in median particle size of sample A as a function of reaction time. The secondary particle grows from 1.5 to 16 μm in three hours. Three stages of particle growth could be observed: (I) growth and agglomeration of primary particles (before 45 mins), (II) mixed stage (45~100 mins), and (III) surface smoothing of secondary particles (after 100 mins). In stage I, primary particles are formed through instant nucleation, growth, and agglomeration after the addition of transition metal sources. The growth rate is as high as 11.0 $\mu\text{m}/\text{h}$, which is due to the immediate agglomeration of newly formed primary particles, decreasing their surface energy. In contrast, the growth rate of the particles dropped significantly to 0.9 $\mu\text{m}/\text{h}$ in stage III. During this stage, the newly added transition metal ions form smooth layers in the void space of the secondary particles surfaces, which consists of disordered nanoplates. In stage II, the growth rate of the secondary particles is about 3.2 $\mu\text{m}/\text{h}$, representing a mixed effect of stage I and stage III. This suggests the growth and agglomeration of the primary particles as well as the surface smoothing of the secondary particles occur at the same time. The change in the growth mechanism is directly related to the concentration of total transition metal ions and metal hydroxide in the reactor. A quick calculation shows the concentration of transition metal is 0.05M and 0.1M at the first turning point (1 hour) and second turning point (2 hours), respectively.

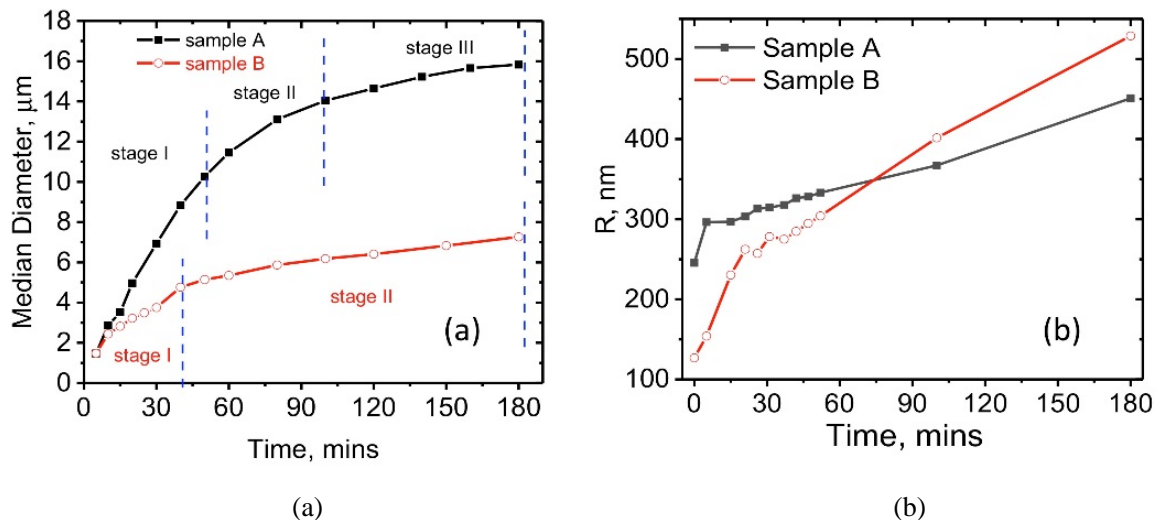


Figure 30. Particle size growth and the effective radius of disk: (a) dynamics of $\text{Ni}_{1/3}\text{Mn}_{1/3}\text{Co}_{1/3}(\text{OH})_2$ secondary particle growth measured by particle size analyzer and (b) dynamics of primary particle growth of sample measured by in-situ USAXS

Further analysis has been conducted on the dynamics of the primary particle growth for both samples, which is shown in Figure 29b. By assuming the shape of primary particles is a thin disk, the effective radius of disk could be calculated through equation: $R_g^2 = (R^2/2)$. For sample A, R grows from 245 nm at $t = 1$ min to 296 nm at $t = 5$ mins. This corresponds to a growth rate of 12 nm/min. As the reaction continues, R gradually increase from 296 nm to 451 nm at three hours. For the primary particles of sample B synthesized at a higher pH of 11.4, R of the primary particles grows from 126 nm to 529 nm at three hours. The primary particle grows fast from 126 nm to 262 nm with a growth rate of 6.5 nm/min in the first 20 minutes and then grows to 529 nm with a slower rate of 1.7 nm/min. The smaller size of primary particle of sample B at initial time could be explained by more presence of nucleation in the higher pH solution, leading to smaller particle with limited amount of metal ions available initially. Later, the primary particle of sample B grows larger than that of sample A, which is due to the more open structure of the secondary particles in sample B compared to the compact particle of sample A.

The initial size of primary particles of sample B is smaller (see Figure 30b), which can be explained by the more nucleation of hydroxide at higher pH value. At higher magnitudes of pH, due to oxidation, the surface of primary particles contains excess amounts of negative charge, which prevents its aggregation in a compact fashion. Compared to the secondary particles of sample A, these secondary particles of sample B have less primary particles and much larger voids between the nanoplates, indicating a much larger surface area and lower tap density of these secondary particles. Indeed, the tap density of these two samples after the 3-hour reaction is measured to be 1.23 g/cm^3 for sample A and 0.3 g/cm^3 for sample B. These values are in good agreements with the reported value with the same reaction time.

A simplified multiscale computational model was developed that can capture the nucleation growth and aggregation of primary particles that leads to the formation of secondary particles. Since the developed model assumes the nuclei and primary particles to be spherical in shape, it is characterized as a simplified model. Realistically, the primary particles are disk shaped. The formed secondary particles also turn out to be almost circular in the two-dimensional computational domain. However, the advantage of the developed model is that it can predict nucleation phenomena that happens in the range of angstroms, growth of the primary particles in the range of hundreds of nanometers, and the formation of the micron-size secondary particles that is associated with the aggregation of the primary ones. Since, the developed model can capture physical phenomena over a very wide range of length scales, it can be characterized as a multiscale model. The three

different physical mechanisms being considered here are nucleation, growth and aggregation. All three physical phenomena are interlinked in spatial as well as time scales. Secondary particles form due to the aggregation of sufficiently large primary particles, which was captured through Monte-Carlo simulation techniques. Growth of the primary particles from the nucleus stage was captured using a continuum scale deposition scheme. The standard classical nucleation theory was adapted to model the formation of nuclei in a supersaturated solution. A set of mass balance equations was solved to determine the concentrations of metal ions, ammonia, and metal ammonia complex within the reacting solution under equilibrium. Existence of the metal-ammonia complex plays a major role in the formation of spherical secondary particles with uniform size distribution. Hence, determining the concentration of metal-ammonia complex as functions of solution pH and ammonia content is very important for successfully capturing the growth and aggregation of particles.

Based on equilibrium relations (van Bommel and Dahn 2009), the amount of individual and total metal-ammonia complex is provided in Figure 31a. While generating this particular figure, concentrations of metal cations and aqueous ammonia have been approximated to be 2M and 1M, respectively. At relatively lower magnitudes of pH, the metal cations react with single ammonia molecules. However, at higher values of pH, an enhanced number of ammonia molecules react with the single metal cations. From Figure 31b, faster growth of the primary particles occurs at lower magnitudes of pH due to the presence of a higher concentration of the metal-ammonia complex. As the primary particles grow larger than a particular limit, they start to aggregate. At higher values of pH, repulsion of the surface charge prevents the formation of extremely large secondary particles, which has been modeled by decreasing the diffusion coefficient of primary particles with increasing hydroxyl ion concentration. Figure 31c shows the growth of secondary particles with time. Since diffusion of the primary particles on top of the secondary particles lead to its growth, the overall process is rightfully diffusion controlled and shows a square root of time dependence. The first standard deviation of the particle size distribution is shown in Figure 31c by the vertical blue error bars.

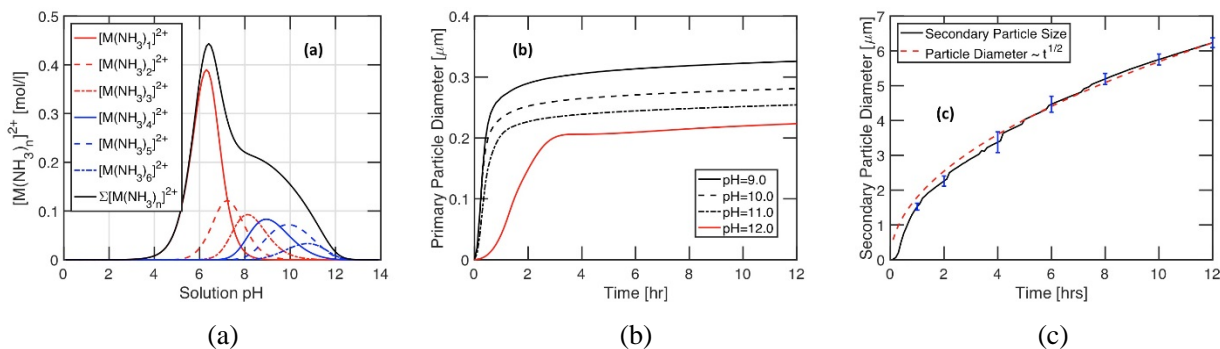


Figure 31. Individual and total metal-ammonia complex: (a) concentration of metal-ammonia complex with respect to pH showing neither very low pH nor very high pH is beneficial for the formation of the metal-ammonia complex, (b) increase in primary particle diameter with time showing that initially it increases quickly and eventually saturates due to aggregation and loss of contact with the reacting solution, and (c) growth of secondary particle diameter with time at pH = 11.0 and $C_{NH_3} = 1.0M$ showing a good correlation with the square-root of time curve indicating that the aggregation process is diffusion limited

Variation in secondary particle size obtained at the end of coprecipitation process conducted at different magnitudes of pH is illustrated in Figure 32a. The concentration of ammonia was kept constant for all the reactions ($C_{NH_3}=1.6M$). The black line indicates the computational prediction along with error bars demonstrating the first standard deviation in the particle size distribution. The red squares indicate average secondary particle sizes observed during coprecipitation experiments (adopted from Noh and Cho 2013). At higher magnitudes of pH (~12.0), even though the secondary particle size decreases, its density increases significantly. This can be attributed to the higher rate of nucleation and enhanced number of primary particles at larger magnitudes of pH. With increasing pH, higher surface potential prevents the aggregation of primary particles, which leads to smaller secondary particle sizes. This has been modeled by lowering the primary

particle diffusivity with increasing pH (or concentration of the hydroxyl anions) of the reacting solution. Even though the correlation is not very good, the model is capable of capturing the overall trend observed in experiments. The phase map between solution pH and ammonia content, demonstrating the average particle sizes and size distributions obtainable from the computational scheme, and the corresponding first standard deviation under the assumption of Gaussian particle size distributions, is illustrated in Figure 32b. All the data shown here were adopted from computational model. The greenish region indicates smaller sized secondary particles; whereas, the yellowish region represents larger particles. The light blue colored dots demonstrate the smaller values of standard deviation; whereas, pink dots indicate larger magnitudes of standard deviation for the secondary particle size distribution. Optimum operating conditions, in terms of pH and ammonia content, for precipitating relatively larger ($D_{\text{part}} \sim 8\mu\text{m}$) and smaller ($D_{\text{part}} \sim 4\mu\text{m}$) sized secondary active particles, are highlighted within the figure by red circles.

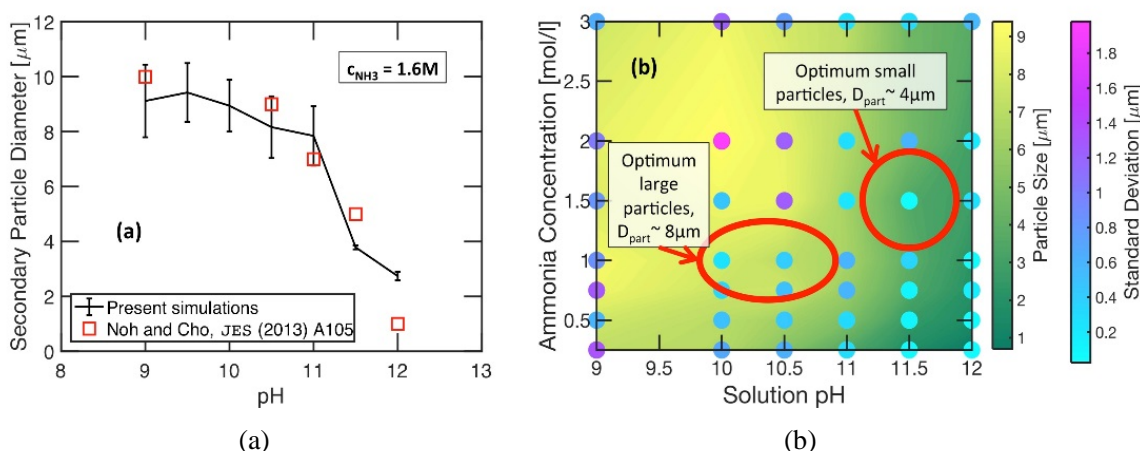


Figure 32. Variation in secondary particle size obtained at the end of coprecipitation process conducted at different magnitudes of pH: (a) comparison between experimentally obtained and computationally predicted diameter of the secondary particles obtained at different pH values and (b) phase map between ammonia content and solution pH. Source: ANL

To summarize, based on detailed experimental analysis, a comprehensive computational modeling approach was developed for predicting the impact of operating conditions on the size of transition metal hydroxide secondary particles. Visualization of the dynamics of primary and secondary particle growth during the coprecipitation process has never been reported previously. The presence of a fast and a slow growth regime for the primary particles was captured from both experimental and computational results. Also, coupling the particle growth mechanism with the chemical reactions produced the detailed methodology necessary for the successful estimation of optimum operational conditions required for precipitating particles with various sizes and size distributions. However, there still exists a scope of development in the present computational model to capture the realistic phenomena more closely. The assumption of spherical primary particle is not acceptable for the development of detailed computational schemes because they are always disk shaped. Also, growth of the primary particles happens only along the crystal facets with maximum energy. Hence, uniform growth of primary particles is not an accurate assumption. Development of more accurate models should be beneficial for capturing the physical phenomena more accurately.

R2R Water Nexus

The R2R Water Nexus project was an additional effort for the R2R AMM DOE Lab consortium in FY 2017. The effort is divided into two major tasks: (1) relocation and modification of a polymer extruder for resin wafer production and (2) design of a semi-continuous process for production of an electrodeionization wafer. All tasks and milestones were completed on time and on schedule. The evaluation of the extruder head modification and fabrication of the semi-continuous system will be completed in FY 2018.

The major efforts in FY 2017 were on the design and purchase of equipment for a semi-automated process to fabricate laboratory-scale resin wafers with an area of $\sim 220 \text{ cm}^2$. Initial design is based on the emulation of a hot-stamping process that contains the following unit operations: (1) mixing of resin beads, (2) filling the mixture into the wafer mold, and (3) curing with heat. These unit operations will be integrated to form a sequential assembly line with the blender to mix resin beads and binding polymer. The particles mixture is first fed into a dispenser device via delivery line where the particles will be evenly filled into a series of resin wafer molds. A conveyor belt then continuously sends the wafer molds into a heat-curing device to produce the final porous resin wafer. Figure 33 illustrates the semi-automated system and the highlighted features of these device related to the production rate of wafer fabrication.

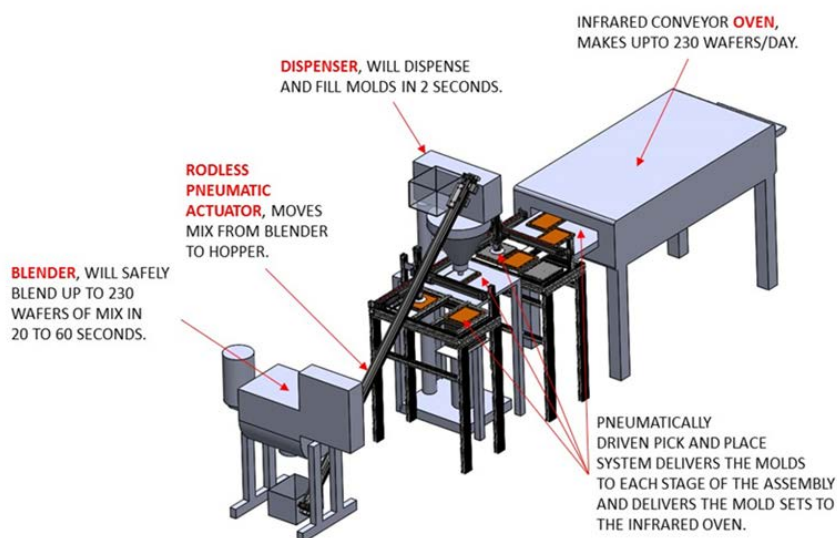


Figure 33. Schematic of semi-automated assembly line to produce resin wafers: Source: ANL

Several equipment vendor locations were visited to evaluate and test components for the best fit to the assembly line. The basic components of the system are a blender for mixing, a dispenser and an infrared oven.

Blender

The blender selected was the OptimaBlend™ Sanitary Lab Blender from Eirich Machines in Gurnee, Illinois and is sized for 1.5 cubic feet of material which can produce ~ 220 wafers per mix. The blender is designed to gently mix product within 60 seconds, at a safe height, and eliminates roll apart segregation caused by gravity when mixing ingredients of greatly varying density, shape and size by fluidizing. Fluidization is achieved by a combination of a defined geometry lifting action with a triple paddle, multi-zoned rotor that is turning about 80% faster than a traditional ribbon blender (Eirich Machines – Erich Group). The lab-scale size of the blender makes it easy to move. Figure 34a shows the equipment and Figure 34b provides a comparison of the particles mixture prepared from the laboratory and the vendor. The mixture of the particles showed no material destruction, which was a concern originally. There is a better mixture of hydrophilic and hydrophobic particles compared to the mixtures from the laboratory table-top.



(a)



(b)

Figure 34. Blending equipment and materials: (a) OptimaBlend™ Sanitary Lab Blender, and (b) particles mixtures from the laboratory and the industrial blender. Source: ANL

Dispenser

The dispenser selected was the All-Fill Inc. Model BS Pouch Filling System shown in Figure 35. The customer-designed unit fills the mold with a very uniform surface on the top after complete filling of the particles. A pneumatic lift then lifts an empty reservoir (pouch) from a weighing scale to its bulk-fill position (approximately 1"). A bottom-up fill occurs, ensuring that the amount of dust caused by product in motion will be minimized. As the bulk fill is in progress, the lift lowers to the scale at a slower speed and a bulk weight is taken at the scale. The lift then raises back up and the bottom-up dribble fill commences. The lift again lowers to the scale, and a final weight is taken. If the mix is underweight, a second dribble fill occurs. The scale also has a “real-time” weight function to guarantee flexibility and accuracy (All-Fill Inc.)



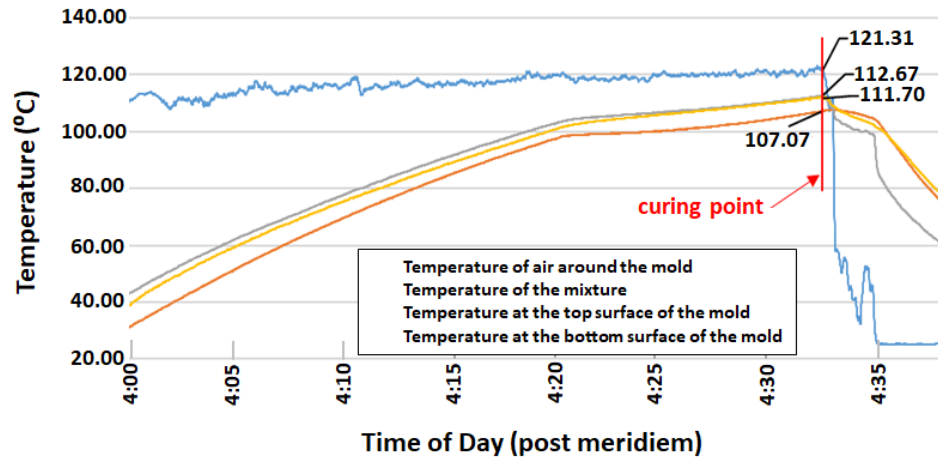
Figure 35. All-Fill Inc. Model BS particle dispenser with lift and inflatable bag clamp. Source: All-Fill Inc.

Electric Infrared Conveyor Oven

The infrared conveyor oven (for heat curing) selected is manufactured by INTEK. The oven has a digital control panel and the variable speed conveyor with VFD control can be set as low as 1/10 of a hertz. There are six separate heat zones for independently controlled top and bottom temperature settings. The heat source is a radiant long-wave electric infrared technology using INTEK IR emitters. There are adjustable baffles at the entrance and exit for improved oven efficiency (INTEK Corporation). The oven has a completely different heating profile compared to the heat-curing system typically used at ANL. Since the resin wafers fabricated at ANL have a very narrow range of temperature to produce a good porous resin wafer, we have designed a temperature profile test device to measure the heating profile. Figure 36a shows the infrared conveyor oven and Figure 36b gives the test results for the temperature profile. The temperature profile fit well into our specifications for wafer fabrication.



(a)



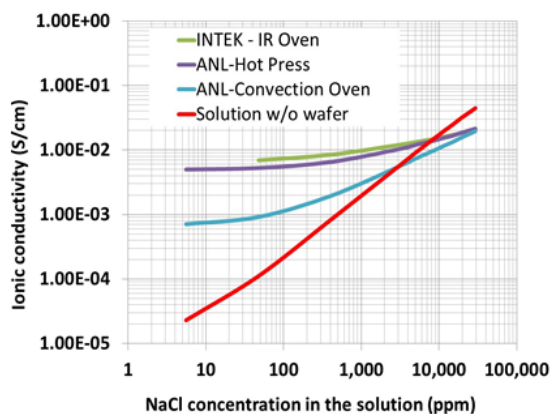
(b)

Figure 36. Curing equipment: (a) INTEK Corporation electric infrared conveyor oven and (b) the temperature profile measurement of the oven at 395°F (187°C). Sources: (a) Intek Corporation (b) ANL

Fabrication of the resin wafer using the infrared conveyor oven was also evaluated. The quality of the resin wafer was measured by their ionic conductivity compared to the previous laboratory resin wafer. Results of the tests shown in Figure 37 indicated that the resin wafer made by the oven achieve the same level of quality as the current resin wafer made by the laboratory method. Figure 37a shows samples for the laboratory method and the infrared conveyor oven and Figure 37b presents the results of the ionic conductivity as a function of salt concentration in the solution.



(a)



(b)

Figure 37. Resin wafer fabrication: (a) sample before and after curing in the INTEK electric infrared conveyor oven and (b) results of ionic conductivity measurements. Source: ANL

Figure 38 shows the assembly line under construction at ANL that will utilize the blender, the dispenser and the oven. Inspection of the wafer materials that are produced will be done with cameras and software that will confirm the consistency of the mixture. The system is expected to increase the production rate by >10x, and automation will reduce the operating cost to ~ 5%. Pilot-scale wafer production and testing will commence in FY 2018.



Figure 38. The assembly line under construction to incorporate the blender, the dispenser and oven. Source: ANL

Collaboration/Coordination/Outreach/CRADA

Core program

The consortium continues to extend its efforts for collaboration, coordination and outreach to the partner laboratories, industry and academia through the various meetings and attendance at review meetings, conferences and symposia. The R2R AMM DOE Consortium Team Leads and Team members participated in biweekly project conference calls along with AMO and FCTO Program Managers; participated in the FY 2017 project planning meeting at ANL, the FY 2017 Kickoff Meeting with the AMO Program Manager, and the FY 2017 Quarterly Review Meeting; and contributed to the FY 2017 final report, the industry CRADA call, and posters for conferences. Team members also participated in a webinar on LBNL's battery slurry characterization and modeling efforts.

ANL consortium members collaborated closely with researchers at the Advanced Photon Source, ANL to conduct USAXS experiments to determine the evolution of primary particles during the coprecipitation process. Scientists at the Materials Engineering Research Facility, ANL were collaborated with to understand the working principle of CSTR and BRs. The use of their CILAS particle size analyzer for measuring the size of the secondary particles.

ORNL collaborated with the other Consortium Labs to develop the core plan for FY 2017 study of anode architectures, PEMFC GDEs, and the abstract for submission to the TechConnect conference in May 2017. ORNL coordinated with NREL on details of the XRF analysis and next steps for in-line porosity measurement technique. An LBNL researcher was hosted in May 2017 for one week to work with ORNL researchers for electrode slurry preparation and process variables. Samples and data were exchanged with ANL in support of the Structured Anode Study. ORNL collaborated with NREL on an American Fuel Cell future proposal submission.

NREL participated with partner laboratories to coordinate tasks, milestones and timing for the new Fuel Cell core lab project; specifically, with ORNL for electron microscopy and materials and substrates for coating and calendaring, with ANL for USAXS and XCT at the APS, and with LBNL for phase field modeling. The AMO Program Manager was hosted during an NREL site visit, which included tours and discussions of various projects. Coordination was done with ANL researchers on possible NREL activities with membranes for the ANL R2R Water Nexus project. Outreach activities included attendance at the International Converting Exposition in April 2017 to better understand state-of-the-art processes in coating, drying, curing and metrology. Collaborative discussions were held with the Director of the Association of International Metallizers, Coaters and Laminators (AIMCAL) about future interactions between the Consortium and AIMCAL membership as well as communications to AIMCAL membership about the Consortium program. Outreach continued through attendance at the TechConnect World Innovation conference in May 2017 to discuss the Consortium capabilities with many industry attendees. NREL led the Consortium effort for participation in the 2017 AIMCAL R2R Conference, including interacting with Lab Leads to gather their inputs, creating and submitting a presentation and extended abstract for the Consortium's plenary presentation, registering the Consortium for a display booth, and working with ORNL and NREL communications staff to prepare plans, hand-outs and a laboratories capabilities poster for the booth. Coordination was afforded to the Consortium members for presentations for both the Hydrogen/Vehicles Program AMR and the AMO Peer Review. A poster was developed for the Fuel Cell Study and presented at the AMO Peer Review.

LBNL coordinated with the Head of the Electrochemical Technologies Group on battery assembly and test assistance and with the Group Leader of the Energy Conversion Group on biweekly scale up of slurry processes as well as slurry particle size and zeta potential characterization assistance.

CRADA solicitation and proposals

ORNL released a Development Assistance Opportunity for R2R Advanced Energy Materials Manufacturing as a CRADA Solicitation No. R2RAMM-2017-02-02 on February 2, 2017 to solicit proposals focused on advanced materials and component development, synthesis and processing methods, and quality control and metrology in the following specific areas:

- Polymer electrolyte fuel cells and membrane electrolyzers
- Advanced batteries
- Flexible electronics and displays
- Energy efficient window films
- Flexible solar photovoltaic (PV) cells
- Water separation and purification membranes

ORNL developed the first drafts of the target industry partner list for the solicitation and team members coordinated with their technology transfer offices in support of development of the multi-laboratory solicitation. ORNL discussed the Consortium efforts with many industry partners such as materials suppliers, battery and fuel cell manufacturers, etc. in context of the CRADA solicitation. NREL coordinated extensively with their industry partners in the fuel cells/electrolysis, organic photovoltaics, and water and heating, ventilation and air conditioning membranes technology areas to encourage and facilitate proposals to the CRADA solicitation.

Proposals were received for the following technology areas from the respective companies:

- Lithium-ion battery proposal from Navitas Systems and Fisker Inc.
- Membrane electrolyzer proposal from Proton Energy Systems (doing business as Proton OnSite)
- Liquid desiccant panel proposal from 7AC Technologies
- Microwave drying of electrodes proposal from Lambda Technologies
- Window films proposal from Solar Window Technologies
- Graphene PEM membrane with advanced materials frame proposal from Mechanically Intelligent (MI) Elements

The Consortium Team Leads recommended the proposals for Navitas Systems, Fisker and Solar Window and the AMO Program Manager approved those proposals to move forward to contract award. ANL, ORNL, NREL and LBNL worked closely with Business Agreements personnel and principal investigators to initiate the Terms and Agreements process for proposals that were accepted. Coordination with the responsible principal investigators at NREL (for Solar Window Technologies), ORNL (for Navitas Systems) and LBNL (for Fisker Inc.) and the principal investigators for each company was implemented to generate statements of work and cost estimates for each project. Initial consortium-company discussions were held for the three CRADA awards.

Proposals from 7AC Technologies, Lambda Technologies, and Proton Onsite were evaluated in September 2017, and those proposals receiving high evaluation scores and approved by AMO will be considered for awards pending availability of FY 2018.

Workforce Development/Educational Outreach

The consortium expanded its workforce development and educational outreach efforts in FY 2017.

Specifically, ANL employed Eva Allen, Lisa Berkland and Phillip Ridley and other undergraduates who worked on the Structured Anode Study. Eva has been accepted in a PhD program at University of Illinois at

Chicago. Lisa has recently accepted a full-time job at the Advanced Photon Source at ANL. Benjamin Hohman started at ANL on the Fuel Cell Study to determine the impact of catalyst-ionomer-solvent dispersion methods and time on the electrochemically-active surface area of the Pt/Vulcan and Pt/HSC catalysts.

At ORNL, Marissa Wood (post-doctoral research associate from University of Washington) was hired in February 2016 to work on the Structured Cathode/Anode Study half time and continues to contribute to its success. Several undergraduate students that support the Consortium efforts at ORNL include the following:

- Alexander Kukay, University of Wisconsin Eau Claire, Physics
- John Wade, Mississippi State Community College, Mechanical Engineering
- Nicholas Ross, University of Tennessee, Chemical Engineering
- Josh Fernquist, Brigham Young University Idaho, Mechanical Engineering
- Andrew Hunt, Vanderbilt University, Chemical Engineering
- Kelsey Cavallaro, University of Texas at Austin, Chemical Engineering

The one graduate student supporting the R2R efforts at ORNL is William Blake Hawley, University of Tennessee, Bredeben Center, who is in his first year of the PhD program.

NREL supported part of a graduate researcher for the diagnostics development tasks (Brian Green at the University of Denver), part of a post-doctoral researcher for coating science and rheology (Sunil khandavalli at the University of Massachusetts Amherst), and part of a post-doctoral researcher for fundamental and in-situ studies of the role of the ionomer overcoat in the performance of GDEs (Ami Neyerlin at the Colorado School of Mines). Meetings were also held with a professor from Rice University who has strong capabilities in coating flow modeling, a professor at Vanderbilt University performing fundamental fuel cell and battery ink studies, and a professor and other graduate students from the University of Massachusetts at Amherst, who perform fundamental polymer solution and colloid studies regarding future opportunities to engage with these groups within the consortium.

LBNL hired Fuduo Ma, a graduate student from the Colorado School of Mines, on January 3, 2017.

Challenges/Contingencies

For Functional Materials at ANL, the development of a computational model to capture the aggregation of primary particles was a big challenge that we were able to overcome by using a Monte-Carlo based computational approach. Capturing the different physicochemical phenomena that occurs during the calcinations process will be a big challenge. Modeling the transport of different species within the primary and secondary particles at the time of high temperature oxidation also needs to be resolved. Proper planning of required tests will alleviate most of these challenges.

Challenges for ORNL include ensuring distribution of CRADA solicitation to a wider audience, having enough battery cycling channels at ORNL to complete the anode architecture study in a timely manner (a new equipment purchase), and rate performance cycling for the combined structured anode/cathode screening, which must occur in a series format due to the large volume of cells (up to $7 \times 7 \times 3 \times 3 = 294$) that will be evaluated. Timely procurement of equipment and the use of alternate cycling facilities will aid in addressing these challenges.

NREL continues to be challenged when working with industry partners to facilitate fuel cell proposals to the CRADA solicitation because many companies submitted proposals to and AMO Funding Opportunity Announcement and a Round 3 Small Business Voucher solicitation. Companies have reported they had no cost share left, and several stated the 50% cost share was too high. A couple indicated that they did not want to collaborate on process development due to intellectual property issues. Discussions on a modification to the

R2R CRADA solicitation could result in reducing the cost share in the CRADA and lowering technology readiness levels for proposed technologies, which in turn could improve interest from industry.

There are still technical challenges for the tasks at LBNL. In-situ visualization of the electrode slurry mixing process with optical microscopy is hindered by the block of light because of high volume fractions of particles in the slurry. Other types of microscopy may be needed to do this study. Rheological modeling of electrode slurries with different materials and additional sequences require the precise calculation of the interparticle interactions at different sequences. A better characterization of the assembling structures may help. For the data mining task, obtaining synthesis paragraphs from research papers continues to be a challenge because, to extract plain text from files in PDF/XML/HTML with high accuracy, requires preserving important information about synthesis route, e.g. correct parsing of various complex chemical names, their abbreviations, and units. Developing complex and research text-specific methods can help to overcome this problem.

Risks and Risk Handling

ANL has no significant risks associated with the core program research tasks.

ORNL efforts require that rate performance cycling for the combined structured anode/cathode screening must occur in series format due to the large volume of cells ($7 \times 7 \times 3 \times 3 = 294$) that will be evaluated. An equipment purchase (96-channel Maccor cyler with 5 A channels) was completed for additional battery cycling to stay on schedule with the FY 2017 tasks and milestones with respect to the Structured Anode Study. This risk was originally identified as high, but it was mitigated by doing a series testing approach for the (shorter time) rate performance testing. Based on these “screening” results, a down-selection will be made in early FY 2018 for long-term USABC and high-rate cycling.

NREL’s Structured Anode Study has an identified risk that the porosity diagnostic will not be sensitive to relevant variations in anode properties (as opposed to the sensitivity that was demonstrated for cathode properties). For the Fuel Cell Study, the primary risk is that the concepts for phase-segregation to enable a single-layer electrode coating with an ionomer-rich surface layer will not be successful.




Project Ratings

Project performance assessments are determined through quantitative and qualitative methods in accordance with DOE O 413.3B Program and Project Management for the Acquisition of Capital Assets. Programs are assessed by definitions: green – project is expected to meet its current performance baseline; yellow – project is potentially at risk of not meeting an element of the current performance baseline; red – project is highly at risk of requiring a change to the performance baseline by the Acquisition Executive or is not being executed within the acquisition strategy and Project Execution Plan.




Table VI provides an overview of project performance for each of the Consortium laboratories and for the overall project at the end of FY 2017.

Table VI. R2R AMM Laboratory Consortium Project Ratings




ANL

Key Performance Indicator	Rating (red/green/yellow)	Status/Corrective Action
Performance		All performance targets are being met.
Cost		Project cost was within FY 2017 budget.
Schedule		All tasks and milestones were met on schedule.




ORNL

Key Performance Indicator	Rating (red/green/yellow)	Status/Corrective Action
Performance		All performance targets are being met.
Cost		Project cost was within FY 2017 budget.
Schedule		Fuel cell gas diffusion electrode study was delayed due to slot-die coating repairs that were needed in the summer of 2017. Higher priority was also given to the structured anode study. A more balanced approach will be taken in the first quarter of FY 2018 between these two tasks to get the second task back on schedule.

NREL

Key Performance Indicator	Rating (red/green/yellow)	Status/Corrective Action
Performance		All performance targets are being met.
Cost		Project cost was within FY 2017 budget.
Schedule		All tasks and milestones were met on schedule.

LBNL

Key Performance Indicator	Rating (red/green/yellow)	Status/Corrective Action
Performance		All performance targets are being met.
Cost		Project cost was within FY 2017 budget.
Schedule		All tasks and milestones were met on schedule.

OVERALL PROJECT

Key Performance Indicator	Rating (red/green/yellow)	Status/Corrective Action
Performance	●	All performance targets are being met.
Cost	●	Project cost was within FY 2017 budget.
Schedule	●	All tasks and milestones were met on schedule.

Conclusions

ANL focused on blending structured cathodes with new structured anodes to enable cycling of high loading (~4.4 mAh/cm²) electrodes. The materials that were used to produce these electrodes were a cathode lithium metal oxide powder. The baseline low loading couples achieved the 80% capacity retention between cycles 441 to 496. The top four high loading couples were (1) double pass NMC532 12 μm in the bottom layer/NMC532 6 μm in the top layer:SLC1520P only (2) double pass NMC532 12 μm in the bottom layer/NMC532 6 μm in the top layer:SLC1520P/SLC1506T mixed; (3) NMC532 6 μm only:SLC1520P only; and (4) NMC532 6 μm only:SLC1506T only. Other cells tested did not fall within the acceptable cycle number range for the 80% capacity retention line.

Research with functional materials produced a two-dimensional porous-electrode-theory based computational model that is capable of predicting the performance of secondary cathode particles under the assumption that electrolyte can flow freely through the inter-primary-particle space. Transport of lithium in the solid phase is not a major obstacle to the capacity and rate capability experienced by the lithium battery cathodes. An *in-situ* experimental technique has been developed that can capture the dynamics of primary and secondary particle growth using x-ray scattering methodologies. SEM images of the hydroxide particles precipitated at different pH values clearly demonstrate that porous and flocculated particles grow at higher magnitudes of solution pH. Dense secondary particles are observed at relatively lower values of pH. A simplified multiscale computational methodology has been developed to predict the particle size and size distribution as a function of solution pH and ammonia content. The model that uses this methodology can successfully capture the overall variation in secondary particle size with increasing pH and ammonia content. At its present state, the model cannot capture the variation in internal porosity observed in the SEM images of secondary particles obtained at different pH values.

ORNL testing of cathode samples on of the high-rate (1C/-2C), long-term cycling of the FY 2016 cathode coatings confirmed that the 1.5 Ah pouch cells from ORNL, as well as rate capability study with the full coin cells from ANL, were anode limited because of a non-graded structure at the anode. The final long-term cycling performance data for the cathode coatings showed that a coating of mixed particle sizes exhibited the best capacity retention (85%) after ~1000 cycles at 0.333/-0.333 charge/discharge rates, followed closely by the coatings with all small particles and coatings made with a single pass process having large particles on bottom. The coating made with a dual pass process having small particles on bottom and coatings made with a single pass process having small particles on bottom performed the worst with one coating showing only 51% capacity retention after ~1000 cycles.

A spread of 19% of rated discharge capacity retention at -2C was observed for the 14 structured electrode combinations investigated:

- 59% for dual-pass cathode (large bottom) and dual-pass anode (small bottom)
- 40% for cathode baseline 1 (all small) and single-pass anode (large bottom)

- 41% for baseline 1 (all small cathode) / baseline 1 (all small anode) combination
- 55% for baseline 1 (all small cathode) / baseline 2 (all large anode) combination

The electrode with small particles on bottom and baseline 1 (all small particles) for the anode showed best charge performance when combined with the third structured cathode (22% improvement in 5C charging capacity retention over baseline combination with all small particles). Baseline cathode 1 (all small particles) has much greater porosity (after calendaring) between 0.9-3.0 μm , which is much worse for charge and discharge performance. The cathode made by dual-pass with large particles on the bottom has the lowest total porosity of all cathodes measured and provides superior charge and discharge performance. A lower porosity with large anode pores between 1-5 μm is better for discharge performance.

NREL's activities related to the non-destructive evaluation of the structured electrode were completed successfully. Overall, progress on the new Fuel Cell Study was very successful, in that single-layer GDEs have been fabricated with near-target performance, and there is very insightful characterization of agglomeration in inks and coated electrode morphology.

At LBNL, the dynamic process of anode slurry coating was successfully captured by a homemade optical microscopy equipment. The coating process only functions as thinning the slurry on the substrate, while the assembly structures of particles in the slurries is mainly determined by the mixing process. A physics-based model has been built to study the rheological properties of anode slurries. The viscosities of the anode at varying shear rates were well predicted with this model. The parameters on slurry rheological properties, such as particle size, zeta potential, and slurry formulation were also investigated. A database of 848,706 research papers was created. Each of the papers was parsed to extract paragraphs describing synthesis routes as plain text. The web-scraping tools were created to update the database, yet the parsing tools were developed to accurately extract relevant information.

Glossary

1C, 2C, C/3, C/5, C/10, C/20	Charge and discharge rates of a battery are governed by C-rates. The capacity of a battery is commonly rated at 1C, meaning that a fully charged battery rated at 1Ah should provide 1A for one hour. The same battery discharging at 0.5C should provide 500mA for two hours, and at 2C it delivers 2A for 30 minutes. Losses at fast discharges reduce the discharge time and these losses also affect charge times. (The Battery University)
Calendering	A finishing process used on cloth, paper, or plastic film. A calender is employed, usually to smooth, coat, or thin a material. (Wikipedia)
Chombo	is a set of tools for implementing finite difference and finite volume methods for the solution of partial differential equations on block-structured adaptively refined rectangular grids. (LBNL)
Coin cell	A single-cell battery that is used to power wristwatches, computer clocks, hearing aids and other small devices. Also called a "coin cell," button cells look like small, squat silver cans from five to 25mm in diameter. (The Free Dictionary)
COMPRO	Software by Convergent Manufacturing Technologies for process analysis of complex structures (Convergent Manufacturing Technologies)
CrossRef	Interlinks millions of items from a variety of content types, including journals, books, conference proceedings, working papers, technical reports, and data sets. (Wikipedia)

Dual slot	A process that allows splitting of the required amount of material into two layers and then applying them simultaneously on a substrate.
Hybrid Pulse Power Characterization (HPPC)	Test procedure whose results are used to calculate pulse power and energy capability under specific operating conditions. (FreedomCAR)
Monte-Carlo	Monte-Carlo methods (or Monte-Carlo experiments) are a broad class of computational algorithms that rely on repeated random sampling to obtain numerical results. Their essential idea is using randomness to solve problems that might be deterministic in principle. They are often used in physical and mathematical problems and are most useful when it is difficult or impossible to use other approaches. Monte Carlo methods are mainly used in three distinct problem classes: optimization, numerical integration, and generating draws from a probability distribution. (Wikipedia)
NMC particles	Cathodes made of nickel manganese cobalt oxide, or NMC, are an especially hot area of battery research because they can operate at the relatively high voltages needed to store a lot of energy in a very small space. (SLAC)
Particle size distribution, D50	The value of the particle diameter at 10%, 50% and 90% in the cumulative distribution for a group of particles expressed as D10, D50, D90, etc. Particle size distribution of D50 is also known as the median diameter or the medium value of the particle size distribution, it is the value of the particle diameter at 50% in the cumulative distribution. It is one of an important parameter characterizing particle size. For example, if D50=5.8 um, then 50% of the particles in the sample are larger than 5.8 um, and 50% smaller than 5.8 um. D50 is usually used to represent the particle size of group of particles. (HMKTest®)
Pore size distribution	The distribution of the size of the various pores in a material. The range of pore sizes is divided into the groups according to IUPAC Classification of pore sizes: macropore >500 Angstroms, mesopore 20 to 500 Angstroms, supermicropore 7 to 20 Angstroms, and ultramicropore ,7 Angstroms. (Lastoskie et al. 1992)
Porosimetry	An analytical technique used to determine various quantifiable aspects of a material's porous nature, such as pore diameter, total pore volume, surface area, and bulk and absolute densities (Definitions and Translations)
Pouch cell	Instead of a metallic cylinder and glass-to-metal electrical feed-through, conductive foil-tabs are welded to the electrodes and brought to the outside in a fully sealed way with the end product resembling a pouch. (The Battery University)
Proton exchange membrane fuel cell	Type of fuel cell being developed for transport applications as well as for stationary and portable fuel cell applications (Wikipedia)
Roll-to-roll	Any process of applying coatings, printing, or performing other processes starting with a roll of a flexible material and re-reeling after the process to create an output roll. (Wikipedia)
Slot coating die	A slot coating die is a device that is capable of holding a fluid's temperature, distributing a fluid uniformly and defining a coating width. The die is

comprised of steel body sections that house the fluid flow chamber. A dual slot coating die would use an upper and lower section. (Miller 2009)

Technology Readiness Level

Technology Readiness Levels (TRLs) were developed by the National Aeronautics and Space Administration (NASA) as a systematic metric/measurement system that supports assessments of the maturity of a particular technology and the consistent comparison of maturity between different types of technology as defined in Table XI. Figure 23 above provides a schematic of the relationships. [Mankins 1995; DOE OEM 2008]

Table VII. Technology Readiness Level Definitions

U.S. DOE Office of Environmental Management
TRA/TMP Process Implementation Guide

Revision 1, August 2013
Page 9 of 76

Table 1 Technology Readiness Levels

Relative Level of Technology Development	Technology Readiness Level	TRL Definition	Description
System Operations	TRL 9	Actual system operated over the full range of expected conditions.	Actual operation of the technology in its final form, under the full range of operating conditions. Examples include using the actual system with the full range of real wastes.
System Commissioning	TRL 8	Actual system completed and qualified through test and demonstration.	Technology has been proven to work in its final form and under expected conditions. In almost all cases, this TRL represents the end of true system development. Examples include developmental testing and evaluation of the system with real waste in hot commissioning.
	TRL 7	Full-scale, similar (prototypical) system demonstrated in a relevant environment	Prototype ^a full scale system. Represents a major step up from TRL 6, requiring demonstration of a system prototype in a relevant environment. Examples include testing the prototype in the field with a range of simulants and/or real waste and cold commissioning.
Technology Demonstration	TRL 6	Engineering scale, similar (prototypical) system validation in a relevant environment	Representative engineering scale system, which is well beyond the scale tested for TRL 5, is tested in a relevant environment. Represents a major step up in a technology's demonstrated readiness and system integration. Examples include testing a prototype with real waste and a range of simulants.
Technology Development	TRL 5	Laboratory/bench scale, similar system validation in relevant environment	The basic technological components are integrated so that the system configuration is similar to (matches) the final application in almost all respects. Examples include testing a high-fidelity system in a simulated environment and/or with a range of real wastes and simulants.
	TRL 4	Component and/or system validation in laboratory environment	Basic technological components are integrated to establish that the pieces will work together. This is relatively "low fidelity" compared with the eventual system. Examples include integration of "ad hoc" hardware in a laboratory and testing with a range of simulants. ^b Laboratory/bench scale testing may not be appropriate for all systems. For example, mechanical systems, such as robotic retrieval technologies, may require full scale prototype testing to meet TRL 4.
Research to Prove Feasibility	TRL 3	Analytical and experimental critical function and/or characteristic proof of concept	Active research and development is initiated. This includes analytical studies and laboratory/bench scale studies to physically validate the analytical predictions of separate elements of the technology. Examples include components that are not yet integrated or representative. Components may be tested with simulants. For some applications, such as mechanical systems, this may include computer and/or physical modeling to demonstrate functionality.
	TRL 2	Technology concept and/or application formulated	Invention begins. Once basic principles are observed, practical applications can be invented. Applications are speculative, and there may be no proof or detailed analysis to support the assumptions. Examples are still limited to analytic studies.
Basic Technology Research	TRL 1	Basic principles observed and reported	Lowest level of technology readiness. Scientific research begins to be translated into applied research and development (R&D). Examples might include paper studies of a technology's basic properties.

^a A prototype is defined as a physical or virtual model used to evaluate the technical or manufacturing feasibility or utility of a particular technology or process, concept, end item, or system.

^b If feasible, it is recommended to include tests on a limited range of real waste prior to achieving TRL 4.

Mechanical Turk	Crowdsourcing marketplace where a requester can publish and coordinate a wide set of human intelligence tasks, such as classification, tagging, surveys, and transcriptions. (Amazon Web Services)
Weblane	During the sheet printing process, after each sheet has been printed, the press table needs to be hand-wiped to ensure the ink will not smear and ruin the printed circuit. In weblane printing, the machine has a wiper mechanism, automating the process. Using weblane printing increases production speeds and creates a more streamlined printing process. (GM Nameplate)
Word2vec	A group of related shallow two-layer neural network models used to produce word embeddings and trained to reconstruct linguistic contexts of words. (Wikipedia)

Key Publications

References

1. Howell, D. 2017. “Electrochemical Energy Storage R&D Overview.” Presented at the 2017 Annual Merit Review and Peer Evaluation Meeting (AMR) for the Hydrogen and Fuel Cells Program and the Vehicle Technologies Office, Washington, DC (June).
2. Garland, N. L. 2017. “Manufacturing R&D Program Area.” Presented at the 2017 Annual Merit Review and Peer Evaluation Meeting (AMR) for the Hydrogen and Fuel Cells Program and the Vehicle Technologies Office, Washington, DC (June).
3. Macknick, J.; Newmark, R.; Heath, G.; Hallett, K.C. 2011. A Review of Operational Water Consumption and Withdrawal Factors for Electricity, Generating Technologies, NREL Technical Report NREL/TP-6A20-50900 (March)
4. “Materials Genome Initiative for Global Competitiveness,” National Science and Technology Council, Executive Office of the President, Washington, DC, June 24, 2011, accessed on November 15, 2017: <http://www.whitehouse.gov/mgi>.
5. Rupnowski, P.; Ulsh, M.; Sopori, B.; Green, B.; Wood III, DL.; Li, J.; Sheng, Y. 2017. “In-line monitoring of Li-ion battery electrode porosity and areal loading using active thermal scanning – modeling and initial experiment.” *Journal of Power Sources*, in press: 11 pages <https://doi.org/10.1016/j.jpowsour.2017.07.084>
6. Sopori, B.; Ulsh, M.; Rupnowski, P.; Bender, G.; Penev, M.; Li, J.; Daniel, C.; Wood III, D. L. “Batch and Continuous Methods for Evaluating the Physical and Thermal Properties of Films.” Filed March 8th, 2016, U.S. Patent Application No. 16/051,314 (Alliance for Sustainable Energy, LLC).
7. van Bommel, A. and Dahn, J. 2009. “Analysis of the growth mechanism of coprecipitated spherical and dense nickel, manganese and cobalt-containing hydroxides in the presence of aqueous ammonia”. *Chemistry of Materials*, 21: 1500 – 1503.
8. Noh, M. and Cho, J. 2013. “Optimized synthetic conditions of $\text{LiNi}_{0.5}\text{Co}_{0.2}\text{Mn}_{0.3}\text{O}_2$ cathode materials for high rate lithium batteries via co-precipitation method”. *Journal of the Electrochemical Society*, 160: A105 – A111.
9. Eirich Machines – Eirich Group. Accessed on December 19, 2017. www.eirichusa.com/products/lab-equipment/optimablend-sanitary-lab-blender
10. All-Fill Inc. Accessed on December 19, 2017. www.all-fill.com/filling-machines/auger-fillers/fill-to-weight-auger-fillers/model-bs-pouch-filling-system/

11. INTEK Corporation. Assessed on December 19, 2017. <http://intekcorp.com/custom-continuous-process-conveyor-oven-electric-infrared-annealing-poly-automotive-parts/>
12. Amazon Web Services blog. <https://cloudacademy.com/blog/machine-learning-datasets-mechanical-turk/>
13. The Battery University, BU-402: What Is C-rate.
http://www.batteryuniversity.com/learn/article/what_is_the_c_rate
14. Wikipedia – Calendering, www.en.wikipedia.org/wiki/Calendering
15. Lawrence Berkeley National Laboratory Commons, <https://commons.lbl.gov/display/chombo/Chombo++Software+for+Adaptive+Solutions+of+Partial+Differential+Equations>
16. The Free Dictionary. www.encyclopedia2.thefreedictionary.com/Coin+cell
17. Convergent Manufacturing Technologies, <http://www.convergent.ca/products/compro-simulation-software>
18. Wikipedia – CrossRef, <https://en.wikipedia.org/wiki/Crossref>
19. FreedomCAR Battery Test Manual For Power-Assist Hybrid Electric Vehicles, U.S. Department of Energy, Energy Efficiency and Renewable Energy, Idaho Operations Office, October 2003.
https://avt.inl.gov/sites/default/files/pdf/battery/freedomcar_manual_04_15_03.pdf
20. Wikipedia – Monte Carlo, https://en.wikipedia.org/wiki/Monte_Carlo
21. “A Simple Way to Make Lithium ion Battery Electrodes that Protect Themselves” SLAC Press Release on January 11, 2016. <https://www6.slac.stanford.edu/news/2016-01-11-simple-way-make-lithium-ion-battery-electrodes-protect-themselves.aspx>
22. HMKTest® website. www.aimsizer.com/faqs-What-is-D50.html
23. Lastoskie, C; Keith E. Gubbins, K.E.; Quirk, N. 1993. “Pore Size Distribution Analysis of Microporous Carbons: A Density Functional Theory Approach.” J. Phys. Chem., 97: 4786-4796
24. Definitions and Translations. <http://www.definitions.net/definition/porosimetry>
25. The Battery University, BU-301a: Types of Battery Cells.
http://www.batteryuniversity.com/learn/article/types_of_battery_cells
26. Wikipedia – Proton Exchange Membrane for Fuel Cells.
https://en.wikipedia.org/wiki/Proton_exchange_membrane_fuel_cell
27. Wikipedia – Roll-to-Roll Processing, https://en.wikipedia.org/wiki/Roll-to-roll_processing
28. Miller, M.D. ‘Slot Die Coating Technology’ Extrusion Dies Industries, LLC, Chippewa Falls, WI.
<https://www.pstc.org/files/public/Miller09.pdf>
29. Mankins, J. C. 1995. Technology Readiness Levels: A White Paper, Advanced Concepts Office, Office of Space Access and Technology, National Aeronautics and Space Administration. (April)
30. U.S. Department of Energy, Office of Environmental Management, Technology Readiness Assessment (TRA) / Technology Maturation Plan (TMP) Process Guide, March 2008
31. GM Nameplate, <https://www.gmnameplate.com/company/blog/printing-sheet-vs-weblane-printing>
32. Wikipedia – Word2vec, <https://en.wikipedia.org/wiki/Word2vec>

Bibliography

Daniel, C. D. “Roll-to-Roll Advanced Materials Manufacturing Lab Consortium Project ID: MN018.” 2017. Presented at the U.S. Department of Energy’s (DOE’s) 2017 Annual Merit Review and Peer Evaluation Meeting for the Hydrogen and Fuel Cells Program and the Vehicle Technologies Office, Washington, DC (June) https://www.hydrogen.energy.gov/annual_review17_manufacturing.html

Daniel, C. D. “Roll-to-Roll Advanced Materials Manufacturing Lab Consortium Project Period: FY 2016/17.” 2017. Presented at the Advanced Manufacturing Office Peer Review, Arlington, VA (June) <https://energy.gov/eere/amo/downloads/amo-2017-technical-resources-forum-presentations>

Daniel, C. D.; Wood, D.; Ulsh, M.; Krumdick, G.; Prasher, R. “AMO Roll-to-roll Advanced Materials Manufacturing Laboratory Consortium.” 2017. Presented at the TechConnect World Innovation Conference & Expo (May).

http://www.techconnectworld.com/World2017/sym/Advanced_Manufacturing_Innovation.html

Du, Z.; Rollag, K.M.; Li, J.; An, S.J.; Wood, D.L. 2017. “Enabling aqueous processing for crack-free thick electrodes”. *Journal of Power Sources*, 354, (June): 200-206

Higa, K.; Zhao, H.; Parkinson, D.; Barnard, H.; Ling, M.; Liu, G.; Srinivasan, V. “Electrode Slurry Particle Density Mapping Using X-ray Radiography.” 2017. *Journal of the Electrochemical Society*, 164(2), A380-A388.

Khandavalli, S.; Mauger, S.; Stickel, J. J.; Hurst, K.; Neyerlin, K. C.; Ulsh, M. 2017. “Rheological properties and interparticle interactions of fuel cell catalyst dispersions,” poster presentation at the Society of Rheology Meeting; Denver, CO (October).

Krumdick, G.; Dunlop, A.; Trask, S.; Polzin, B.; Jansen, A.; Wood, D.; Wood, M.; Li, J.; Daniel, C.; Ulsh, M.; Rupnowski, P.; Prasher, R.; Ma, F. 2017. “Structured Cathodes and Anodes for High-Energy and High-Power Lithium-Ion Batteries (LIBs).” poster presentation at the Advanced Manufacturing Office Peer Review; Arlington, VA (June).

Ma, F; Battaglia, V.; Prasher, R. “Viscoelastic Modeling of Anode Slurry.” 2018. *Journal of the Electrochemical Society*, (forthcoming).

Mauger, S.; Khandavalli, S.; Neyerlin, K.C.; Stickel, J.; Hurst, K.; Ulsh, M. 2017. “Rheological characterization of interparticle interactions in fuel cell catalyst dispersions,” oral presentation IO1A-1382 at the Fall Electrochemical Society Meeting; National Harbor, MD; (October).

Mauger, S.; Neyerlin, K.C.; Yang-Neyerlin, A.C.; Bender, G.; Ulsh, M.; Green, B.; More, K. 2017. “Material-process-performance relationships for roll-to-roll coated fuel cell electrodes,” oral presentation IO1B-1441 at the Fall Electrochemical Society Meeting; National Harbor, MD (October).

ORNL Invention Disclosure 201303063, “Transformational Thick Cathode having Hierarchical Pore Structure”

Rupnowski, P.; Ulsh, M.; Sopori, B.; Green, B.; Wood III, D.L.; Li, J.; Sheng, Y. 2017. “In-line monitoring of Li-ion battery electrode porosity and areal loading using active thermal scanning – modeling and initial experiment.” *Journal of Power Sources*, in press: 11 pages
<https://doi.org/10.1016/j.jpowsour.2017.07.084>

Seong Jin An, Jianlin Li, and David L. Wood. 2017. Addendum to “Fast formation cycling for lithium ion batteries” [*J. Power Sources* 342 (2017) 846–852], *Journal of Power Sources*, 350, (May), Page 152

Sopori, B.; Ulsh, M.; Rupnowski, P.; Bender, G.; Penev, M.; Li, J.; Daniel, C.; Wood III, D.L. “Batch and Continuous Methods for Evaluating the Physical and Thermal Properties of Films.” Filed March 8th, 2016, U.S. Patent Application No. 16/051,314 (Alliance for Sustainable Energy, LLC).

Ulsh, M.; Mauger, S.; Neyerlin, K.C. 2017. “Material-process-performance relationships for roll-to-roll coated PEM electrodes,” poster presentation at the Hydrogen and Fuel Cells/Vehicle Technologies Office Annual Merit Review and Peer Evaluation Meeting, Washington, DC (June).

Ulsh, M.; Mauger, S.; Neyerlin, K. C.; Wood, D.; Li, J.; Wood, M.; More, K.; Myers, D.; Kariuki, N.; Park, J.; Cetinbas, C. F.; Ahluwalia, R.; Krumdick, G.; Weber, A.; Ma, F.; Prasher, R. 2017. “PEM Fuel Cell Gas-diffusion Electrodes with Ionomer-rich Surface Layer.” poster presentation at the Advanced Manufacturing Office Peer Review; Arlington, VA (June).

Ulsh, M. “DOE Advanced Materials Manufacturing/Roll-To-Roll Consortium.” 2017. Presented at the AIMCAL R2R Conference (October). <http://www.aimcal.org/>

Wood, M.; Li, J.; David L. Wood, D.L.; Daniel, C.; Krumdick, G.; Jansen, A.; Polzin, B. “Evaluation of Thick Graded-Porosity Cathode Architectures as a Means of Improving Energy Density and Battery Performance”. Submitted to the *Journal of Power Sources*, forthcoming